

USING WRF/CHEM, IN-SITU OBSERVATIONS, AND CALIPSO DATA TO
SIMULATE SMOKE PLUME SIGNATURES ON HIGH-LATITUDE PIXELS

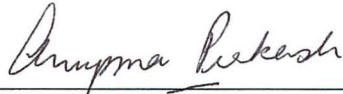
By

James Michael Madden

RECOMMENDED:



Dr. Kenneth Sassen



Dr. Anupma Prakash



Dr. Georg Grell

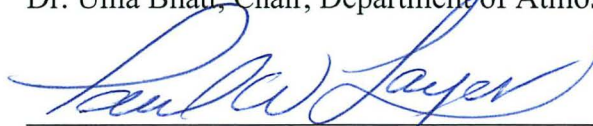


Dr. Nicole Mölders, Advisory Committee Chair

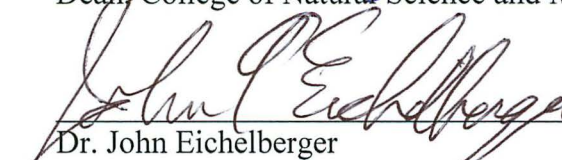


Dr. Uma Bhatt, Chair, Department of Atmospheric Sciences

APPROVED:



Dr. Paul Layer
Dean, College of Natural Science and Mathematics



Dr. John Eichelberger
Dean of the Graduate School

4/21/14

Date

USING WRF/CHEM, IN-SITU OBSERVATIONS, AND CALIPSO DATA TO
SIMULATE SMOKE PLUME SIGNATURES ON HIGH-LATITUDE PIXELS

A
THESIS

Presented to the Faculty
of the University of Alaska Fairbanks

in Partial Fulfillment of the Requirements

for the Degree of

MASTER OF SCIENCE

By

James Michael Madden, B.S.

Fairbanks, Alaska

May 2014

Abstract

The transport of wildfire aerosols provides concerns to people at or near downwind propagation. Concerns include the health effects of inhalation by inhabitants of surrounding communities and fire crews, the environmental effects of the wet and dry deposition of acids and particles, and the effects on the atmosphere through the scattering and absorption of solar radiation. Therefore, as the population density increases in Arctic and sub-Arctic areas, improving wildfire detection increasingly becomes necessary. Efforts to improve wildfire detection and forecasting would be helped if additional focus was directed toward the distortion of pixel geometry that occurs near the boundaries of a geostationary satellite's field of view. At higher latitudes, resolution becomes coarse due to the curvature of the Earth, and pixels toward the boundaries of the field of view become difficult to analyze.

To assess whether it is possible to detect smoke plumes in pixels at the edge of a geostationary satellite's field of view, several analyses were performed. First, a realistic, four-dimensional dataset was created from Weather Research and Forecasting model coupled with Chemistry (WRF/Chem) output. WRF/Chem output was statistically compared to ground observations through the use of skill scores. Output was also qualitatively compared to vertical backscatter and depolarization products from the Cloud-Aerosol Lidar and Infrared Pathfinder Satellite Observation (CALIPSO) satellite.

After the quantitative and qualitative examinations deemed the model output to be realistic, synthetic pixels were constructed, appropriately sized, and used with the realistic dataset to examine the characteristic signatures of a wildfire plume. After establishing a threshold value, the synthetic pixels could distinguish between clean and smoke-polluted areas. Thus, specialized retrieval algorithms could be developed for smoke detection in strongly distorted pixels at the edge of a geostationary satellite's field of view.

Table of Contents

	Page
Signature Page	i
Title Page	iii
Abstract	v
Table of Contents	vii
List of Figures	ix
List of Tables	xiii
Acknowledgements	xiv
Chapter 1 Introduction	1
1.1 Work Description	4
1.2 Climatology of Alaska Wildfires	5
1.3 Structure of Thesis	9
Chapter 2 Experimental Design	13
2.1 Advanced Research WRF	13
2.1.1 WRF Physics Packages	15
2.1.2 WRF Chemistry Packages	17
2.1.3 Emissions	18
2.1.4 Model Domain and Initialization	19
2.2 Model Evaluation Techniques	19
2.2.1 Synoptic Conditions	24
2.2.2 CALIPSO Components and Products	25
2.2.3 CALIOP's Application to Model Evaluation	29
2.3 Synthetic Pixel Design	29
Chapter 3 Evaluation of WRF/Chem by Meteorological Surface Observations and CALIPSO	
Data	35
3.1 Meteorological Quantities	35
3.1.1 Temperature	35

3.1.2 Dewpoint Temperature	40
3.1.3 Relative Humidity.....	40
3.1.4 Precipitation.....	43
3.1.5 Wind Speed.....	45
3.1.6 Wind Direction	47
3.1.7 Downward Shortwave Radiation.....	47
3.1.8 Sea-level Pressure.....	50
3.1.9 Conclusions on the Meteorological Performance.....	53
3.2 Comparison of CALIPSO 1B Products and WRF/Chem Cross-sections	54
3.2.1 July 7 Case.....	54
3.2.2 July 11 Case.....	59
3.2.3 July 27 Case.....	59
3.2.4 Conclusions on the Vertical Aerosol Performance.....	68
 Chapter 4 Synthetic Pixels	 69
4.1 Synthetic Pixel Construction.....	69
4.2 Clean Synthetic Pixels.....	73
4.3 Polluted Synthetic Pixels.....	73
4.4 Synthetic Pixel Discussion.....	81
 Chapter 5 Discussion and Conclusions.....	 85
5.1 Future Work	87
 References.....	 89

List of Figures

	Page
Figure 1.1: MODIS Aqua image of wildfire smoke propagating through Interior Alaska and Western Canada	2
Figure 1.2: Total changes in mean annual temperature (K) from 1949 to 2012	10
Figure 2.1: An illustration of a terrain-following coordinate system, and an illustration of the Arakawa C-grid staggering class	14
Figure 2.2: Topography height (m) as used in the model domain	20
Figure 2.3: Model domain with WRF/Chem terrain height (m) and locations of observation stations	22
Figure 2.4: An artist’s illustration of the A-Train satellites	26
Figure 2.5: Theoretical pixel sizes adapted for a 1 km nadir field of view	30
Figure 2.6: Length scale of a synthetic pixel with corresponding ‘oval’ shape	32
Figure 2.7: An illustration of the averaging of individual grid cells to create a synthetic pixel	33
Figure 3.1: Time series of daily average temperature	37
Figure 3.2: Simulated versus observed daily minimum and maximum temperatures	39
Figure 3.3: Time series of dewpoint temperature	41
Figure 3.4: Time series of relative humidity	42
Figure 3.5: Time series of daily accumulated precipitation	44
Figure 3.6: Time series of wind speed	46
Figure 3.7: Time series of wind direction	48
Figure 3.8: Time series of daily accumulated downward shortwave radiation	49
Figure 3.9: Time series of sea-level pressure	51
Figure 3.10: Model domain featuring the locations of all sea-level pressure stations	52
Figure 3.11: MODIS Aqua visible and infrared images of wildfire smoke propagating through the approximate model domain, taken on 7 July, 1310 UTC	55
Figure 3.12: WRF/Chem breathing level PM ₁₀ concentrations at 7 July, 1300 UTC with the CALIPSO scan track in red	56

Figure 3.13: The nighttime total attenuated backscatter and perpendicular backscatter at 532 nm from CALIPSO's CALIOP lidar for 7 July, 1311 to 1312 UTC.	57
Figure 3.14: The linear depolarization ratio derived from nighttime CALIOP backscatter data for 7 July, 1311 to 1312 UTC, and the WRF/Chem model cross-section of PM_{10} concentration at 7 July 1300 UTC	58
Figure 3.15: MODIS Aqua visible and infrared images of wildfire smoke and clouds propagating through the approximate model domain, taken on 11 July, 1245 UTC	60
Figure 3.16: WRF/Chem breathing level PM_{10} concentrations at 11 July, 1300 UTC	61
Figure 3.17: The nighttime total attenuated backscatter and perpendicular backscatter at 532 nm from CALIPSO's CALIOP lidar for 11 July, 1246 to 1247 UTC	62
Figure 3.18: The linear depolarization ratio derived from nighttime CALIOP backscatter data for 11 July, 1246 to 1247 UTC, and the WRF/Chem model cross-section of PM_{10} concentration at 11 July 1300 UTC	63
Figure 3.19: MODIS Aqua visible and infrared images of wildfire smoke and clouds propagating through the approximate model domain, taken on 27 July, 1245 UTC	64
Figure 3.20: WRF/Chem breathing level PM_{10} concentrations at 27 July, 1300 UTC	65
Figure 3.21: The nighttime total attenuated backscatter and perpendicular backscatter at 532 nm from the CALIPSO's CALIOP lidar for 27 July, 1246 to 1247 UTC	66
Figure 3.22: The linear depolarization ratio derived from nighttime CALIOP backscatter data for 27 July, 1246 to 1247 UTC, and the WRF/Chem model cross-section of PM_{10} concentration at 27 July 1300 UTC	67
Figure 4.1: A normal plot of vertically-integrated WRF/Chem PM_{10} data over the domain for June 25, 2009, 300 UTC.....	70
Figure 4.2: A grid of synthetic pixels overlay the WRF/Chem data over the same domain.....	71
Figure 4.3: Synthetic pixels from the previous figure are averaged	72
Figure 4.4: A raw WRF/Chem plot for 1900 UTC, July 15, 2009, illustrating an optically-thin environment with low amounts of simulated accumulated smoke	74
Figure 4.5: A grid of synthetic pixels overlay the previous plot.....	75
Figure 4.6: Synthetic pixels from the previous figure are averaged to produce a clean-environment test case.....	76
Figure 4.7: A cross-section through part of the clean-environment case.....	77

Figure 4.8: A raw WRF/Chem plot for 600 UTC, June 24, 2009, illustrating an optically-thick environment with high amounts of simulated accumulated smoke.	78
Figure 4.9: A grid of synthetic pixels overlay the previous plot.....	79
Figure 4.10: Synthetic pixels from the previous figure are averaged to produce a smoke-polluted environment test case.....	80
Figure 4.11: A cross-section through part of the polluted-environment case, 24 June, 2009, 600 UTC	82
Figure 4.12: An illustration of discrepancies that occur with regard to wide spatial distributions of smoke.....	83

List of Tables

	Page
Table 1.1: The total number of fires and acres burned, as well as the percentages of human- and lightning-caused fires in Alaska.....	7
Table 2.1: Number of observation sites possessing specified meteorological variables	23
Table 3.1: Summary of skill scores between simulated and observed meteorological data	36

Acknowledgements

I thank: my advisor Nicole Mölders for the opportunity to research within the halls of the Geophysical Institute (GI) and for her guidance; my committee members Kenneth Sassen, Anupma Prakash, and Georg Grell for their direction; the Arctic Region Supercomputing Center (ARSC) team within the GI for support in computational questions; and, the Geographic Information Network of Alaska (GINA) for sharing satellite images and providing assistance.

For supplying meteorological data, I thank the Western Regional Climate Center (WRCC), the National Water and Climate Center (affiliated with the National Resources Conservation Service), Jack Stickel from the Alaska Department of Transportation, the National Weather Service office in Fairbanks, Alaska, and the National Climatic Data Center (affiliated with the National Oceanic and Atmospheric Administration).

For helping me with the thesis, I also thank my friends and colleagues, Ketsiri Leelasakultum, Michael Pirhalla, Huy N.Q. Tran, Mary Butwin, Sean Egan, Colin Triplett, Robin Wing, Karen Barnard, Chris Waigl, Cory Wolff, Mary Haley, and Dennis Shea for their support. I thank Barbara Day, the administrative assistant to the University of Alaska Fairbanks (UAF) Atmospheric Science Program, for processing the necessary forms and requests.

I thank my sister, Erin, for her great encouragement, enthusiasm, patience and love. I thank my parents, Jim and Angela, for their love and encouragement. I thank my grandparents, Fred and Ann Baisch, June Madden, and Harold and Shirley Thieman for their love and support.

Funding was provided by the National Aeronautics and Space Administration (grant number: NASA-NNX11AQ27A), and I thank them for making this possible. Computational resources were provided by ARSC at the UAF – part of the Department of Defense High Performance Computing Modernization Program.

Chapter 1 Introduction

Many Arctic and sub-Arctic regions are experiencing increases in population. For example, the population of the State of Alaska increased by 82% since 1980 (U.S. Census Bureau 2013). Since 2006, the populations of the Canadian territories of Nunavut and Yukon increased by 8.3% and 11.6%, respectively (Statistics Canada 2014). Further increases of population in Arctic and sub-Arctic areas will necessitate additional efforts in wildfire research and adaptation, as wildfires profoundly affect human health, public safety, and environmental systems (Bytnerowicz et al. 2009; Goldammer et al. 2009; Urbanski et al. 2009).

Wildfires not only lead to the destruction of personal and governmental property, but also release numerous chemicals and particulates in the atmosphere, and those constituents can propagate for thousands of kilometers (Wotawa and Trainer 2000; Forster et al. 2001) (Fig. 1.1). For example, wildfire emissions in Alaska in the summer of 2004 were transported through Canada, Wisconsin, and Nova Scotia during a period of 8-10 days (Damoah et al. 2006; Duck et al. 2007).

Smoke constituents, even from long distances (>100 km), can be dangerous for communities as the chemicals and particulates violate air-quality standards and threaten public health and safety (Goldammer et al. 2009). To illustrate, health studies have provided evidence that particulate matter less than or equal to 2.5 μm in diameter ($\text{PM}_{2.5}$), emitted by wildfires, can cause harmful effects after both long and short term exposure, such as increased risks for cardiovascular disease, chronic obstructive pulmonary disease (COPD), and infant mortality (Kappos et al. 2004; Dominici et al. 2006; Miller et al. 2007). The disabled and the elderly, upon exposure to $\text{PM}_{2.5}$, have even greater risks of developing circulatory and respiratory problems (Kappos et al. 2004).

Wildfire particulates also change the visibility, leading to dangers in road and air transportation. An example of this type of incident occurred in the summer of 2013 near Tok, Alaska, where wildfire smoke caused delays in road travel along the Alaska Highway (Delta News Web 2014). Additionally, visibilities of an eighth of a mile and reductions in incoming solar radiation have been reported during times of heavy smoke (Shulski and Wendler 2007).

Wildfires also release large amounts of carbon monoxide (CO) (Wotawa and Trainer 2000; Ottmar et al. 2009). Carbon monoxide causes nausea, vomiting, and headaches, and can prove to be debilitating or fatal if inhaled at high concentrations (Ernst and Zibrak 1998; U.S. EPA 2014a). Aldehydes and ozone, which are also released by wildfires, act as irritants to the

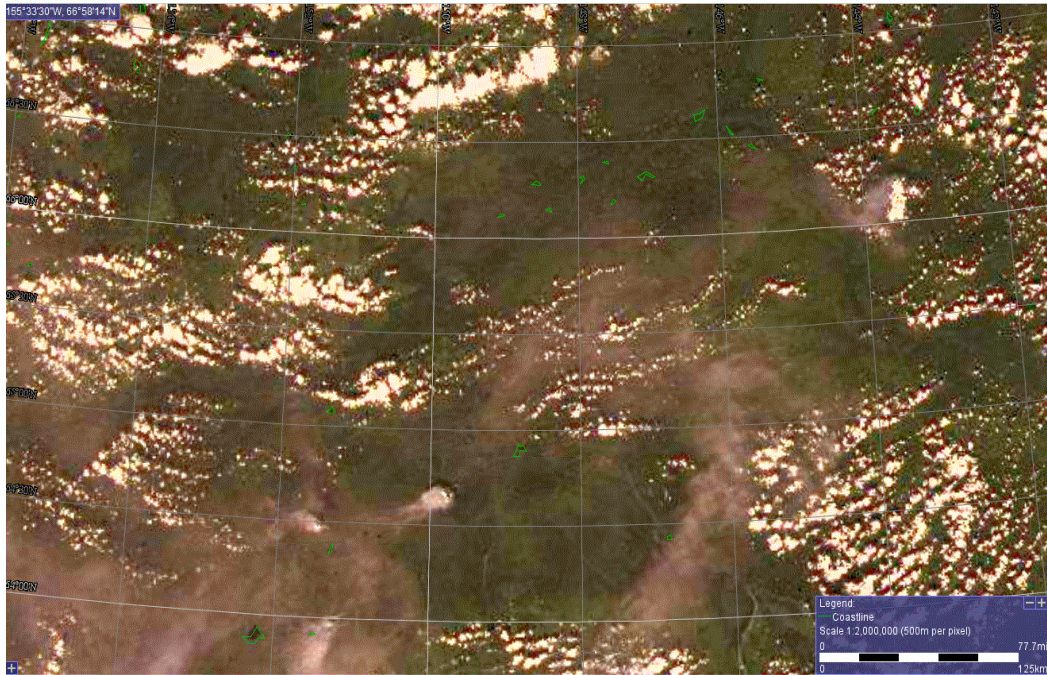


Fig. 1.1 MODIS Aqua image of wildfire smoke propagating through Interior Alaska and Western Canada, taken on 3 July 21:30:29 UTC, 2009 (Geographic Information Network of Alaska 2013). Note that clouds appear brighter than the smoke.

eyes, throat, and nasal passages, and can trigger asthmatic attacks (Reinhardt and Ottmar 2000; Pfister et al. 2008; U.S. EPA 2014b).

Moreover, the scientific community is interested in the effects that wildfires pose to the environment. Wildfires release greenhouse gases (e.g., carbon dioxide (CO₂), methane (CH₄), nitrous oxide (NO_x)) and aerosols that have direct and indirect climatological impacts. Nitrogen oxides and sulfur dioxide (SO₂) provide the foundations needed for acid rain development – a threat to trees, the soil, aquatic flora and fauna, national landmarks, and buildings (Schindler 1988; U.S. EPA 2014c). NO_x and SO₂ are also precursors to aerosol formation, which would again impact the climate.

Wildfires also influence landscape development and land cover type as they affect surface energy fluxes, forest niches, biogeochemical and hydrological processes (Shugart et al. 1992; Mölders and Kramm 2007). In the higher latitudes, fires thaw permafrost and consequently change moisture and precipitation patterns (Chang and Wetzel 1991; Zhuang et al. 2002; Mölders and Kramm 2007). Additionally, wildfires change surface and atmospheric boundary layer (ABL) temperature and humidity through the formation of burn scars (areas of charred land). Burn scars can cause increases in surface temperature (Amiro et al. 1999), the formation of non-classical mesoscale circulations (Mölders and Kramm 2007), and changes to cloud formation patterns (Rabin et al. 1990; O'Neal 1996). The claims regarding changes in mesoscale circulations and/or cloud formation are supported by various modeling studies (Anthes 1984; Pinty et al. 1989; Mölders 2000; Trier et al. 2004; Mölders and Kramm 2007).

To improve the detection and forecasting of wildfire plumes at the high latitudes would create many opportunities. Other than the obvious benefits for scientific inquiry, improvements would help fire fighters, air-quality specialists, meteorologists, and public health authorities quickly respond to fires, and notify the public of dangerous chemicals and particulates entering their communities. Improving the detection of wildfire plumes at high latitudes however would require knowledge of the challenges.

Challenges arise partly because high latitude regions have low population densities. Alaska, the biggest state in the United States, has the lowest population density (U.S. Census Bureau 2013). The Fairbanks North Star Borough has a population of approximately 99,200, and the borough covers 7,361 square miles (Fairbanks North Star Borough 2013). The borough is around 1.1% of the total area of the State of Alaska.

Lower population densities ultimately mean that there is low observational coverage. For example, the closest National Weather Service office to the one in Fairbanks, Alaska is in Anchorage, Alaska, which is 580 km away. There is sparse air-quality coverage within the Fairbanks metropolitan region and even less in surrounding areas. Thus, the difficulty in improving the detection of high latitude wildfire plumes is in finding observations that could provide information in regard to plume particulate propagation and concentration at surface levels.

Remote sensing could help in detecting smoke profiles. Polar-orbiting satellites, such as the Cloud-Aerosol Lidar and Infrared Pathfinder Satellite Observation (CALIPSO) satellite (Winker et al. 2007), can help distinguish smoke aerosols from clouds. However, the gathering of polar-orbiting satellite data is limited as polar-orbiting satellites orbit over an area twice a day. Thus, polar-orbiting satellites lack the spatial and temporal coverage needed to fully understand plume particulate propagation and concentration at the surface.

On the other hand, geostationary satellites, such as the Geostationary Operational Environmental Satellite (GOES), have the ideal spatial and temporal coverage needed to analyze plume particulate propagation and concentration at the surface, and could become a great resource if utilized properly. However, at high latitudes, pixels toward the edges of the geostationary satellite's field of view become distorted and often overlap.

1.1 Work Description

To help address the previous concerns, this thesis will test the following hypothesis: a suitable, four-dimensional dataset of wildfire smoke conditions can be created with WRF/Chem to assess whether it is possible to detect smoke plumes in pixels at the edge of a geostationary satellite's field of view. The dataset must be simulated, as low observational coverage in the high latitudes gives no other alternative. Additionally, this thesis will consider the next generation of radiometers that is to possess resolutions of 1 km at the sub-satellite point over the equator. To test this hypothesis, the following approaches will be conducted.

First, version 3.3 of the Alaska-adapted Weather Research and Forecasting model coupled with Chemistry (WRF/Chem) (Mölders et al. 2011; Peckham et al. 2011) will be used to simulate both the meteorology of Interior Alaska and the propagation of wildfire aerosols. The model's initialization, physics, and chemistry packages will reflect the changes occurring in an atmospheric environment affected by wildfires.

For confidence in the simulated dataset, the output of WRF/Chem will need to be statistically and qualitatively tested. The model's meteorological simulations will be compared statistically to surface observational meteorological data. Moreover, cross-sections of the simulated aerosol profiles will be compared qualitatively to CALIPSO Level 1B products to examine the model's ability to simulate aerosol presence at various altitudes. In some cases, the comparisons between CALIPSO products and WRF/Chem will be supplemented with positive indications of smoke from National Weather Service discussions, METAR reports, and MODIS products.

The extensive evaluation, at the near-surface and in the vertical, will demonstrate that WRF/Chem created a realistic four-dimensional dataset that is physically and chemically consistent. Next, the realistic dataset will be processed through grids of synthetic pixels. The synthetic pixels will be constructed and appropriately sized to represent the distortion of pixel geometry that occurs at the edge of a geostationary satellite's field of view. Then, test cases of clean and smoke-polluted environments will be produced to determine whether clean and smoke-contaminated synthetic pixels can be distinguished. The realistic dataset and the synthetic pixels will demonstrate the possibility that smoke plumes could be detected at the edge of a geostationary satellite's field of view by a radiometer that is sensitive to particles of 10 μm or less in diameter.

1.2 Climatology of Alaska Wildfires

The climatology of Interior Alaska and the causes of wildfires in Interior Alaska and other high latitude regions must be explored for historical and scientific context. Interior Alaska lies in the middle of Alaska between the Brooks Range, to the north, and the Alaska Range to the south. Interior Alaska has a continental climate, and is far from the maritime influence of the Pacific Ocean and the Gulf of Alaska (Shulski and Wendler 2007). Interior Alaska is characterized as having warm summers with low humidity and light precipitation (Shulski and Wendler 2007). Fairbanks, Alaska, the flagship city of the Interior, has a mean maximum temperature of 21.6°C in June, 22.8°C in July, and 19.1°C in August. The mean minimum temperatures are 9.2°C in June, 11.1°C in July, and 7.9°C in August. The summer temperatures in Interior Alaska have the distinction of being the highest in the State (Shulski and Wendler 2007). The mean precipitation in Fairbanks is 35.6 mm in June, 43.9 mm in July, and 44.2 mm in

August. The wind speeds in the Interior are relatively light during the summer, averaging less than 4 m/s (Shulski and Wendler 2007).

In Interior Alaska, thunderstorms occur irregularly during the summer (Shulski and Wendler 2007). These thunderstorms, through low level convergence and graupel formation, are capable of producing lightning, mostly in the afternoon (Sullivan 1963; Houze 1993). Lightning strikes Alaska on an average of 32,400 times per year (McGuiney et al. 2005), and an estimated 90% of all annual lightning occurs in June and July (Reap 1991). Due to Interior Alaska's lightning occurrence, light precipitation values during June and July, and high population of spruce trees and other flammable vegetation (Viereck 1983), the region is susceptible to wildfires (Shulski and Wendler 2007).

Interior Alaska is special for wildfire research, as 96% of all wildfires in the State occur there (Kasischke et al. 2002). While only a small percentage of wildfire ignitions in Alaska are caused by lightning strikes, these lightning-caused wildfires can be responsible for a large amount of burning (Barney 1971). For example, 80% of the total area burned in Alaska from 1950 to 1969 was attributable to lightning ignitions (Barney 1971). Another estimate concludes that fires, caused by lightning, account for 90% of the total burned area annually (Shulski and Wendler 2007).

The Alaska Interagency Coordination Center, an organizational service for all Alaska State agencies that handle wildfires, provides additional annual estimates on fires (Table 1.1). Lightning-induced fires burn more of the total area because lightning can occur far away from human settlements. While lightning-induced fires may go unnoticed or unsuppressed, their plumes may reach communities downwind. Human-induced fires generally occur near more populated areas, where the fires can be suppressed (Shulski and Wendler 2007). In total, there is an annual average of 550 fires, burning an approximate area of 980,000 acres in Alaska (Shulski and Wendler 2007).

Wildfires are partly dependent on synoptic-scale weather conditions. For example, wildfire activity is enhanced through the passages of upper level troughs that carry little moisture (Brotak and Reifsnyder 1977); the dry winds aid the development of fires, and there is little to no precipitation to hinder fire progression. Moreover, Henry (1978) found that 500 hPa ridges in Alaska are accompanied by less mid- and high-level clouds; consequently, there is more solar insolation at the surface. As the ground warms the overhead air and dries the surface, instability rises, and a thermal low develops (Henry 1978). The combination of the weak subsidence at the

Table 1.1 The total number of fires and acres burned, as well as the percentages of human- and lightning-caused fires in Alaska in the last 8 years (Alaska Interagency Coordination Center 2013).

	2013	2012	2011	2010	2009	2008	2007	2006
Total								
Fires	601	416	515	691	527	367	509	308
Acres	1,319,867	286,888	293,018	1,125,737	2,951,593	103,649	649,411	266,269
Percentages								
Human	65%	66%	73%	52%	63%	80%	59%	81%
Lightning	35%	34%	27%	48%	37%	20%	41%	19%

upper ridge and convergence at the surface favors air-mass thunderstorms and the risk of lightning increases as a result. Skinner et al. (2002) found anomalous Canadian 500 hPa ridges and upper blocking patterns can also redirect circulations and deflect moisture-carrying systems, drying the regions below and upstream. Schaefer (1957) proposed that gusty winds, caused by jet streaks, are also associated with increased fire activity.

Wildfires are also related to monthly-to-seasonal variability in climate. In fact, monthly-to-seasonal climate variability can decide whether a fire season is particularly extreme (Bieniek 2007). Bieniek (2007) found that extreme fire seasons correlate with positive temperature and 500 hPa geopotential height anomalies over, or near to Alaska, which is consistent with the findings by Henry (1978). In addition, positively correlated relationships between upper-level ridges and high amounts of burned land, as well as frequent appearances of positive 700 hPa height anomalies, were found in a Canadian study (Flannigan and Harrington 1988).

North American wildfire activity can also be related to teleconnection indices (Johnson and Wowchuk 1993; Hess et al. 2001; Duffy et al. 2005). For example, Johnson and Wowchuk (1993) found a relationship between wildfires and 500 hPa height anomalies in the Pacific North American pattern (PNA). Positive 500 hPa height anomalies, which are correlated with large fire years and summer droughts (Henry 1978; Knox and Lawford 1990), resemble the positive mode of the PNA. Hess et al. (2001) concluded that El Niño episodes lead to decreased precipitation and increased surface heating in Interior Alaska. Fifteen out of the last 17 extreme wildfire seasons in Interior Alaska, prior to 2001, happened during El Niño Southern Oscillation (ENSO) years (Hess et al. 2001). Duffy et al. (2005) showed that seasonal wildfire patterns correspond with positive phases of the East Pacific oscillation (EP), as positive phases create more meridional circulations that give rise to upper-level blocking patterns. Fauria and Johnson (2006) demonstrated an increase in wildfire activity in association with a Pacific Decadal Oscillation (PDO) cold-to-warm phase switch in 1976. Moreover, Duffy et al. (2005) showed that cool-to-warm phase switches of the PDO results in an intensification of the Aleutian low, causing the low to move southeasterly. The low's movement to the southeast created a more easterly component of winds in Interior Alaska, a move that is associated with increased regional droughts. Duffy et al. (2005) showed that cool-to-warm PDO phase switches correlate with the highest record years of burned area, which is consistent with the findings of Fauria and Johnson (2006).

In the climatological field, it is generally agreed upon that the greatest impacts from climate change will occur in the high latitudes, where boreal forests reside, and that boreal

regions are already responding to climate change (Soja et al. 2007). In addition to increasing temperatures (Fig. 1.2), trends indicate an increase of fire frequency for boreal environments (Stocks et al. 2000; Podur et al. 2002). For instance, the area of burned boreal forest in North America has doubled in conjunction with warming trends over the two decades prior to the year 2000 (Stocks et al. 2000). Other studies conducted in boreal Canada and Eurasia support this claim (Shvidenko and Nilsson 1994, 1997; Kurz et al. 1995; Kasischke et al. 1999).

The increase in wildfire frequency, in Alaska and other boreal regions, concerns climatologists because boreal environments store more than 30% of the carbon in the global terrestrial biome (Kasischke 2000) and boreal wildfires spread quickly (Levine and Cofer III 2000). The extremely low temperatures, exhibited in boreal environments during the winter, foster permafrost, which reduces drainage and decomposition rates (Kasischke 2000). During the summer, the upper organic layers of the soil dry, and can serve as potential fuel for fires (Kasischke 2000). Moreover, in densely packed (or close-crowned) forests, dead branches and trees remain intact, which again provides notable amounts of fuel for fires (Cayford and McRae 1983; Viereck 1983). Large boreal forest fires spread rapidly due to the copious amount of fuel sources and, with sufficient energy, can inject smoke high into the troposphere through convective smoke columns (Levine and Cofer III 2000). If the vegetation destroyed by wildfires does not recover, the carbon released into the atmosphere would not be balanced out through regional photosynthetics (Levine and Cofer III 2000).

1.3 Structure of Thesis

The thesis will be structured in the following manner. Chapter 2 will cover: the WRF/Chem model description and the model's physics and chemistry packages; the model domain and initialization; the statistical techniques and synoptic conditions that will be used for model evaluation; the background and historical performance of CALIPSO; and, the design of the synthetic pixels.

Chapter 3 will cover the statistical and the qualitative evaluations of the WRF/Chem model. Statistical evaluations will compare model simulations with surface meteorological stations in the following quantities: temperature; dewpoint temperature; relative humidity; precipitation; wind speed; wind direction; downward shortwave radiation; and, sea-level pressure. Qualitative evaluations will feature cross-section comparisons between simulated aerosol profiles and CALIPSO Level 1B products.

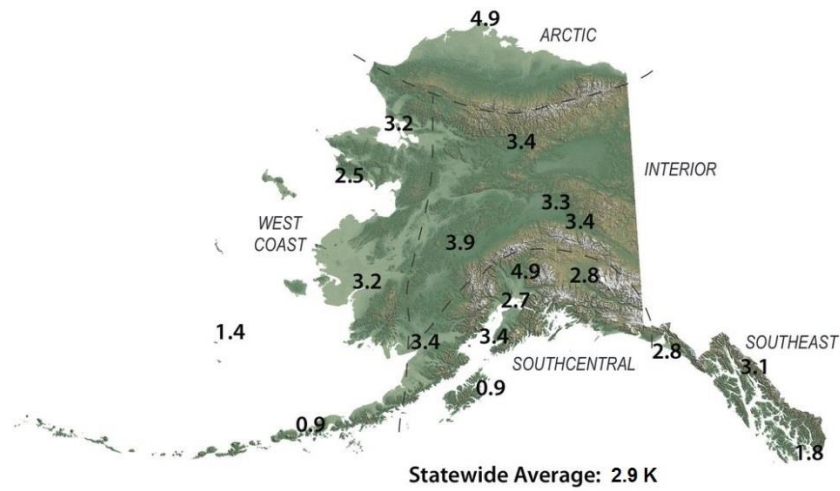


Fig. 1.2 Total changes in mean annual temperature (K) from 1949 to 2012 (Alaska Climate Research Center 2013). Positive numbers indicate increases in mean annual temperature.

Chapter 4 will examine the use of the WRF/Chem data with grids of synthetic pixels. Cases of clean and smoke-polluted environments will be examined to evaluate the distinguishability of the synthetic pixels. Chapter 5 will synthesize results and present conclusions. Moreover, Chapter 5 will present additional ways to improve, clarify, and expand upon the current research.

Chapter 2 Experimental Design

To have a model that simulates wildfire-plume transport, the model's initialization, physics, and chemistry packages must reflect the changes that occur in an environment affected by wildfires. After setting the necessary wildfire specifications, the model will run, and its output will be statistically compared to meteorological observations at the ground. Observational data products and station data are examined for the usability and reliability of the WRF/Chem simulated data. Comparison with the synoptic conditions during the period of interest will allow for additional insight into how the model performs for various meteorological episodes. Additionally, model simulations of smoke plumes will be qualitatively compared in the vertical direction to CALIPSO level 1B products. When the evaluation process completes, the model output will be used as a realistic dataset to assess differences between clean and smoke-contaminated pixels. Moreover, synthetic pixels will be of the size expected for the next generation of radiometers onboard geostationary satellites. The following sections are more complete descriptions of the aforementioned experimental designs.

2.1 Advanced Research WRF

WRF is a highly flexible, state-of-the-art, numerical weather prediction and atmospheric simulation model (Skamarock et al. 2008). It showcases its flexibility through its usage in a wide range of atmospheric phenomena (mesoscale to global), and through its broad range of physical and dynamical schemes.

Used alongside other compatible physical components to produce simulations, the Advanced Research WRF (ARW) dynamic core is utilized in the thesis. The ARW contains compressible, Eulerian, non-hydrostatic equations, which encompass a variety of prognostic variables, such as the Cartesian velocity components, the perturbations of potential temperature, geopotential, dry air surface pressure, and optional inclusions of turbulent kinetic energy, mixing ratios, and chemical species (Skamarock et al. 2008). Vertical coordinates follow a terrain-following system (Fig. 2.1), which is defined by the following (Laprise 1992)

$$\eta = (P_h - P_{ht}) / (P_{hs} - P_{ht}) \quad (2.1)$$

where η is a hydrostatic-pressure vertical coordinate, P_h is the hydrostatic component of pressure, and P_{ht} and P_{hs} represent the hydrostatic component of pressure at the top and surface layers,

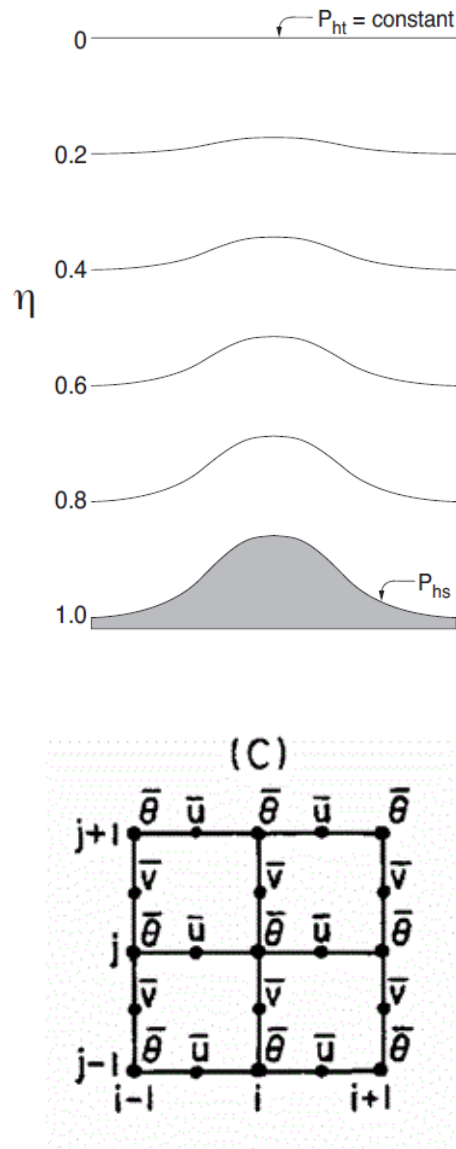


Fig. 2.1 An illustration of a terrain-following coordinate system from Skamarock et al. (2008; top), and an illustration of the Arakawa C-grid staggering class from Pielke (2001; bottom). Top: the letter η represents a hydrostatic-pressure vertical coordinate, and P_{ht} and P_{hs} represents the hydrostatic component of pressure at the top and surface layers, respectively (Laprise 1992). Bottom: dependent variables are represented through velocity components u and v , and θ represents mass-related variables; grid point indices in the x and y directions are represented by i and j , respectively (Arakawa and Lamb 1977).

respectively. Horizontal coordinates are not defined at the same grid point, but rather through the Arakawa C-grid, a class of grid staggering (Fig. 2.1) (Arakawa and Lamb 1977; Skamarock et al. 2008). Temporal integration is implemented through the use of 3rd order Runge-Kutta schemes, which is subsequently attached to a smaller time step for acoustic and gravity wave modes (Skamarock et al. 2008).

Simulations of air-quality, greatly important for the study of wildfire impacts, are complicated (Grell et al. 2005). Without taking into account the chemistry, vital information regarding radiation, photolysis, deposition, emission, and chemical transformations are lost as both the meteorological and chemical processes intertwine (Grell et al. 2005). Fortunately, WRF/Chem considers these processes through the inclusion of gas-phase chemistry, aerosols, dry deposition, photolysis, chemical transformations, and transport components. Simulations of air-quality run with the same transport and physical schemes, which preserves scalars and mass, and all components use the same major time step (Grell et al. 2005).

2.1.1 WRF Physics Packages

The Grell-3 scheme is utilized to parameterize cumulus convection. Both the Grell-3 and Grell-Dévényi schemes rely upon the ensemble mean approach to resolve updrafts, downdrafts, and motions which surround a cloud; however, the Grell-3 scheme no longer utilizes the quasi-equilibrium approach (Skamarock et al. 2011). Like most cumulus parameterization schemes, the Grell-3 scheme acts like a trigger – it only operates on columns if certain heat and moisture levels are met (Skamarock et al. 2008). The scheme also provides convection from rainfall, and allows the effects of subsidence to propagate to adjacent grid columns. The latter attribute is advantageous, as then the scheme becomes more applicable to grid sizes of less than 10 km (Skamarock et al. 2008).

Subgrid-scale cloud microphysics are parameterized by the Purdue-Lin scheme, in which six forms of water substance are considered (Lin et al. 1983; Skamarock et al. 2008). The six forms considered are water vapor, cloud ice and water, rain, snow and graupel. To replicate the complexities that arise from cloud and precipitation formation, various processes are simulated (e.g. ice and snow crystal aggregation, snow and hail accretion, deposition, melting, freezing of raindrops, evaporation, sublimation). Lin et al. (1983) describe an addition of a snow mixing ratio field to the two-dimensional, time-dependent scheme. The addition adds more realism to the precipitation mixing ratio field as the snow mixing ratio addition reduces the amounts of rain and

cloud ice formed early in the cloud's lifespan. Rutledge and Hobbs (1984), who also contributed to the scheme's parameterizations, conducted a series of sensitivity studies with reasonable results in comparison to field measurements, and detailed the impacts of graupel upon collection.

Numerical weather prediction models, like WRF, require calculations of radiative fluxes and heating rates. The Rapid Radiative Transfer Model (RRTM) (Mlawer et al. 1997) is implemented to provide calculations of longwave clear-sky fluxes and cooling rates, as well as the trace gases and microphysical species in 16 spectral bands. The RRTM is based upon the line-by-line radiative transfer model (LBLRTM), a foundation for all radiation codes. The LBLRTM calculates the absorption and emission of radiation by gaseous molecules, and has been validated in comparison to spectral observations (Mlawer et al. 1997). The radiative transfer is performed through the representation of characteristic values within each spectral band.

The Eta similarity scheme (Janjić 2002), based upon the work of Monin and Obukhov (1954), is used to determine surface heat and moisture fluxes (Skamarock et al. 2011). Surface layer schemes, like the Eta similarity scheme, employ friction velocities for the atmospheric boundary layer scheme and the land-surface model (Skamarock et al. 2011). The parameterization of a viscous sub-layer is proposed, and is further modified by Zilitinkevich (1995), who proposes that the sub-layer effects are taken into account through various roughness heights for both temperature and humidity (Skamarock et al. 2011). Concerning the scheme when unstable layers and vanishing wind speeds are present, the scheme by Beljaars (1994) is used as a correction to avoid singularities.

Land surface models (LSMs) use data from surface layer schemes, radiation schemes, microphysical schemes, convection schemes, and land-surface snow-and-soil information to calculate heat and moisture fluxes (Skamarock et al. 2008). To calculate these heat and moisture fluxes, the Rapid Update Cycle (RUC) LSM utilizes the following items (Smirnova et al. 1997, 2000). There is a six layer multi-level soil model with higher resolution in the upper parts of the soil. Additionally, soil moisture and temperature are predicted, while soil ice is diagnosed. This feature is important in Alaska as large parts of soil are underlain by continuous or discontinuous permafrost. Other features include surface balance equations to consider the diurnal changes of temperature and moisture near the soil-atmosphere interface (Skamarock et al. 2008). The LSM also contains a multi-layer snow model and the effects from vegetation (Smirnova et al. 1997, 2000). The multi-layer snow model is well suited for Alaska as snow exists year-round at higher elevations.

The model's atmospheric boundary layer scheme is based on Mellor and Yamada (1982) and Janjić (2002). The Mellor-Yamada-Janjić (MYJ) scheme, as it is called, contains turbulence parameterizations within the atmospheric boundary layer and the free atmosphere (Skamarock et al. 2008). The scheme also determines flux profiles within mixed and stable layers, which provides tendencies of heat, moisture, and horizontal momentum within atmospheric columns (Skamarock et al. 2008).

2.1.2 WRF Chemistry Packages

A regional air-quality model must include a gas-phase chemical mechanism. The distribution of gas-phase species connects to the magnitude of emissions, transport, deposition, and chemical transformations (Stockwell et al. 1990). Stockwell et al. (1990) add that atmospheric transformation rates must include all significant chemical reactions. Thus, the Regional Acid Deposition Model, version two, (RADM2) is applied. RADM2 is widely used to predict the concentrations of air pollutants and oxidants (Grell et al. 2005). Fourteen stable species, four reactive intermediates, and three abundant species (oxygen, water, and nitrogen) compose the inorganic side of RADM2 (Stockwell et al. 1990). Important for the simulation of ozone and acid deposition, the aggregation procedure of volatile organic compounds (VOCs) is included in RADM2, and incorporates 26 stable species and 16 peroxy radicals (Middleton et al. 1990). The aggregation procedure is additionally important for a couple of reasons. First, wildfires release VOCs, which then, in conjunction with nitrous oxides, help produce tropospheric ozone. Moreover, Interior Alaska is densely covered by vegetation, which is another source of VOCs. RADM2 adequately represents the regional air chemistry as is documented by a comparison evaluation with its predecessor RADM (Chang et al. 1987), and through environmental chamber results (Stockwell et al. 1990).

A coupled atmospheric simulation and chemistry model must also include the process of photolysis. Photolysis plays a major role in the chemistry of the atmosphere as sunlight breaks certain molecules into their constituents (at certain spectral ranges). The inclusion of photolysis is especially important for Alaska during the summer, as sunlight is available throughout the entire day. Coupled with hydrometeors, the Madronich (1987) scheme describes the frequencies of photolysis for 21 reactions; and for photoactive molecules, photodissociation rates are given through the integration of the product of the absorption cross section, the quantum yield, and the actinic flux (Madronich 1987; Grell et al. 2005).

2.1.3 Emissions

A global emissions dataset is used to describe anthropogenic emissions. The global emissions dataset comes from the Emission Database for Global Atmospheric Research (EDGAR), version 4.1 (EC-JRC/PBL 2014). EDGAR provides global annual emissions data for several greenhouse and precursor gases on a 1° x 1° grid. The annual emissions dataset is mapped onto the chosen model domain, and is capable of providing both biomass and/or wildfire emissions (Peckham et al. 2011).

Case-specific emissions for biogenic and wildfire emissions are described in the following. Biogenic emissions of isoprene, monoterpenes, and VOCs from plant foliage and nitrogen oxides were calculated online. The calculations of emissions were based upon the U.S. Geological Survey (USGS) land-use calculation and were described by Guenther et al. (1994) and Simpson et al. (1995). Moreover, biogenic emissions were determined by WRF/Chem land temperature and radiation fluxes because of the emissions' dependence upon photosynthetic activity (Guenther et al. 1993).

Wildfire location data, which was needed to properly map emissions onto the domain, was available from the Moderate Resolution Imaging Spectroradiometer (MODIS), specifically from the Fire Information for Resource Management System (FIRMS). Fire location data compared well with thermal anomaly data from the MOD14 algorithm on MODIS (Justice et al. 2002; Grell et al. 2011).

Fire location data from MODIS is then used by the Brazilian Biomass Burning Emissions Model (3BEM) (Freitas et al. 2005, 2007; Longo et al. 2010). 3BEM uses remote sensing fire products to estimate fire emissions and plume rise characteristics. The area of burned land is estimated by the fire sizes, which are retrieved from the selected remote sensing products (Grell et al. 2011). The bottom-up approach (Seiler and Crutzen 1980) is used to calculate emission rates. Additionally, the masses of emitted wildfire tracers (m) within each fire pixel are based upon the following equation (Grell et al. 2011)

$$m^{[n]} = \alpha_{\text{veg}} \beta_{\text{veg}} \xi_{\text{veg}}^{[n]} a_{\text{fire}} \quad (2.2)$$

where α_{veg} is the amount of above-ground biomass available for burning, β_{veg} is the combustion factor, ξ_{veg} is the emission factor, and a_{fire} is the area of the burning land. The equation parameter

is dependent upon vegetation type. Equation 2.2 will help determine the performance and the limitations of the model (see Section 3.2.4).

2.1.4 Model Domain and Initialization

Model runs were performed with a domain covering Interior Alaska with 200 x 160 grid points. The domain captures the cities of Fairbanks, North Pole, Fox, Nenana, and Livengood (Fig. 2.2). The grid increments were 2 km, and the time step for integration was 6 seconds. The runs included 28 vertical layers (from the surface to 100 hPa).

For the meteorological quantities, initial and boundary conditions within the model came from the National Centers for Environmental Prediction (NCEP) 1.0° x 1.0° 6-hour resolution global final analyses (FNL). In regard to chemical fields, initial and boundary conditions were provided by vertical profiles of the average background concentrations for Alaska. At the end of a simulation, chemical fields were then used as initial conditions for the following simulation.

The model runs were performed for 41 days, from June 20, 2009 to July 30, 2009. The meteorological fields were reinitialized every five days. Since WRF starts with zero cloud and precipitation particles, spin-up time is needed to equilibrate the model after initial conditions are first applied, so that the model only reflects the internal forcings of model physics (Cosgrove et al. 2003).

The period of June 20, 2009 to July 30, 2009 was chosen for a couple of reasons. In 2009, more than 2.9 million acres in Alaska were burned, and some of those wildfires occurred within the domain of interest (AICC 2013). For example, the Minto Flats South wildfire started on June 21, 2009, and was responsible for the reported burning of 534911 acres (AICC 2013). The Minto Flats South wildfire started 35 miles west of the Fairbanks Metropolitan Area. Additionally, multiple small fires sporadically occurred north of the Fairbanks Metropolitan Area during the period of interest (AICC 2013). In summary, the selected period and domain would suit well for a wildfire study.

2.2 Model Evaluation Techniques

In numerical modeling, tests are required to determine a model's applicability to real world scenarios, as errors due to initialization, boundary conditions, and model parameterizations impact simulated meteorological variables (Pielke 2001). After running the WRF/Chem model, the simulations will need to be statistically and qualitatively compared to observations.

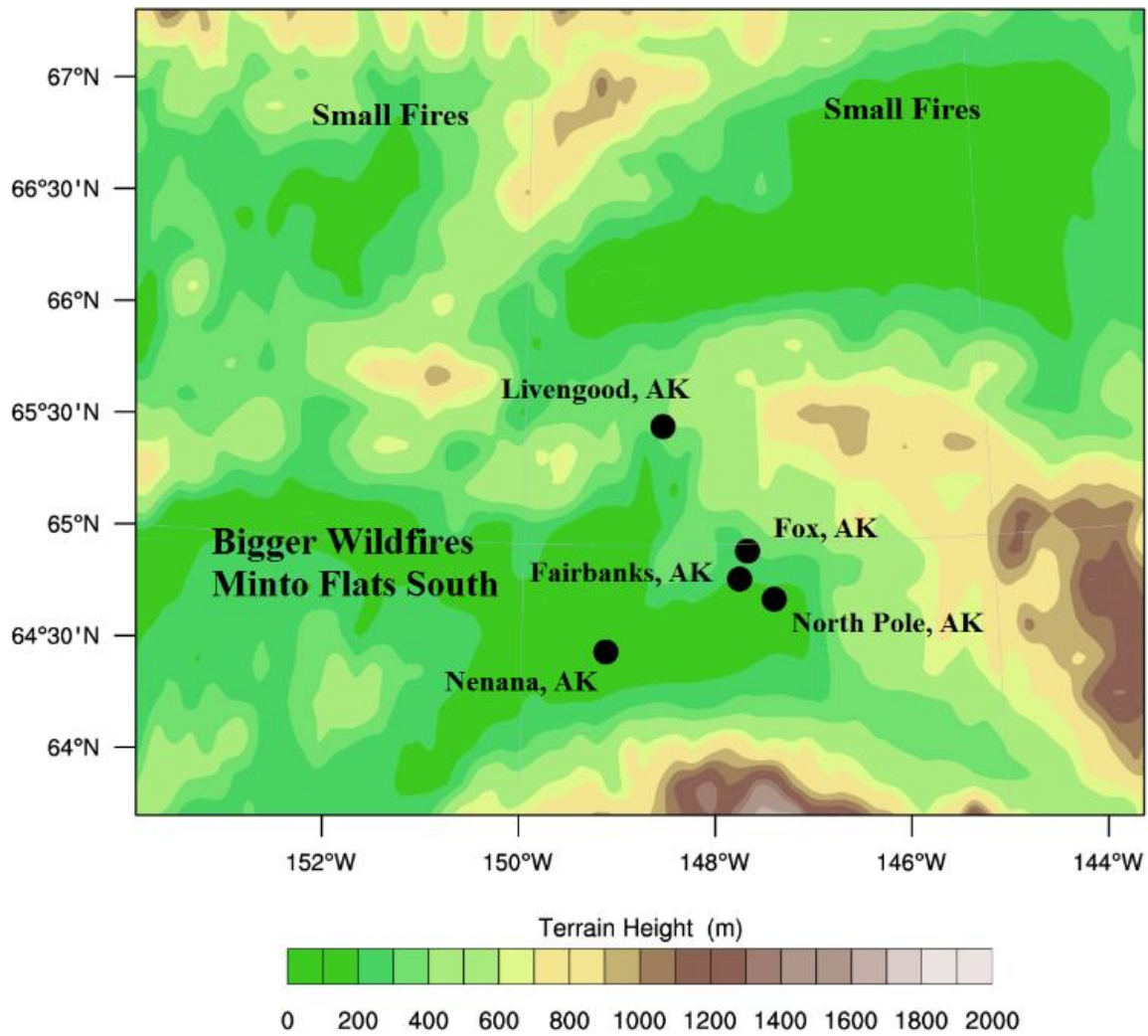


Fig. 2.2 Topography height (m) as used in the model domain, with the cities of Fairbanks, North Pole, Fox, Nenana, and Livengood indicated.

Simulations will be compared with surface meteorological observations of temperature, dewpoint temperature, relative humidity, precipitation, wind speed, wind direction, sea-level pressure, and downward shortwave radiation. Daily maximum and minimum temperatures and daily accumulated precipitation will also be considered. The performance analyses will be conducted on the hourly and daily scale, and results will be compared to other past performances of WRF and other models in similar regions to place the performance into a broader context.

Due to Interior Alaska's low population density and varying topography (Fig. 2.2), observations are scarce. Therefore, observations will be gathered from multiple sources. Hourly measurements were conducted by: 32 remote automatic weather stations (RAWS), provided by the Western Regional Climate Center; 11 automated surface observing systems (ASOS), provided by the National Climatic Data Center; four road weather information systems (RWIS), provided by the Alaska Department of Transportation and Public Facilities; and ten snow telemetry (SNOTEL) sites, provided by the United States Department of Agriculture's Natural Resources Conservation Service.

While there are 57 observation sites in the model domain (Fig. 2.3), some stations do not possess measurements of all the specified meteorological quantities (Table 2.1). To illustrate, all stations have temperature measurements, but only seven stations possess sea-level pressure measurements.

Four statistical skill scores will be used to evaluate the model's meteorological performance: bias, the root mean square error (RMSE), the standard deviation of error (SDE), and the correlation skill score. The measure of bias denotes systematic errors, which occur from model parameterizations, deficiencies, and approximations (Mölders 2008). The bias can be computed simply by taking the difference between the simulated mean and the observed mean. The perfect score for bias is 0; however, a score of zero can still indicate the presence of systematic errors, as the negative differences can equalize positive differences (Mölders 2008). The RMSE also contributes to systematic error analysis, as the RMSE is a tool for measuring accuracy (Anthes et al. 1989). The RMSE is influenced by the bias and the variance, thus large errors in a dataset have higher impacts (Anthes et al. 1989; Mölders 2008). The SDE sheds light upon random errors. These random errors are associated with uncertainty in observations and with initial and boundary conditions (Mölders 2008). The correlation-skill score shows how well the simulated and observed values correspond. A score of 1 indicates a positive relationship, while a score of -1 indicates a negative, anti-correlated relationship.

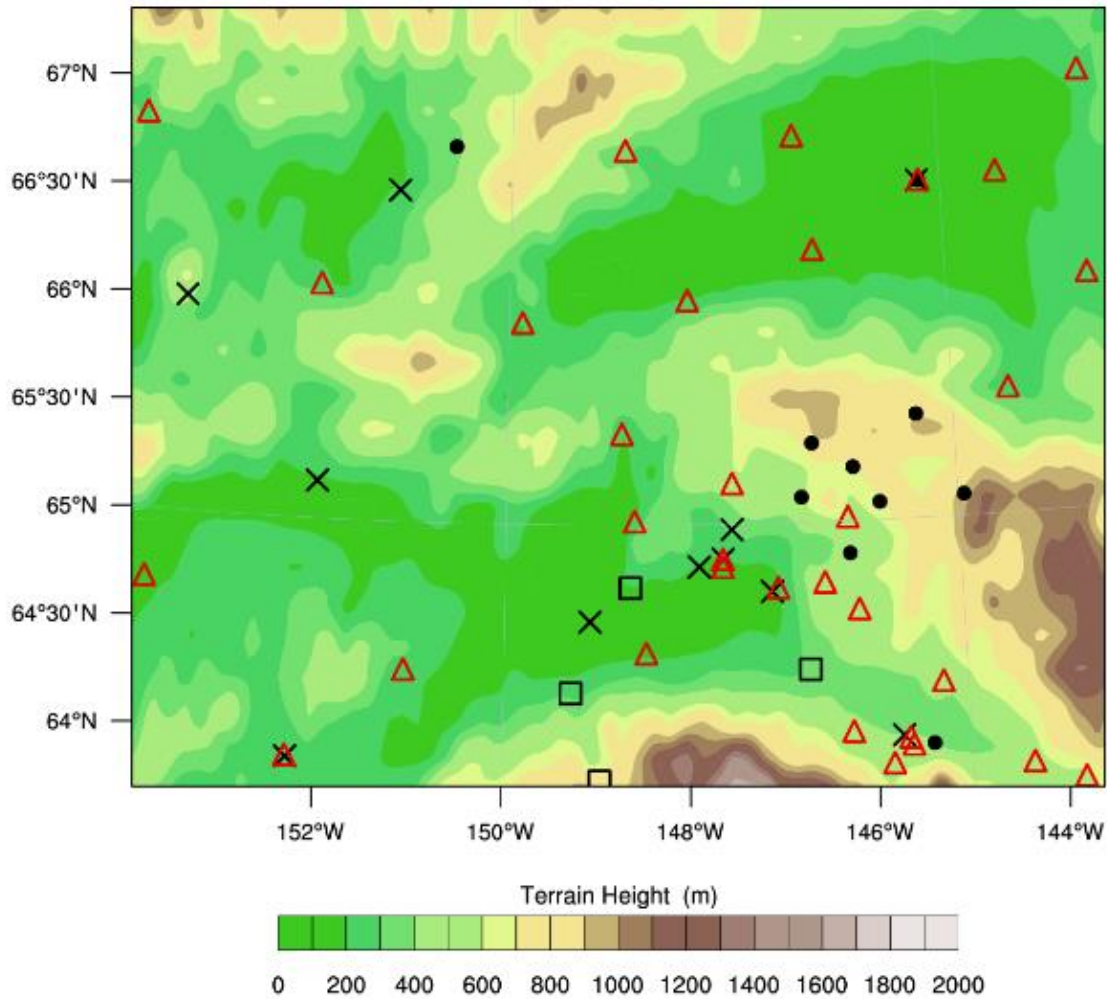


Fig. 2.3 Model domain with WRF/Chem terrain height (m) and locations of observation stations. Red triangles indicate the locations of remote automatic weather stations (RAWS). Black crosses indicate the locations of automated surface observing systems (ASOS). Black squares indicate the locations of road weather information systems (RWIS). Solid, black dots indicate the locations of snow telemetry stations (SNOTEL).

Table 2.1 Number of observation sites possessing specified meteorological variables.

Meteorological Variable	Number of Observation Sites
Temperature	57 out of 57 (100%)
Dewpoint Temperature	46 out of 57 (80.7%)
Relative Humidity	46 out of 57 (80.7%)
Precipitation	32 out of 57 (56.1%)
Wind Speed	47 out of 57 (82.5%)
Surface Pressure	7 out of 57 (12.3%)
Downward Shortwave Radiation	36 out of 57 (63.2%)

Calculations of the scalar mean wind direction will be based upon the work of Mitsuta (1973) and Mori (1986), which corrects for the numerical discontinuity at the north direction (359° to 1°). The differences between the wind directions will be assumed to be less than 180° , which will allow for mean and standard deviation calculations.

2.2.1 Synoptic Conditions

Understanding the synoptic conditions of the period of interest (June 20, 2009 – July 30, 2009) would provide additional chances for qualitative investigation, which is needed to analyze the behavior of the atmosphere during meteorological episodes with wildfire smoke. For example, high wind speeds will spread wildfires and aid fire development. Additionally, higher temperatures lead to the drying of fuel, and higher precipitation (> 7.5 mm/d) will reduce the risk for fires in Interior Alaska (Mölders 2010).

From the beginning of the period of interest to July 1, Interior Alaska is moist. Persistent high pressure systems north of Barrow, Alaska, and frequent surface low pressure landfalls from the Gulf of Alaska and southwestern coasts drive easterly waves closer to the model domain. These easterly waves supply cooler air, moisture and precipitation to Interior Alaska. Following, surface highs and an upper level ridge break the moist pattern and lay foundations for drier weather and suppressed convection, which continues to July 4. Then, the dry period in Interior Alaska is interrupted by the passage of a mild cold front, which sets the stage for warm and humid conditions, as the upper level ridge and associated surface highs regain dominance. While an upper level ridge persists, weak surface lows and frontal boundaries occasionally propagate through the region and bring cloudy conditions. On July 17, the upper level ridge weakens slightly, and a surface low pressure system makes landfall on the western coast of Alaska. On July 19, the surface low pressure system brings cloudiness to Interior Alaska. Shortwaves within Interior Alaska generate a few showers, and a frontal boundary from the Brooks Range brings additional cloudiness. On July 22, an occluded front moves northward into southwestern Alaska and greatly changes wind patterns across much of central and eastern Alaska. The low associated with the occluded front engulfs other adjacent surface lows and brings mixed weather patterns to Interior Alaska. On July 24, a mild surface ridge over southeastern Alaska brings drier and warmer conditions to parts of Interior Alaska; however, a stationary front hangs over the Brooks Range. For the rest of the period of interest, multiple shortwaves and weak low surface pressure

systems increase wind speeds and alter temperature patterns, but do not significantly add precipitation to Interior Alaska.

2.2.2 CALIPSO Components and Products

Since there are no direct methods to observe aerosol presence at various heights, cross-sections of WRF/Chem simulations will be compared to CALIPSO level 1B backscatter and depolarization products (Winker et al. 2007). The CALIPSO satellite and definitions of CALIPSO backscatter will be described.

To understand the complexities that surround Earth's radiation budget and provide greater opportunities to study cloud-aerosol interactions, the CALIPSO satellite was launched in 2006. CALIPSO became part of the "A-Train Constellation" (or "Afternoon Train Constellation"), a collective term for the line of satellites that fly closely in formation around the globe – each satellite with its own unique measurement technologies (Fig. 2.4). This close proximity to other polar-orbiting satellites (GCOM-W1, Aqua, CloudSat, PARASOL, and Aura) allows for the extensive, almost simultaneous observation of atmospheric variables and particulates (McCormick 2005). At an altitude of 705 km, and an inclination of 98 degrees, CALIPSO carries three instruments as part of its payload: the Cloud Aerosol Lidar with Orthogonal Polarization (CALIOP), the wide field camera (WFC), and the Imaging Infrared Radiometer (IIR) (McCormick 2005). This thesis focuses on CALIOP data.

The main instrument onboard the CALIPSO satellite is CALIOP, which provides vertical profiles of the total backscatter at two wavelengths, 0.532 and 1.064 μm (Winker et al. 2007). Backscatter is the primary parameter used for the determination of lidar signal strength, describing the amount of light that is scattered back from a target to the lidar receiver (Wandinger 2005). Lidar backscatter can be used as an indicator of molecular or particle categorization.

Backscatter is determined through the lidar equation, which is defined through the following, at range R (Sassen and Khvorostyanov 2008)

$$P(R)_{\perp, //} = P_0 K \beta(R)_{\perp, //} \exp[-2 \int \sigma(R) dR] / R^2, \text{ integral: } 0 \text{ to } \infty \quad (2.3)$$

where P, the variable of interest, is the received backscattered power, P_0 is the initial power sent by the lidar, K is a constant that depends on lidar performance, β is the volume backscatter coefficient $(\text{sr km})^{-1}$, and σ is the volume extinction coefficient (km^{-1}) . The sign \perp represents the

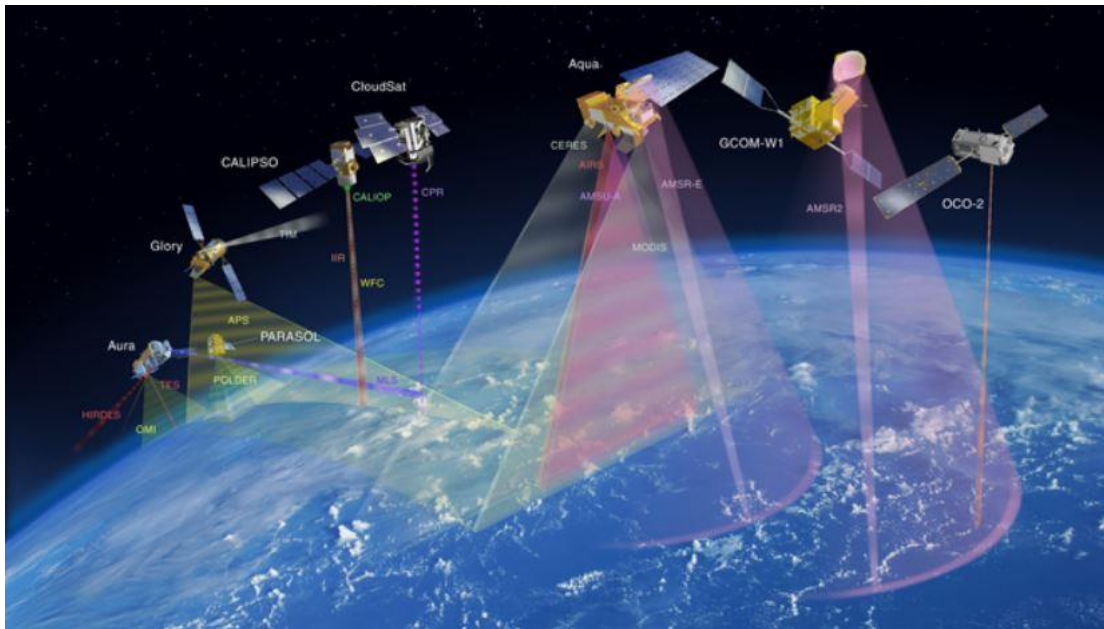


Fig. 2.4 An artist's illustration of the A-Train satellites (NASA 2013). Image courtesy of the National Aeronautics and Space Administration – NASA www.nasa.gov/mission_pages/a-train/a-train.html; retrieved 2014.

orthogonal (perpendicular) polarization plane and the sign // represents the parallel orthogonal polarization plane. In theory, if the particles are perfectly spherical, no backscattering in the orthogonal, or perpendicular plane, should occur (Zhu 2011). Otherwise, irregularly shaped hydrometeors or particles give rise to orthogonal backscattering.

The linear depolarization ratio is an indicator of the shape of particles, and is simply the ratio of the backscattering powers in both polarization planes, perpendicular to parallel, as a function of R (Sassen and Khvorostyanov 2008)

$$\delta = P(R)_{\perp} / P(R)_{//} = [\beta_{\text{mol}}(R)_{\perp} + \beta_{\text{aer}}(R)_{\perp} + \beta_{\text{cld}}(R)_{\perp}] / [\beta_{\text{mol}}(R)_{//} + \beta_{\text{aer}}(R)_{//} + \beta_{\text{cld}}(R)_{//}] \quad (2.4)$$

where subscripts mol, aer, and cld represent the backscattering contributions from molecules, aerosols, and clouds, respectively.

CALIOP's transmitter system consists of two redundant Nd:YAG lasers – one of the lasers is a backup (Hunt et al. 2009). Each laser is frequency-doubled, meaning a laser produces pulses at two wavelengths simultaneously; they also possess beam expanders and a mechanism for steering (Hunt et al. 2009). The beam expanders reduce the output pulse's angular divergence, which resultantly acts as shield against the solar background, and creates a beam diameter of 70 m at the ground (Winker et al. 2007; Hunt et al. 2009). The pulse repetition frequency of the redundant lasers is 20.16 Hz, which translates to a pulse for every 333 m along the Earth's surface (Winker et al. 2007). The lasers are held within containers of dry air at standard atmospheric pressure (Hunt et al. 2009). Linearly polarized pulses, each being 20 nanoseconds, are fired downward through the atmosphere, and a beryllium telescope with a diameter of one meter receives and analyses the backscattered light (Winker et al. 2007). The receiver further reduces the influence of the solar background by establishing a 130 μ rad full angle field of view and utilizing an etalon (an optical interferometer) with a 35 picometer passband (Winker et al. 2007). Moreover, interference filters, one for the 1.064 μ m channel, and a dielectric filter for the 0.532 μ m channel, provide additional support (Winker et al. 2007; Hunt et al. 2009). An onboard computer controls these instruments and processes the information gathered from the receiver.

Throughout the history of CALIOP, the direction of the spaceborne lidar was very important. An exactly nadir orientation would cause heavy saturation, as calm water surfaces would reflect the pulse back to the receiver. From the beginning of the CALIPSO mission to

November of 2007, the direction of the lidar was at an off-nadir angle of 0.3° (Hunt et al. 2009). While the off-nadir angle was suitable for the detection of horizontally oriented ice crystals (HOICs) (Platt 1978), measuring depolarization, and optical depth was greatly problematic, as the ice crystals would produce mirror-like reflections (Hunt et al. 2009). Measurements of depolarization and optical depth became possible after November 2007, when the lidar orientation was switched to an angle of 3.0° (Hunt et al. 2009). This switch allowed for the examination of additional cloud properties and helped CALIOP avoid problematic reflections (Hunt 2007).

Reiterating, there are two redundant Nd:YAG lasers onboard CALIPSO, with one being used as a backup. From the year of its launch to May 2008, the pressure of the container that held the initial laser dropped to 6 psi from 16 psi. This continual loss of pressure necessitated the replacement of the first laser with the backup laser (Hunt et al. 2009). For reference, the loss of pressure did not affect the performance of the initial laser; rather, the loss of pressure made the initial laser susceptible to a corona discharge, which would damage the electronics onboard (Hunt et al. 2009). Thus, the switch from the initial laser to the backup laser commenced during late February 2009, and the backup laser produced the first profiles in mid-March, three months before the period of interest. During the time of the switch, the pressure of the canister that contained the backup laser was approximately 17 psi, which was enough to protect the laser from a discharge (Hunt et al. 2009).

Partly due to the backup laser's inactivity for the first three years of the CALIPSO mission, its performance has been equal to, or in some cases, better than, the initial laser. The backup laser's energy output was higher, and no laser energy adjustments were necessary (Hunt et al. 2009). Additionally, the signal-to-noise ratio (a performance ratio measuring the requested signal to background noise) was higher, and depolarization measurements were at peak performance.

There are other reasons for the backup laser's high performance. A great contributor was the strict solar radiation contamination control, stemming from CALIOP's use of the beam expander, etalon, field of view, and interference filters (Winker et al. 2007; Hunt et al. 2009). CALIOP's designers based these improvements from past developments and orientations of previous spaceborne lidars (e.g. Lidar In-space Technology Experiment (LITE), Geoscience Laser Altimeter System (GLAS)) (McCormick 2005; Hunt et al. 2009).

2.2.3 CALIOP's Application to Model Evaluation

Comparisons between CALIPSO data (backscatter and depolarization) and WRF/Chem cross-sections must be performed along the same latitude and longitude. The comparisons would establish a qualitative assessment of how WRF/Chem simulates smoke plumes as a function of height along a cross-section over the satellite path. In some cases, analyses will be supplemented with MODIS imagery, METAR reports, and National Weather Service discussions of smoke presence.

Generally, the backscattering from clouds tends to play a large role in the depolarization ratio (Sassen and Khvorostyanov 2008). Thus, to find smoke aerosols through backscattering and depolarization, it is wise to find case studies with few to no clouds in the region, as clouds can overshadow smoke signals. However, finding this situation may prove difficult as synoptic conditions give rise to clouds at multiple periods (see section 2.2.1). Thus, it will also help to know what has been reported in past studies in regard to the backscatter and depolarization of smoke.

Murayama et al. (2004) reported that smoke particles generally produce very little to no depolarization, and that older smoke has slightly higher depolarization values. Higher depolarization values for aged smoke may be due to the coagulation of particles, which alters its spherical nature, or that soil matter was lofted into the wildfire plume (Murayama et al. 2004).

Very low depolarization values have been found in multiple studies. For example, a 6% depolarization in the upper part of a smoke layer and even lower depolarization percentages below the active layer were reported (Murayama et al. 2004; Lee et al. 2004). Additionally, depolarization values of less than 3% for fresh smoke and 5% for smoke layers at higher altitudes were reported (Sassen and Khvorostyanov 2008).

2.3 Synthetic Pixel Design

After all statistical and qualitative evaluations, the output from the WRF/Chem model will be used as input into a program that makes synthetic pixels. The lengths of the synthetic pixels must be appropriately sized to represent the expansion that occurs in the high latitudes. For example, a 1 km spatial resolution at the equator, as used by the Geostationary Operational Environmental Satellite (GOES) (Hillger and Schmit 2011), would geometrically expand to roughly 7 to 8 km at the state of Alaska (Liu et al. 2008) (Fig. 2.5). For this thesis, the length of an individual synthetic pixel in the y-direction (north to south), will be approximated as 8 km.

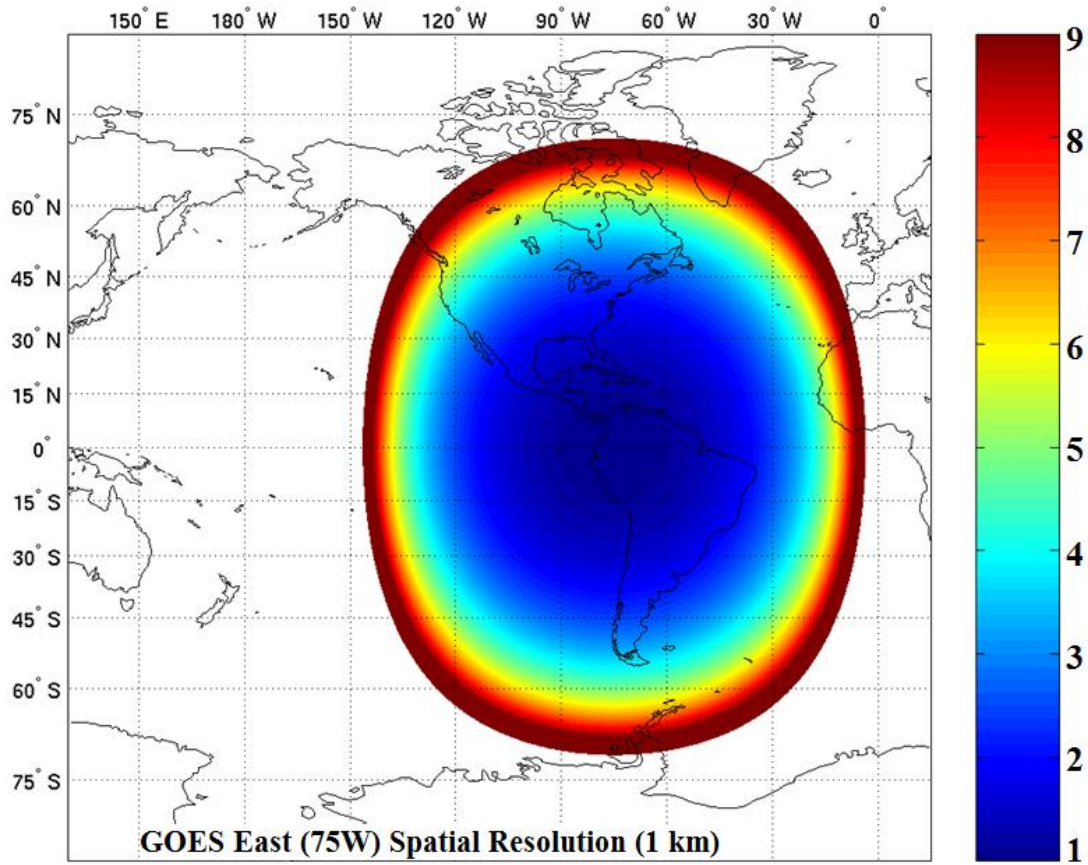


Fig. 2.5 Theoretical pixel sizes adapted for a 1 km nadir field of view by Liu et al. (2008). Approximations of pixel size lengths for Alaska lie within the 7-8 km range to the right.

Ultimately, each synthetic pixel in the model domain will have a length of four grid-increments of 2 km each (Fig. 2.6).

Moreover, the synthetic pixels will need to be widened to not only reflect the distortion of pixel geometry, but also the increase in pixel area. To address the increase in pixel area, another approximation will be applied to the east-west direction; for simplicity, the pixel's width will be slightly longer than the length. Additionally, the distortion of pixel geometry will ultimately stretch the pixel into an 'oval' shape; thus, the synthetic pixels will be created as such. Since multiple grid cells are combined to form one synthetic pixel, the synthetic pixel will not exactly adopt the 'oval' shape; however, the area will be approximately the same (Fig. 2.6).

The plots showcasing the synthetic pixels will need to feature the entire atmospheric column, as that is what a satellite radiometer would encounter. Thus, each synthetic pixel will be vertically integrated across the atmosphere. Additionally, synthetic pixels will be featured across the entire domain, and the PM₁₀ information obtained from the vertically integrated WRF/Chem data within each synthetic pixel will be averaged (Fig. 2.7).

To distinguish between clean and polluted pixels, a threshold should be established due to a lack of better alternatives. The mean of the 2009 non-fire season IMPROVE Denali PM₁₀ data, 1.24 µg/m³, will be used as a basic, background value. The non-fire season data excludes the months of March and April, as Asian dust may propagate into the region of interest (Sassen 2002; Sassen 2005) and skew PM₁₀ values. For consistency, the threshold will also need to adapt to the methodology of vertical integration. Thus, the mean of the non-fire season IMPROVE data will first be applied to the following (Beychok 2005)

$$C_a = C_0 * 0.9877^{(0.01 * h)} \quad (2.5)$$

where C_a is the concentration expressed in mass per unit volume at a certain altitude, C_0 is the mean PM₁₀ concentration in mass per unit volume (in this case, 1.24 µg/m³), and h is the height. The equation by Beychok (2005) expresses how the particulate concentration decreases with increasing altitude.

Concentration values, through Equation 2.5, are vertically-integrated to a maximum height of 2 km through the use of WRF/Chem layer thicknesses. The 2 km height was chosen because stronger wildfires can inject plume constituents past the mixing layer (Labonne et al. 2007). After the vertical integration, a value of 1,800 µg/m² was produced and assigned as the

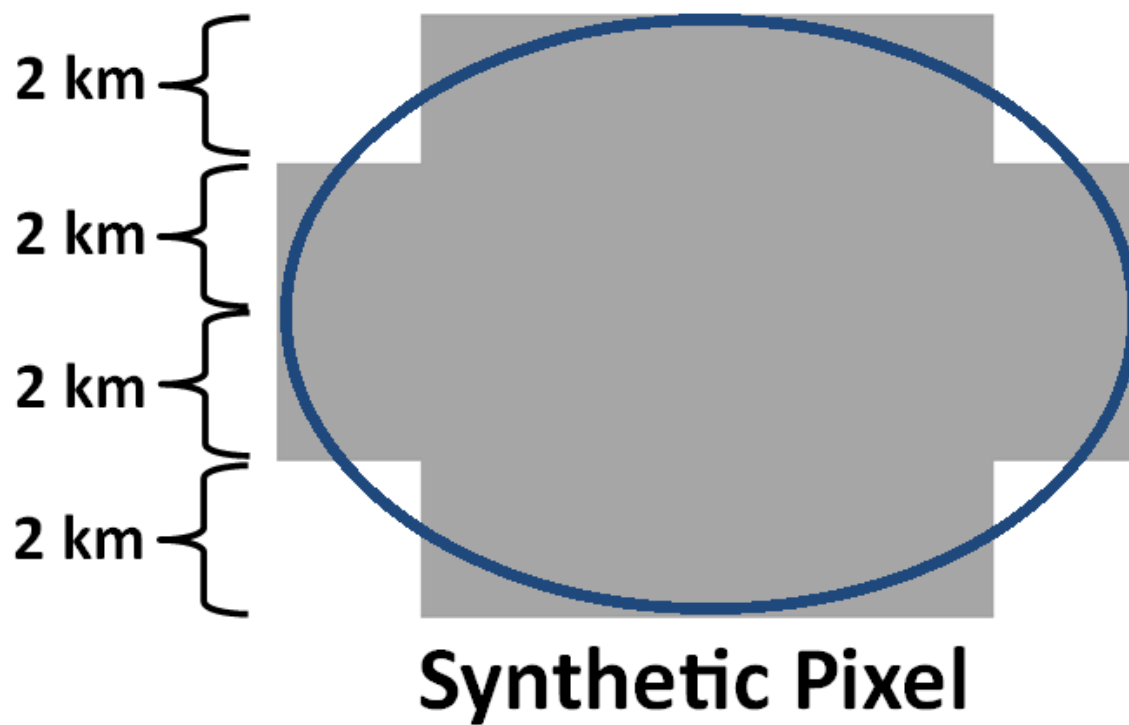


Fig. 2.6 Length scale of a synthetic pixel with corresponding 'oval' shape.

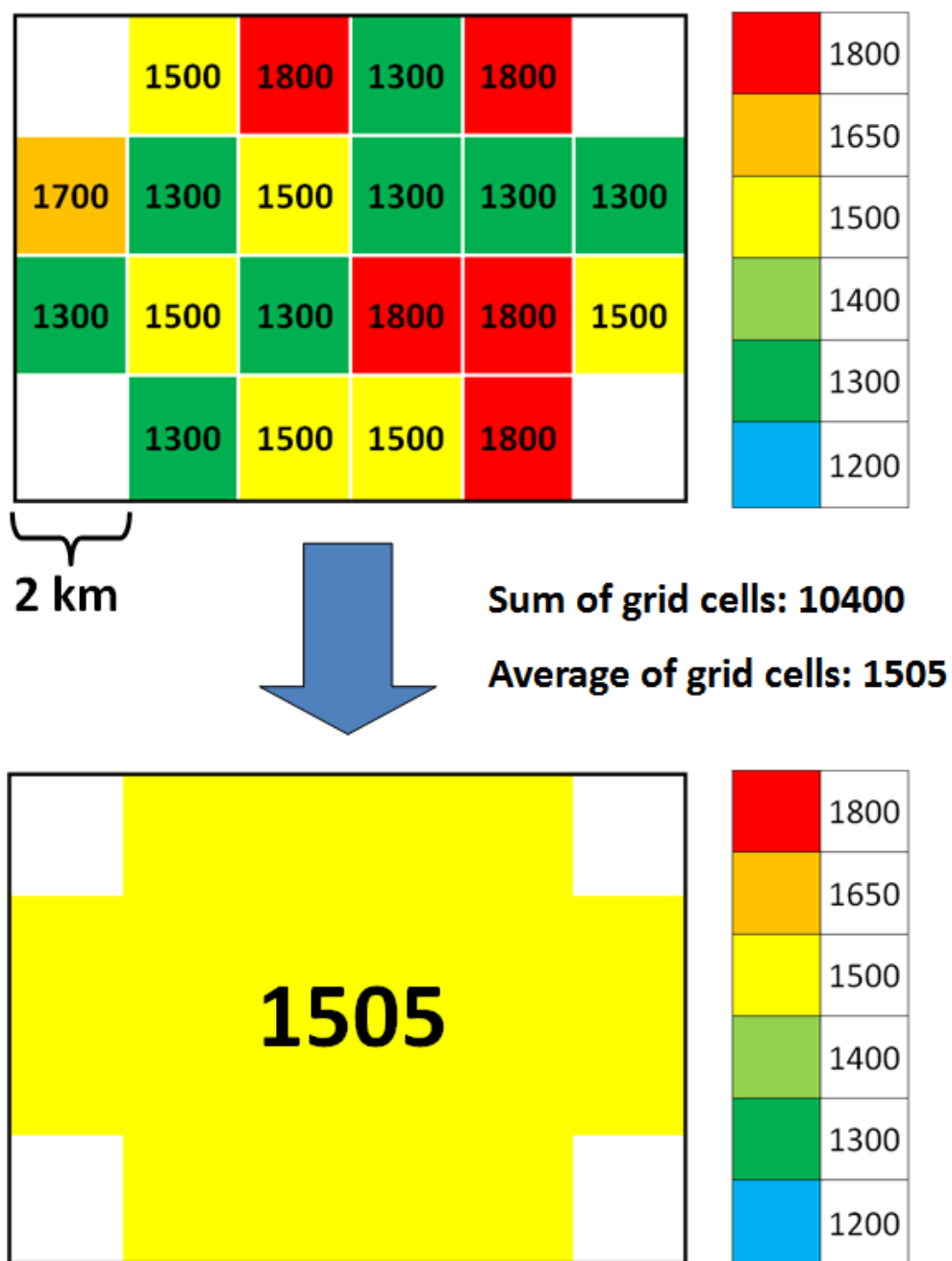


Fig. 2.7 An illustration of the averaging of individual grid cells to create a synthetic pixel, like the one shown in Figure 2.6. Arbitrary values are used. The colors represent the vertically-integrated concentrations within the various grid columns.

threshold. Averaged synthetic pixels that exceed the $1,800 \mu\text{g}/\text{m}^2$ threshold will be distinguished as smoke-polluted.

A couple of test cases will be generated: one in which the PM_{10} concentration is low; and, one where the PM_{10} concentration is high. Additionally, polluted synthetic pixels will be analyzed through a model cross-section to determine the vertical extent of the plume and the applicability to reveal plume presence from the signatures represented by the pixels.

Chapter 3 Evaluation of WRF/Chem by Meteorological Surface Observations and CALIPSO Data

This chapter presents an evaluation of the WRF/Chem model through statistical and qualitative means. WRF/Chem simulated temperature, dewpoint temperature, relative humidity, precipitation, wind speed, wind direction, downward shortwave radiation, and sea-level pressure are compared to ground observations through the bias, the root-mean square error (RMSE), the standard deviation of error (SDE), and correlation.

Later, CALIPSO level 1B products are qualitatively compared to WRF/Chem cross-sections of particulate matter of 10 μm in diameter or less (PM_{10}). To provide additional confidence in simulated smoke presence, these comparisons will be briefly supplemented with MODIS imagery, National Weather Service discussions of smoke, and METAR reports.

3.1 Meteorological Quantities

WRF/Chem simulated quantities are statistically compared to ground observations via the bias, RMSE, SDE, and correlation skill scores. These statistical evaluations are supplemented with comparisons to past WRF/Chem and other model studies in similar regions.

3.1.1 Temperature

Table 3.1 features skill scores associated with temperature and other meteorological quantities for the simulation discussed in this thesis. For hourly temperature, the bias, RMSE, SDE, and correlation are 0.1 K, 3.2 K, 3.2 K, and 0.847, respectively. For daily minimum (maximum) temperature, the bias, RMSE, SDE, and correlation are 1.5 K (-1.0 K), 3.8 K (4.0 K), 3.5 K (3.9 K), and 0.588 (0.722), respectively over all sites for the entire simulation time. Skill scores also indicate an underestimation of the diurnal temperature range. Moreover, WRF/Chem seems to slightly underestimate the spatial variability of observed temperature (Fig. 3.1). For daily maximum and minimum temperatures, systematic errors seem to outweigh random errors.

Throughout the entire period, the model captures the temporal changes of temperature (Fig. 3.1), showing a similar performance to past WRF studies in Alaska (Mölders 2008; Hines et al. 2011; Mölders et al. 2011; Mölders et al. 2012) and other polar regions (Hines and Bromwich 2008). The model also shows a similar performance to a WRF study that was conducted in the Mediterranean (Tuccella et al. 2012). Similar performances were shown through the Fifth-generation Pennsylvania State University – National Center for Atmospheric Research (NCAR)

Table 3.1 Summary of skill scores between simulated and observed meteorological data. Simulated and observed data columns feature the average \pm the standard deviation, the root-mean square error (RMSE), the standard deviation of error (SDE), the bias, and the correlation (R) for hourly and daily averages of available meteorological data over the episode. Meteorological data includes the temperature (T), dewpoint temperature (T_d), relative humidity (RH), wind speed (v), wind direction, sea-level pressure (SLP), downward shortwave radiation (SW), daily maximum temperature (T_{max}), daily minimum temperature (T_{min}), and daily accumulated precipitation.

	Hourly					
	Simulated	Observed	RMSE	SDE	Bias	R
T (K)	16.7 \pm 5.3	16.5 \pm 6.1	3.2	3.2	0.1	0.847
Td (K)	9.2 \pm 3.7	7.4 \pm 3.2	4.1	3.7	1.8	0.452
RH (%)	62 \pm 21	58 \pm 22	18	17	4	0.683
v (m/s)	3.09 \pm 1.65	1.76 \pm 1.79	2.35	1.94	1.33	0.366
Wind Direction ($^{\circ}$)	181 \pm 100	163 \pm 102	114	110	12	0.342
SLP	1013.04 \pm 7.99	1013.41 \pm 8.06	0.9	0.8	-0.4	0.993
SW (W/m^2)	290 \pm 270	220 \pm 232	174	159	71	0.810
Precip. (mm)	0.1 \pm 0.5	0.1 \pm 0.4	0.5	0.5	\sim 0	0.215
	Daily					
	Simulated	Observed	RMSE	SDE	Bias	R
T_{max} ($^{\circ}C$)	22.1 \pm 4.8	23.1 \pm 5.5	4.0	3.9	-1.0	0.722
T_{min} ($^{\circ}C$)	11.2 \pm 3.1	9.6 \pm 4.2	3.8	3.5	1.5	0.588
Precip. (mm)	0.1 \pm 0.2	0.1 \pm 0.2	0.2	0.2	0.3	0.536

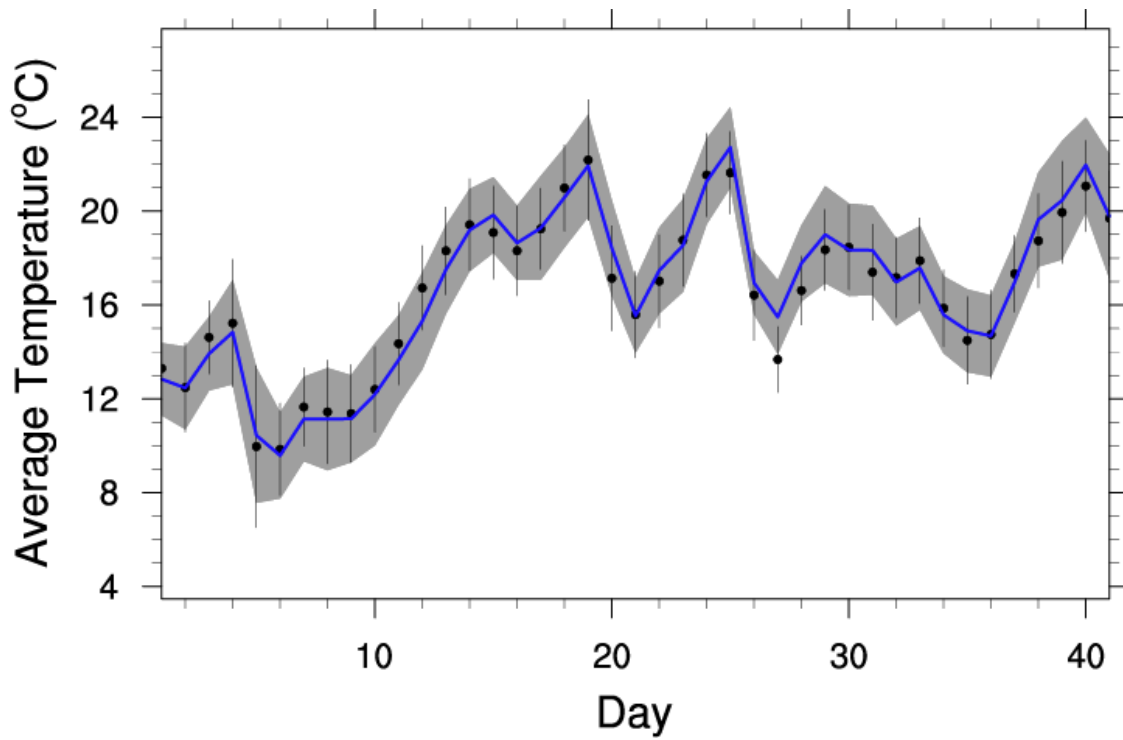


Fig. 3.1 Time series of daily average temperature. Black dots represent the observations with spatial standard deviation averaged over all sites. The solid, blue line represents the model-predicted temperature (averaged over all sites with available data) with corresponding standard deviations in grey shade.

Mesoscale Model (MM5) in Interior Alaska (Mölders and Kramm 2007) and the Great Lakes region (Zhong et al. 2005). In conclusion, the simulation results fall within the range of quality of previous studies.

According to the low positive bias, 0.1 K, the model barely overestimates hourly temperatures. Additionally, WRF/Chem slightly underestimated the daily maximum temperatures and overestimated the daily minimum temperatures (Fig. 3.2); the dampening of the diurnal cycle has been featured in previous WRF studies (Mölders 2008; PaiMazumder and Mölders 2009; Mölders et al. 2011). For daily maximum and minimum temperatures, systematic errors seem to outweigh random errors.

These temperature errors come from a variety of sources. The overestimation of daily minimum temperatures is usually associated with an overestimation of downward shortwave radiation. An overestimation of downward shortwave radiation, due to underestimated cloud cover, leads to increased temperatures during daytime. The underestimation of cloudiness may occur during the first hours of meteorological reinitialization, especially if the reinitialization is on a cloudy day (WRF/Chem starts with zero cloud water and cloud ice). A further source of error comes from the urban heat island effect. Observation stations near the cities of Fairbanks and North Pole may possess slightly higher temperature biases; the model does not take urban effects into account, except that it considers 'urban' as a land-use class. The dampening of the diurnal cycle can also be explained through the following: inadequate soil parameterizations that prevent a full cooling of the surface at night; a vertical diffusion scheme that inordinately brings warm air downward and casts aside cooler air (Manning and Davis 1997); and/or, discrepancies in land use type between the model and nature.

Although the temperature errors are relatively minor, they still propagate into other simulated parameters, such as relative humidity, precipitation, dewpoint temperature, gas phase, and aerosol chemistry. To illustrate, when the model overestimates temperature, more moisture is required for atmospheric saturation. As the model overestimates relative humidity and dewpoint temperature values in comparison to observations, the model will erroneously tend to predict saturation. Furthermore, errors in temperature can modify the reaction rates of various atmospheric chemicals, like ozone; errors in simulated temperature can thus alter the performance of the model's chemical packages.

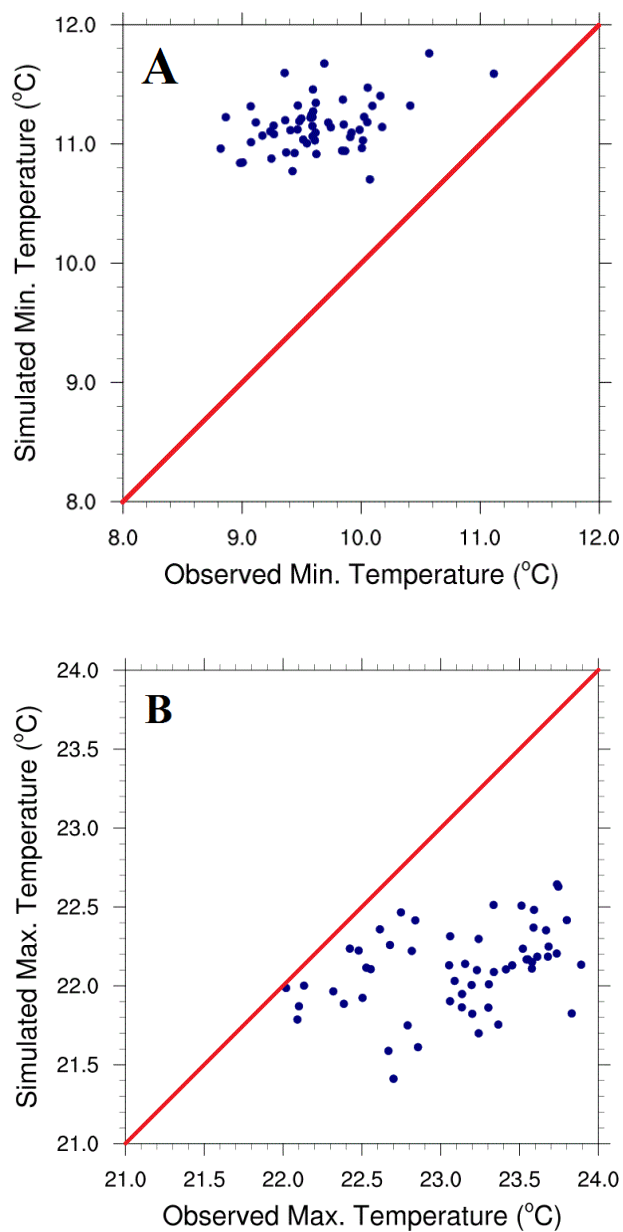


Fig. 3.2 Simulated versus observed daily minimum and maximum temperatures. Panels A and B display the daily minimum and maximum temperatures, respectively. The red line indicates a perfect forecast. Note the temperature difference between the two panels on the axes.

3.1.2 Dewpoint Temperature

WRF/Chem struggles to capture the temporal evolution of the dewpoint temperature, especially near the beginning of the dominant high pressure episode at the beginning of July, near day 10 of the episode (Fig. 3.3). Overall, the dewpoint temperature was overestimated with a bias of 1.8 K, which means the model atmosphere is slightly too wet. In Table 3.1, the RMSE and SDE are 4.1 K and 3.7, respectively; systematic errors have more influence than random errors.

There are many explanations for dewpoint temperature errors. Dewpoint temperature errors are attributable to simulated positive temperature biases. As the temperature increases, more moisture is required to achieve saturation; in turn, the dewpoint temperature must adjust, and becomes positively biased. The dampening of the simulated diurnal temperature cycle should also contribute to the overall error. Furthermore, errors from within the surface layer scheme, herein the RUC LSM, translate to errors in surface heat and moisture fluxes. Surface layer estimates of moisture availability affect simulations of heat and moisture transport in the boundary layer (Manning and Davis 1997), and errors, in this regard, would alter simulations of dewpoint temperature.

The great discrepancy in simulated and observed dewpoint temperature occurs near the beginning of July. The beginning of July follows a light, wet period, where observations have recorded accumulated rainfall up to 0.5 mm. The model simply could have exaggerated the moist environment; ground wetness, coupled with positively biased, rising temperatures, could have pushed the simulated dewpoint higher than in nature. Dewpoint temperature errors also propagate into WRF/Chem simulated cloud formation; higher dewpoint temperatures, along with high simulated wind speeds (see Section 3.1.5), may lead to reduced simulated cloud formation.

3.1.3 Relative Humidity

WRF/Chem overestimates relative humidity with a bias of 4% (absolute) and acceptably captures the temporal evolution (Fig. 3.4). The RMSE, SDE, and correlation are 18%, 17%, and 0.683, respectively (Table 3.1). These skill scores are similar to those from previous WRF studies in Alaska (Mölders 2008; Mölders et al. 2011). The correlation of 0.683 nearly matches that of a WRF/Chem study in Europe that was performed with a 30 km grid resolution (Tuccella et al. 2012). Simulated relative humidity results also slightly outperform both WRF and MM5 models from a summer comparison study conducted over Utah at a 45 km grid spacing (Sauter and Henmi 2004).

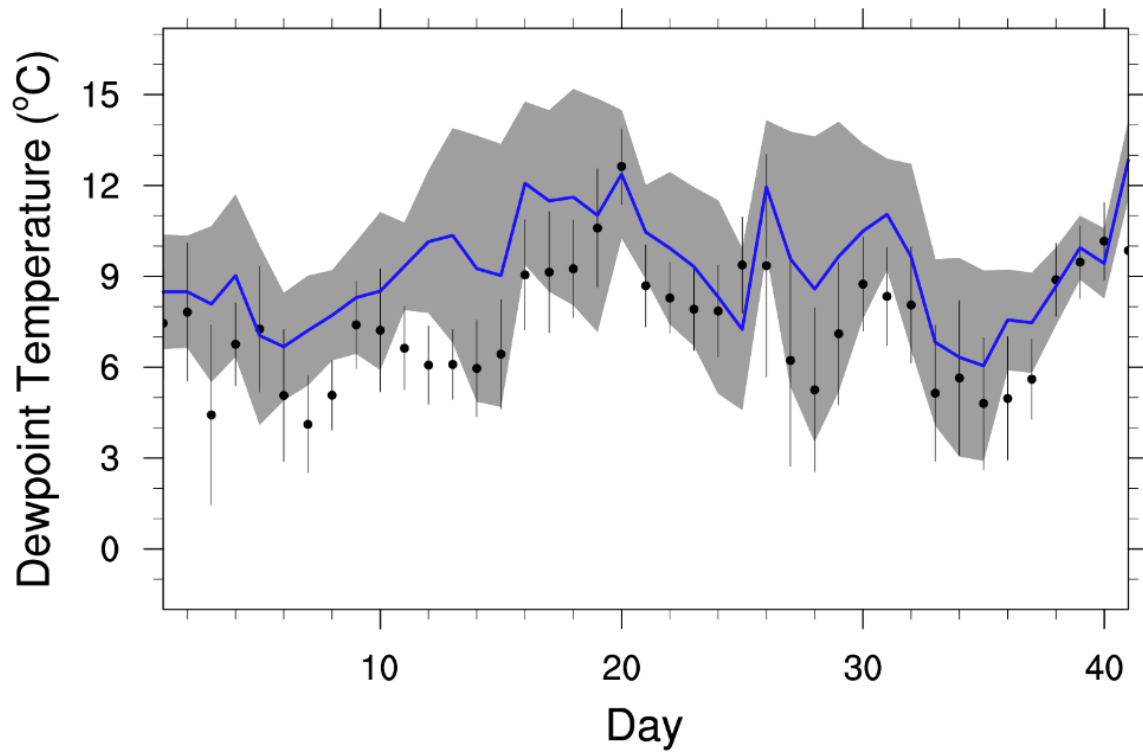


Fig. 3.3 Time series of dewpoint temperature. Black dots represent the observations with spatial standard deviation averaged for all sites. The solid, blue line represents the model-predicted dewpoint temperature (averaged over all sites with available data) with corresponding standard deviations in grey shade.

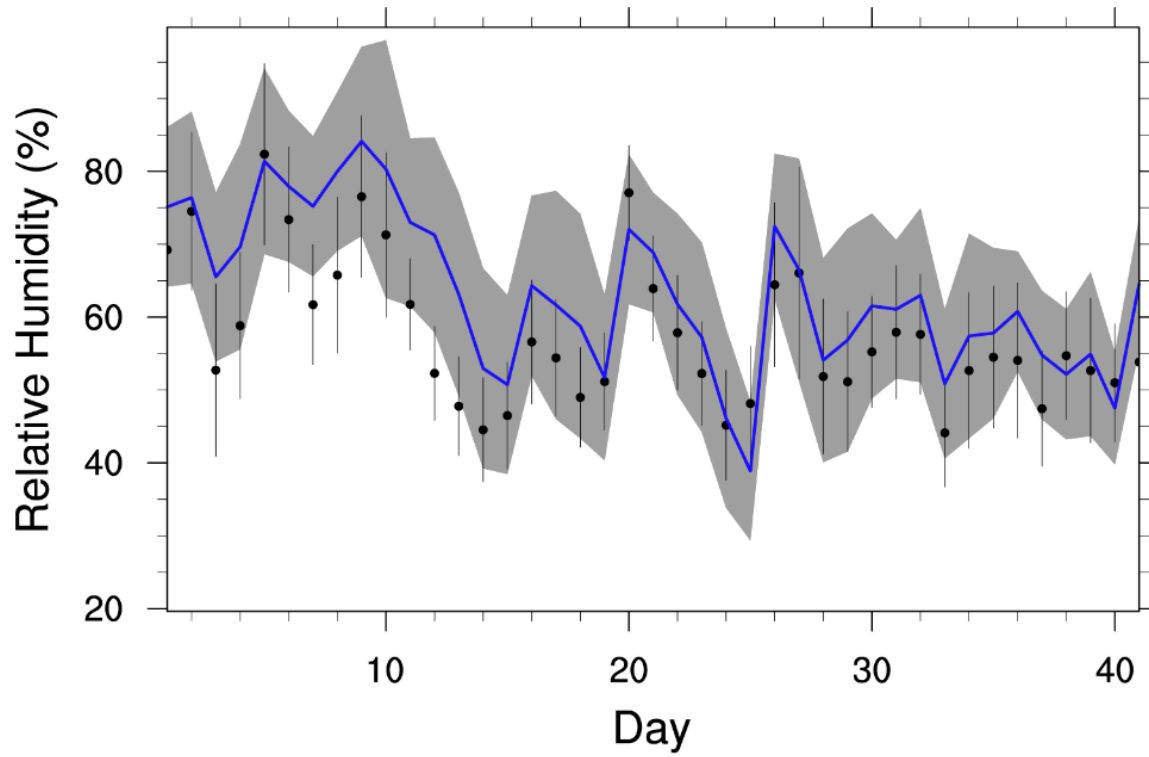


Fig. 3.4 Time series of relative humidity. Black dots represent the observations with spatial standard deviation averaged over all sites. The solid, blue line represents the model-predicted relative humidity (averaged over all sites with available data) with corresponding standard deviations in grey shade.

There are multiple explanations for these results. Reiterating, overestimations of simulated temperature and dewpoint temperature lead to errors in other meteorological quantities; relative humidity is one of those quantities affected, as temperature and humidity are directly related via the Clausius-Clayperon equation. As mentioned with dewpoint temperature, errors originating from the RUC LSM can alter surface heat and moisture fluxes. Concurrently, misrepresentations of land-use type ultimately changes surface parameters from within the RUC LSM, such as heat conduction, soil porosity, and soil thermal conductivity (Smirnova et al. 1997). In a grid-cell, WRF/Chem assumes the dominant land-use type as representative for the entire grid-cell; that assumption can lead to an overestimation (underestimation) of moisture fluxes in regions with high (low) moisture (Avissar and Pielke 1989; Mölders et al. 1996; Mölders and Raabe 1996). Thus, it is also probable that errors in simulated relative humidity are caused by land-use mischaracterizations that have changed heat and moisture interactions amongst the soil and the atmosphere.

3.1.4 Precipitation

WRF/Chem well captures the temporal evolution of precipitation (Fig. 3.5). The model marginally overestimates daily accumulated precipitation in comparison to observations, and the model marginally overestimates precipitation on days of heavy precipitation by roughly 0.1 mm. The bias, RMSE, SDE, and correlation are 0.3 mm, 0.2 mm, 0.2 mm, and 0.536, respectively (Table 3.1). The RMSE and SDE suggest that both systematic and random errors are present. Hourly skill scores show an acceptable performance. For hourly precipitation, the bias, RMSE, SDE, and correlation are ~0 mm, 0.5 mm, 0.5 mm, and 0.215, respectively. The slight overestimations of precipitation is a logical consequence of the slightly wetter atmosphere described earlier.

The WRF/Chem performance, in regard to accumulated precipitation, is similar to results from a previous WRF study in Alaska (Mölders 2008). Daily WRF/Chem accumulated precipitation also slightly outperformed results from a WRF study performed over Anchorage, Alaska, which was conducted without chemical processes and with a resolution of 4 km by Brown (2008). WRF/Chem performance is also similar to results from a WRF study conducted over a limited area domain over Siberia with a 50 km grid increment (PaiMazumder et al. 2012).

A source of error comes from the slight overestimations of temperature, as well as the overestimation of the dewpoint temperature. If the dewpoint temperature is overestimated, then

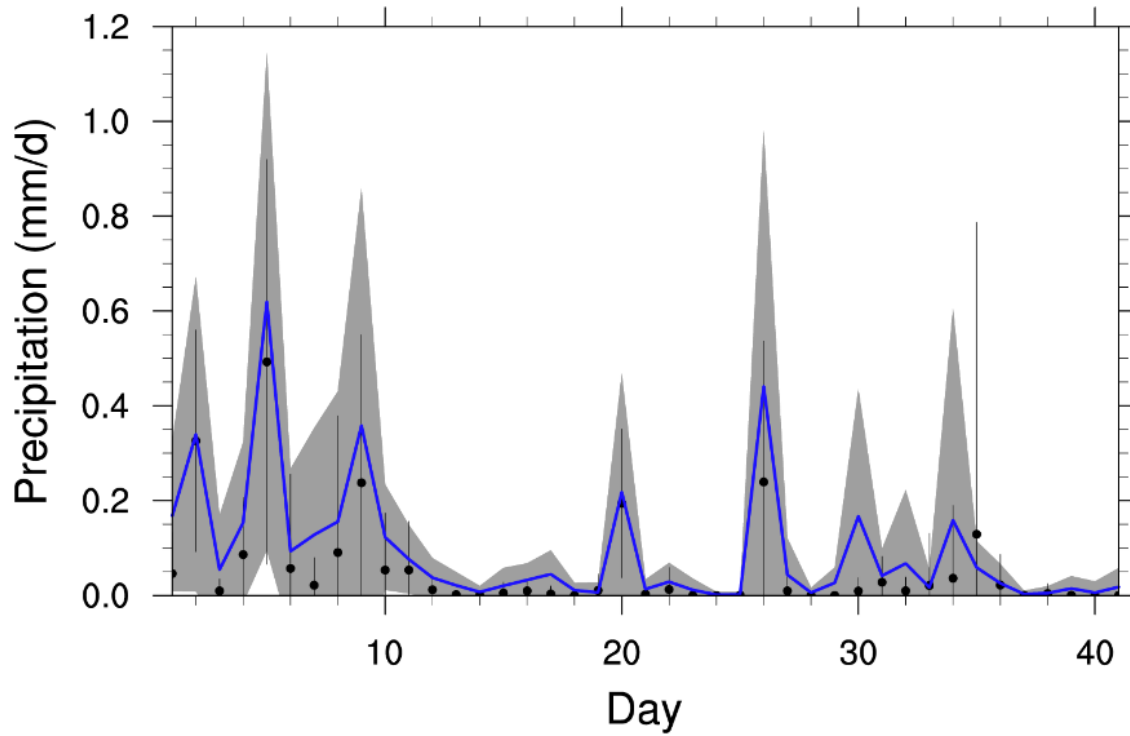


Fig. 3.5 Time series of daily accumulated precipitation. Black dots represent the observations with spatial standard deviation averaged over all sites. The solid, blue line represents the model-predicted daily accumulated precipitation (averaged over all sites with available data) with corresponding standard deviations in grey shade.

relative humidity levels will be affected likewise. As a result, the model's conditions will veer toward saturation, rather than what observations indicate. Other sources of error include the wind speeds in the real world. When the wind speeds are high, rain-gauge errors increase as precipitation does not directly drop into the collection unit (Dingman 2002).

The low correlation is due to the fact that most of the precipitation events are convective precipitation. In these cases, the total amount can be well predicted, but precipitation is predicted in the wrong place; this is due to the model's mishandling of surface heat and moisture fluxes with changes in land-cover type and surface roughness lengths (Loose and Bornstein 1977; Collins and Avissar 1994; Mölders 2012). The low hourly correlation may also be explained through the model's ability to parameterize convective activity at the sub-grid scale. The effects of convective clouds, smaller than the 2 km grid increment, need to be parameterized; current parameterizations are not perfect, and will produce error.

3.1.5 Wind Speed

WRF/Chem simulated wind speeds followed the temporal evolution of observed wind speed, but the model also markedly overestimated observations (Fig. 3.6). The bias, RMSE, SDE, and correlation for wind speed are 1.33 m/s, 2.35 m/s, 1.94 m/s, and 0.366, respectively (Table 3.1); systematic errors carry more influence. These trends were seen in previous polar WRF studies (Mölders 2008; Mölders et al. 2011, Mölders 2013), as well as for other areas with frequent low wind conditions (Sauter and Henmi 2004; Cheng and Steenburgh 2005). In fact, the simulated wind speed outperforms both WRF and MM5 model results from the comparison study performed over Utah by Sauter and Henmi (2004).

There are a couple of explanations for the errors exhibited. The topography within the model is complex, especially in the southeastern portion of the model domain (Fig. 2.2). Complex topography will produce great changes in synoptic circulations; this fact leads to a higher level of wind flow variability over the model domain (Whiteman 2000; Jiménez and Dudhia 2013). Local effects, like wind channeling, add to the difficulty of modeling over complex terrain, as channeling enhances wind speed. The model, as shown previously, averages terrain heights within grid cells, and the observations are of sub-grid scale (a 2 km grid increment). However, the grid cell averaging process smoothes the surface and thus reduces the

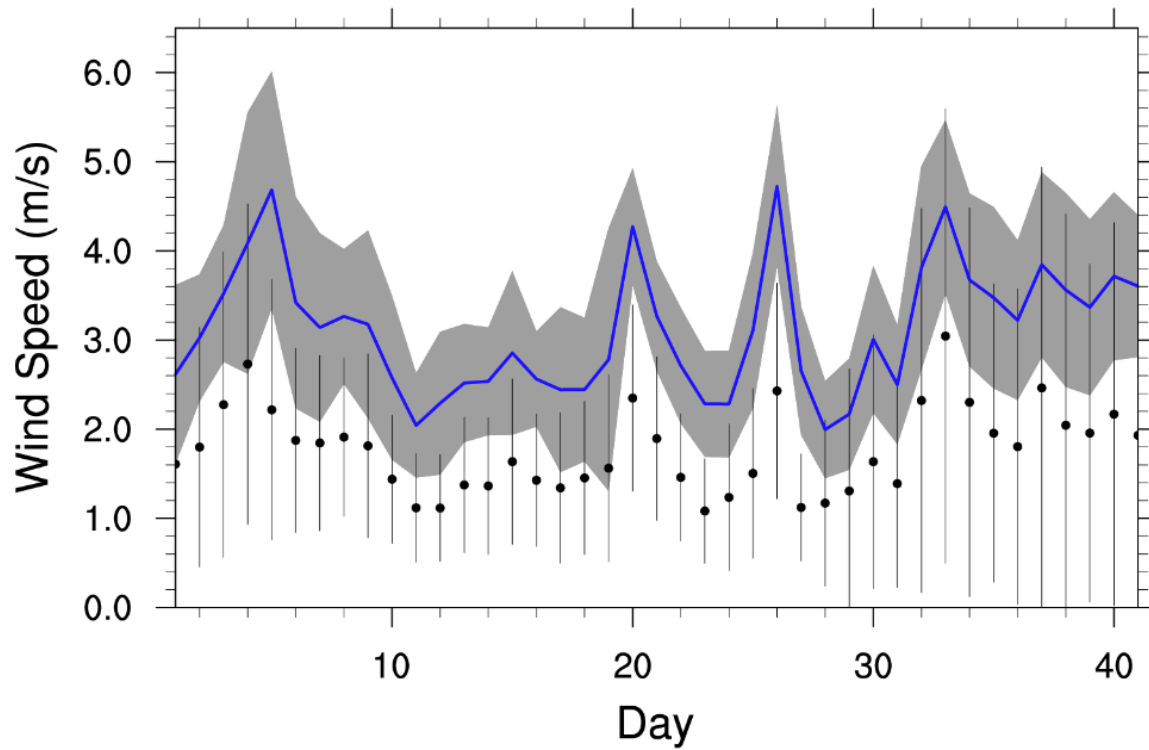


Fig. 3.6 Time series of wind speed. Black dots represent the observations with spatial standard deviation averaged over all sites. The solid, blue line represents the model-predicted wind speed (averaged over all sites with available data) with corresponding standard deviations in grey shade.

complexity of the surface roughness. Consequently, simulated wind speeds are typically higher than observed wind speeds. Wind speed errors also propagate into WRF/Chem simulations of cloud presence; wind speeds that are too high may lead to rushed cloud transport and less cloud formation.

3.1.6 Wind Direction

WRF/Chem captured the temporal evolution of wind direction (Fig. 3.7), and the model performed similarly to past studies (Mölders et al. 2011, 2012). The observed and simulated scalar mean wind directions were 163° and 181° , respectively. The bias, RMSE, SDE, and correlation were 12° , 114° , 110° , and 0.342, respectively. Systematic errors seem to be more common than random errors.

Errors in simulated wind direction are common with areas of complex terrain. Wind direction has a wide variability due to channeling and turbulence effects. Moreover, the topography within the model domain is highly variable, and the grid increment of the model (2 km) cannot fully represent the complexity at the surface. Additionally, model smoothing of the surface prevents the model from fully realizing the changes in surface roughness, which would alter the wind direction in reality.

3.1.7 Downward Shortwave Radiation

The model overestimated daily accumulated downward shortwave radiation with a bias of 71 W/m^2 , and followed the temporal evolution in some cases (Fig. 3.8). The RMSE, SDE, and correlation are 174 W/m^2 , 159 W/m^2 , and 0.810, respectively, illustrating that systematic errors are largely at play (Table 3.1). Overestimations of this quantity have been found in other WRF studies (Mölders 2008; Hines et al. 2011; Mölders et al. 2011). The model seems to also have missed the downward trend observed near the end of the period.

There are a couple of reasons for error. The dampened diurnal temperature range, along with the dewpoint temperature and wind speed, may lead to a decrease in the amount of cloud coverage, which would lead to an overestimation of downward shortwave radiation. Comparisons with MODIS imagery (see Section 3.2) also illustrate that WRF/Chem underestimated cloud presence. The overestimation is also partly attributable to the reinitialization of meteorology, with zero cloud-water and cloud-ice every five days. On cloudy

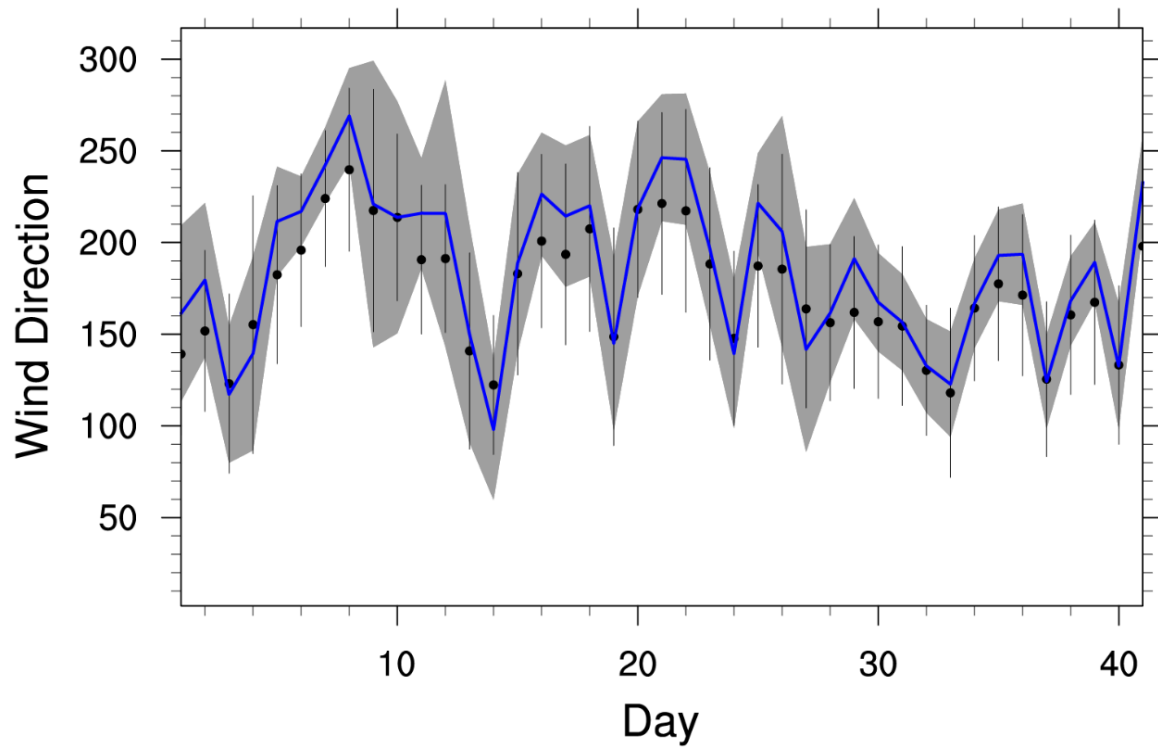


Fig. 3.7 Time series of wind direction. Black dots represent the observations with spatial standard deviation averaged over all sites. The solid, blue line represents the model-predicted wind direction (averaged over all sites with available data) with corresponding standard deviations in grey shade.

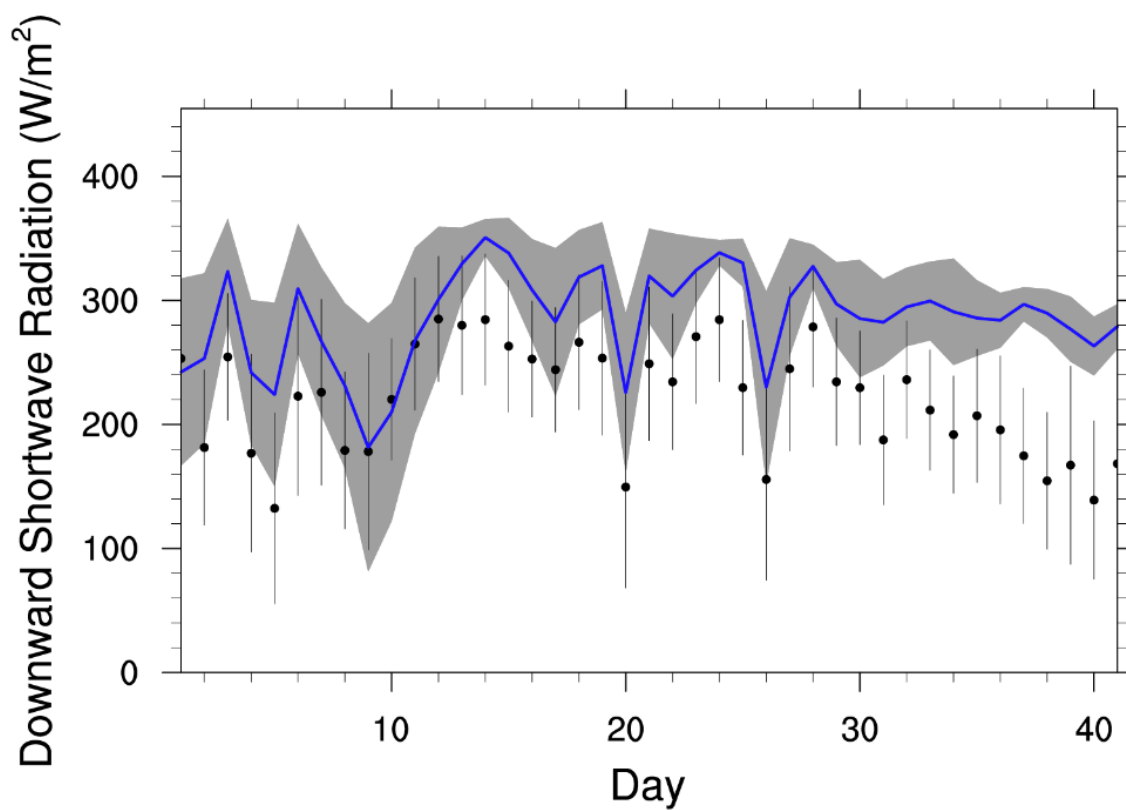


Fig. 3.8 Time series of daily accumulated downward shortwave radiation. Black dots represent the observations with spatial standard deviation averaged over all sites. The solid, blue line represents the model-predicted daily accumulated downward shortwave radiation (averaged over all sites with available data) with corresponding standard deviations in grey shade.

days, clouds will not be fully formed during the first hours of reinitialization, hence incoming shortwave radiation is too high (Mölders and Kramm 2010; Mölders et al. 2011; Leelasakultum et al. 2012). Moreover, simulated sea-level pressure (see Section 3.1.8) shows a low-pressure system moving through the domain near the end of the period before simulated downward shortwave radiation started to experience issues; reiterating, while sea-level pressure performed well, errors in simulated dewpoint temperature and wind speed may reduce simulated cloud formation and rush cloud transport. Errors in simulated downward shortwave radiation will propagate into simulated temperature, photolysis rates, and hence gas phase chemistry.

Concurrently, biomass burning – a wildfire in this case – emits large amounts of black carbon (Grell et al. 2011). Parameterizations of radiative effects upon black carbon will introduce error.

3.1.8 Sea-level Pressure

WRF/Chem simulated sea-level pressure followed the temporal evolution of observed wind speed quite well (Fig. 3.9), and sea-level pressure possesses the highest correlation skill score, 0.993 (Table 3.1). WRF/Chem slightly underestimated sea-level pressure with a bias of -0.4 hPa. The RMSE and SDE are 0.9 hPa and 0.8 hPa, respectively, showing that systematic errors outweigh random errors. Simulated sea-level trends were also seen in previous WRF studies in Alaska (Brown 2008; Porter 2009; Mölders et al. 2011). Trends outperform a WRF study conducted over Siberia that was conducted with a 50 km grid increment (PaiMazumder et al. 2012). Additionally, simulated sea-level pressure slightly outperforms both Polar WRF and MM5 model results from a June study performed in Greenland (Hines and Bromwich 2008).

There are many sources of error. While WRF/Chem seems to trend excellently with observations, it must be noted that there are only seven stations in the model domain that observe sea-level pressure (Fig. 3.10). Additionally, the pressure observation stations are not evenly distributed through the domain; some of them lay close to the city of Fairbanks. The distribution of pressure sites has been shown to affect regional averages (PaiMazumder and Mölders 2009). Concurrently, all pressure observing stations are on low terrain, meaning that high-terrain areas are not represented well by the pressure observational network. More systematic errors arise from the conversion of the WRF/Chem surface pressure to the sea-level pressure, through the use of the barometric equation, and the difference between simulated and observed terrain heights.

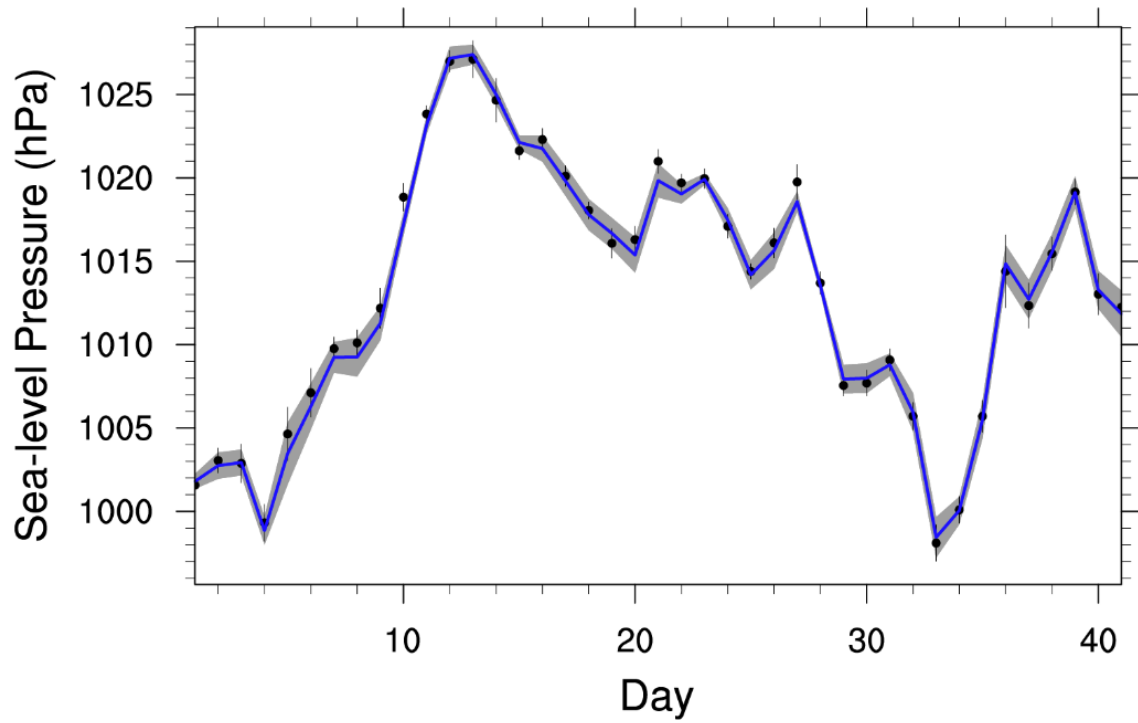


Fig. 3.9 Time series of sea-level pressure. Black dots represent the observations with spatial standard deviation averaged over all sites. The solid, blue line represents the model-predicted sea-level pressure (averaged over all sites with available data) with corresponding standard deviations in grey shade.

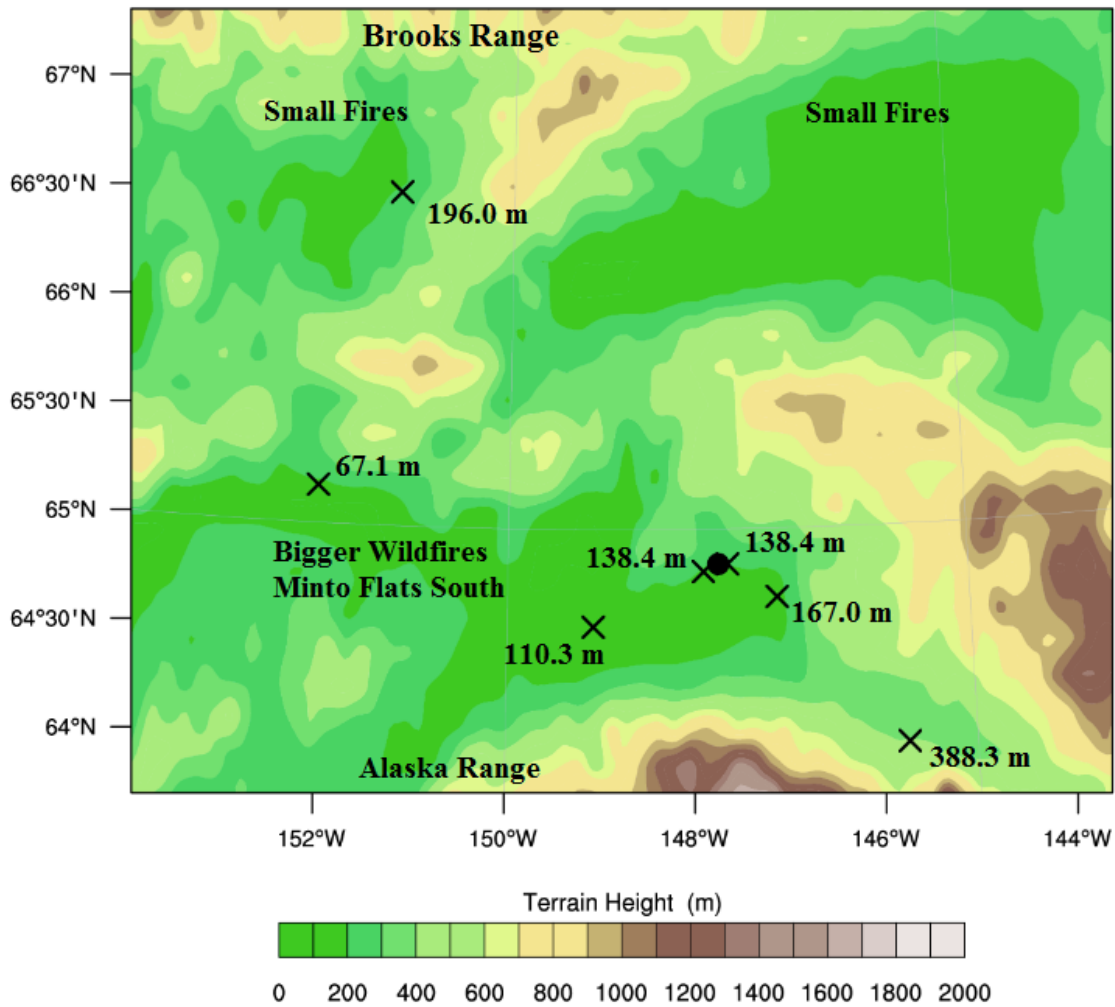


Fig. 3.10 Model domain featuring the locations of all sea-level pressure stations with their real terrain heights (m) in bold, black font. Model terrain height (m) is represented by the color code. Black crosses specifically indicate that these stations are automated surface observing systems (ASOS). The black dot indicates the location of Fairbanks, Alaska.

WRF/Chem terrain heights are higher than the real-world ground observation heights for all pressure stations (Fig. 3.10). Terrain height discrepancies are caused by the averaging of terrain heights within grid cells, a common characteristic shared by all grid models. These misrepresentations, particularly, can lead to errors in pressure gradients. Moreover, the fact that WRF/Chem overestimated wind speed points toward overestimations of pressure gradients.

3.1.9 Conclusions on the Meteorological Performance

The model mostly captures the temporal evolution of meteorological quantities. At the hourly time scale, WRF/Chem overestimates ambient temperature, dewpoint temperature, relative humidity, wind speed, wind direction, downward shortwave radiation, and precipitation. It slightly underestimates sea-level pressure. The model also dampens the diurnal cycle by overestimating minimum temperature and by slightly underestimating the maximum temperature.

There are several over-arching themes of error. One form of error stems from the methodological clash between observational point measurements and simulated volume (T , T_d , v , RH) and area averages (precipitation, SLP, SW). To illustrate, an observation station collects meteorological information from a specific point in the model domain. This simulation used 2 km grid-cell increments, and the meteorological information pertaining to a grid cell is averaged. Extremes and variations, pertaining to individual grid cells, can skew averages, thus creating differences between the simulated and the observed quantity. Meteorological information is not the only concern; terrain height information and land-cover type were affected in a similar manner, hence leading to errors in the fluxes of momentum, sensible heat, latent heat, and matter. For the quantities that depend on those fluxes, there will be errors.

For example, the average difference between observed and WRF/Chem terrain height is 78.92 m. In WRF/Chem, the grid-cell terrain height of 32 stations is higher than what is reported for ground sites, five of which are more than 100 m higher. The WRF/Chem grid-cell terrain height of 25 stations is lower than what is reported for ground sites, nine of which are more than 100 m lower. Only one station's terrain height is more than 500 m lower than the grid cell terrain height.

Land-cover types within grid-cells affect meteorological quantities. For example, the upward flux of shortwave radiation is determined by surface albedo (Skamarock et al. 2008), which largely depends upon how the ground is utilized or composed. To illustrate, an urban area, like downtown Fairbanks and its surrounding neighborhoods, would possess different

meteorological characteristics than would the lush, green boreal forests outside of city limits. Land characteristics are determined by the dominant land-use type, and hence the footprint of land-use around a ground observation site may be a different land-use type than that assumed to be representative for the grid-cell.

An additional source of error is due to the fact that a wildfire is present in the domain. Wildfire aerosols released into the atmosphere can directly and indirectly affect the meteorology in the following ways: reducing incoming solar radiation, thus affecting surface temperature; decreasing the cloud drop size, thus altering precipitation patterns; and increasing the atmospheric instability (Zhang 2008; Zhang et al. 2010). WRF/Chem parameterizes these aerosol mechanisms, and resultantly, systematic errors will be introduced. Furthermore, the simulations do not consider the buoyancy related to the wildfire.

3.2 Comparison of CALIPSO 1B Products and WRF/Chem Cross-sections

Three comparisons between CALIPSO 1B products and WRF/Chem cross-sections will be presented: 7 July at 1311 UTC; 11 July at 1246 UTC; and, 27 July at 1246 UTC. As the WRF/Chem data are archived every hour, the WRF/Chem data that are temporally archived closest to the CALIPSO passage will be used; thus, there will be a small temporal difference. Comparisons are supplemented with MODIS imagery, METAR reports, and National Weather Service discussions to provide additional confidence of smoke presence. The supplied MODIS imagery features scans closest to the times of interest.

3.2.1 July 7 Case

The MODIS imagery and CALIPSO scan track are featured for the 7 July case in Figures 3.11 and 3.12. METAR reports and National Weather Service discussions indicate smoke presence throughout the day. CALIPSO products should feature predominately wildfire-related aerosols as the scan track is outside of the influence of the city's emissions.

The total backscattering plot indicates light backscattering between 64.24 and 63.70 N latitude (Fig. 3.13). Following, the perpendicular backscattering plot indicates near to zero perpendicular backscattering where light total backscattering occurs (Fig. 3.13). In the same area of interest, the linear depolarization ratio is close to zero (Fig. 3.14), which is consistent with what has been reported in smoke depolarization studies (Murayama et al. 2004; Lee et al. 2004; Sassen and Khvorostyanov 2008).

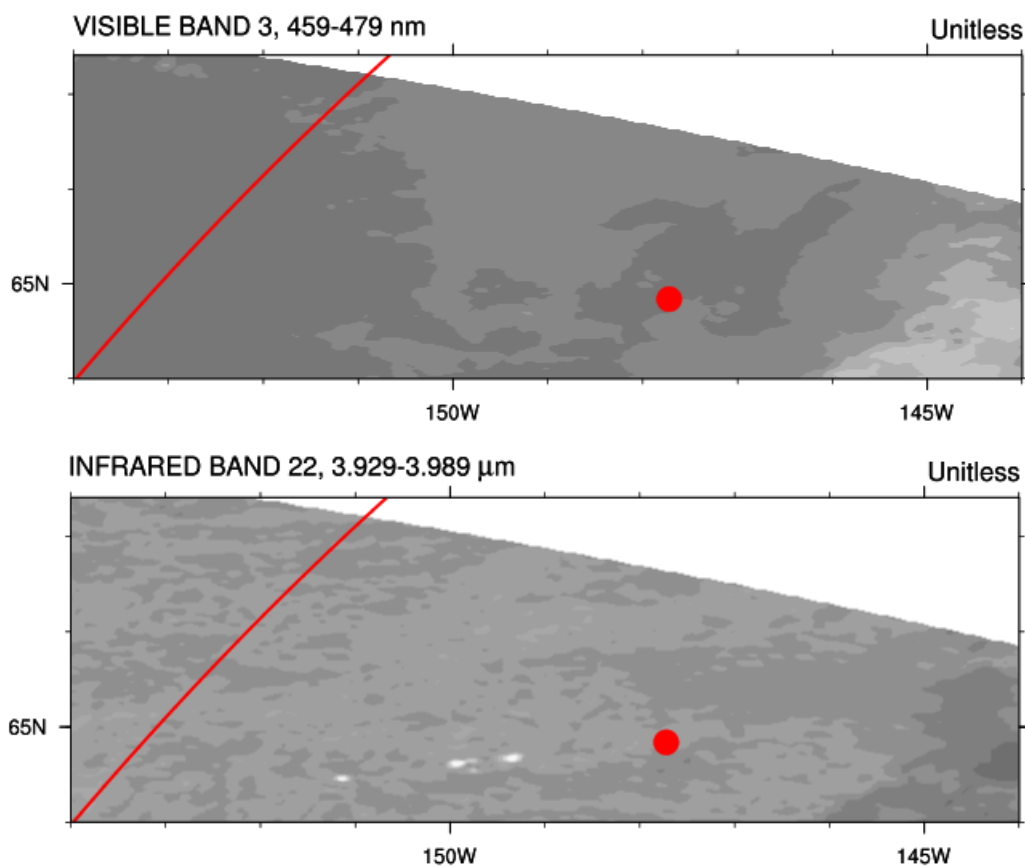


Fig. 3.11 MODIS Aqua visible and infrared images of wildfire smoke propagating through the approximate model domain, taken on 7 July, 1310 UTC. The red dot indicates the city of Fairbanks, Alaska. The red line indicates the CALIPSO scan. Note how the infrared captures the bright wildfire signatures at the surface to the west of Fairbanks. Additionally note the small temporal offset between the imagery and the model results shown in Figure 3.12.

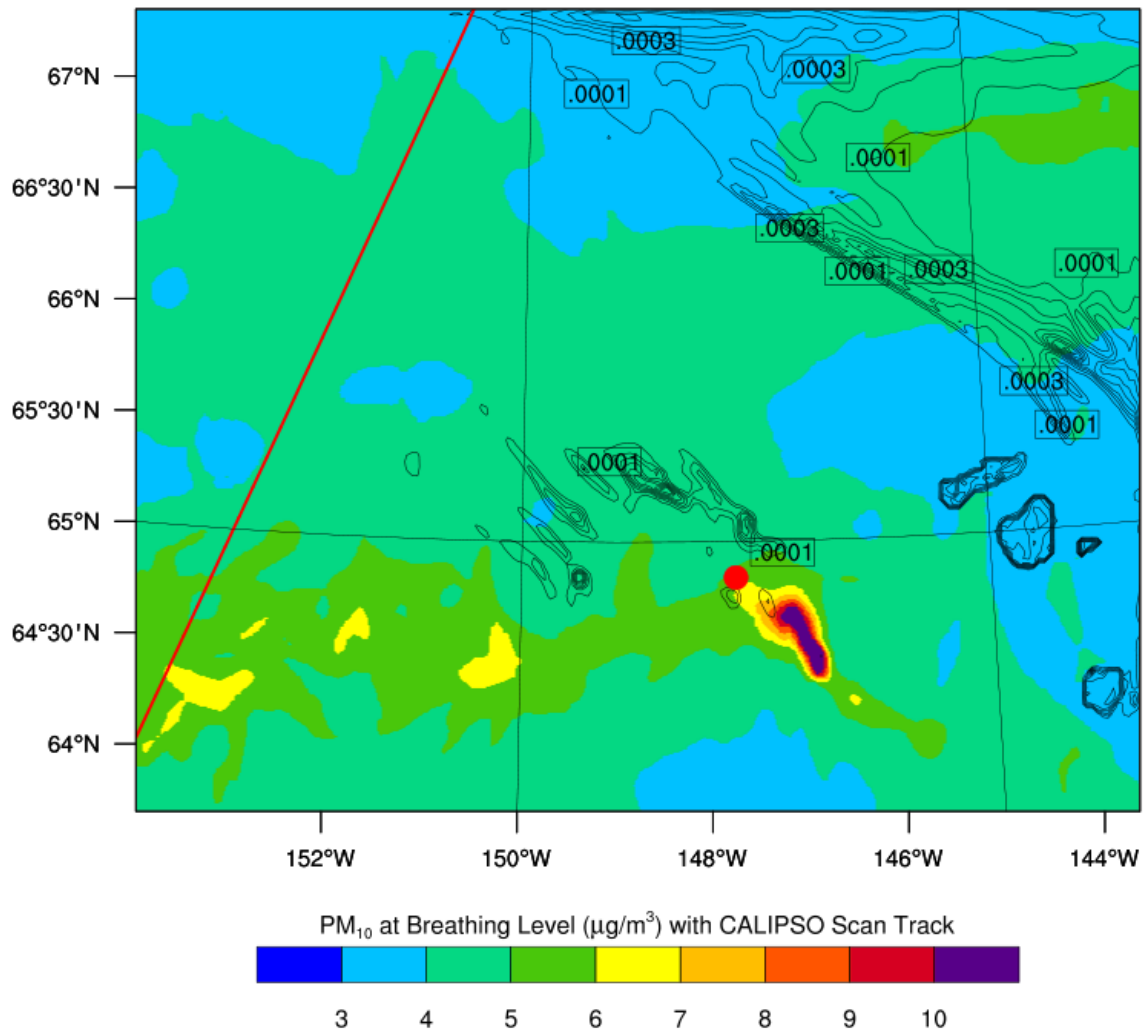


Fig. 3.12 WRF/Chem breathing level PM₁₀ concentrations at 7 July, 1300 UTC with the CALIPSO scan track in red. The red dot signifies the position of Fairbanks, Alaska. Dark contour lines within the model domain indicate the cloud particle mixing ratio (cloud-water + rain-water + snow + graupel + ice mixing ratios), as defined by a threshold value suggested by Beres et al. (2009).

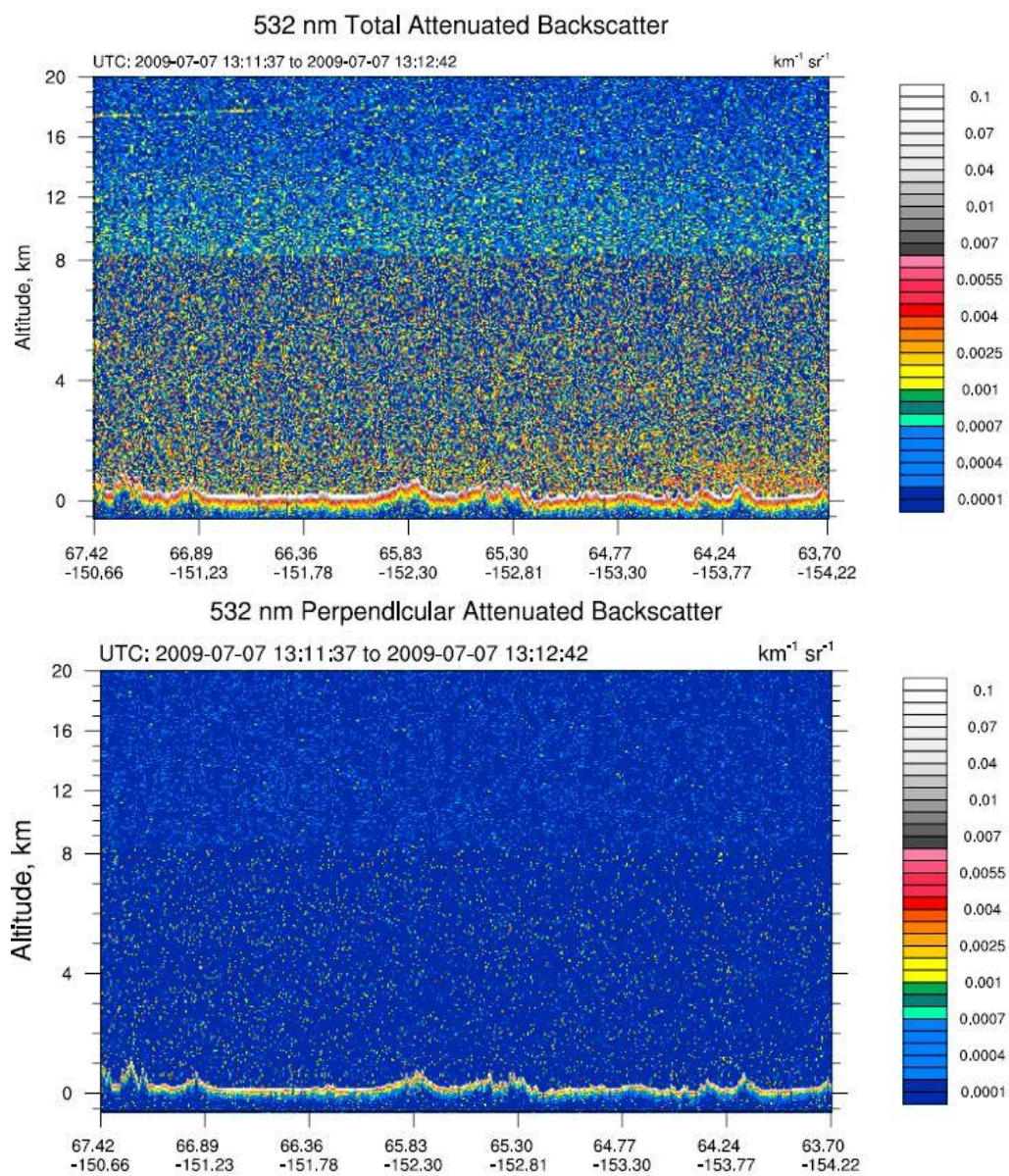


Fig. 3.13 The nighttime total attenuated backscatter (top) and perpendicular backscatter (bottom) at 532 nm from CALIPSO's CALIOP lidar for 7 July, 1311 to 1312 UTC.

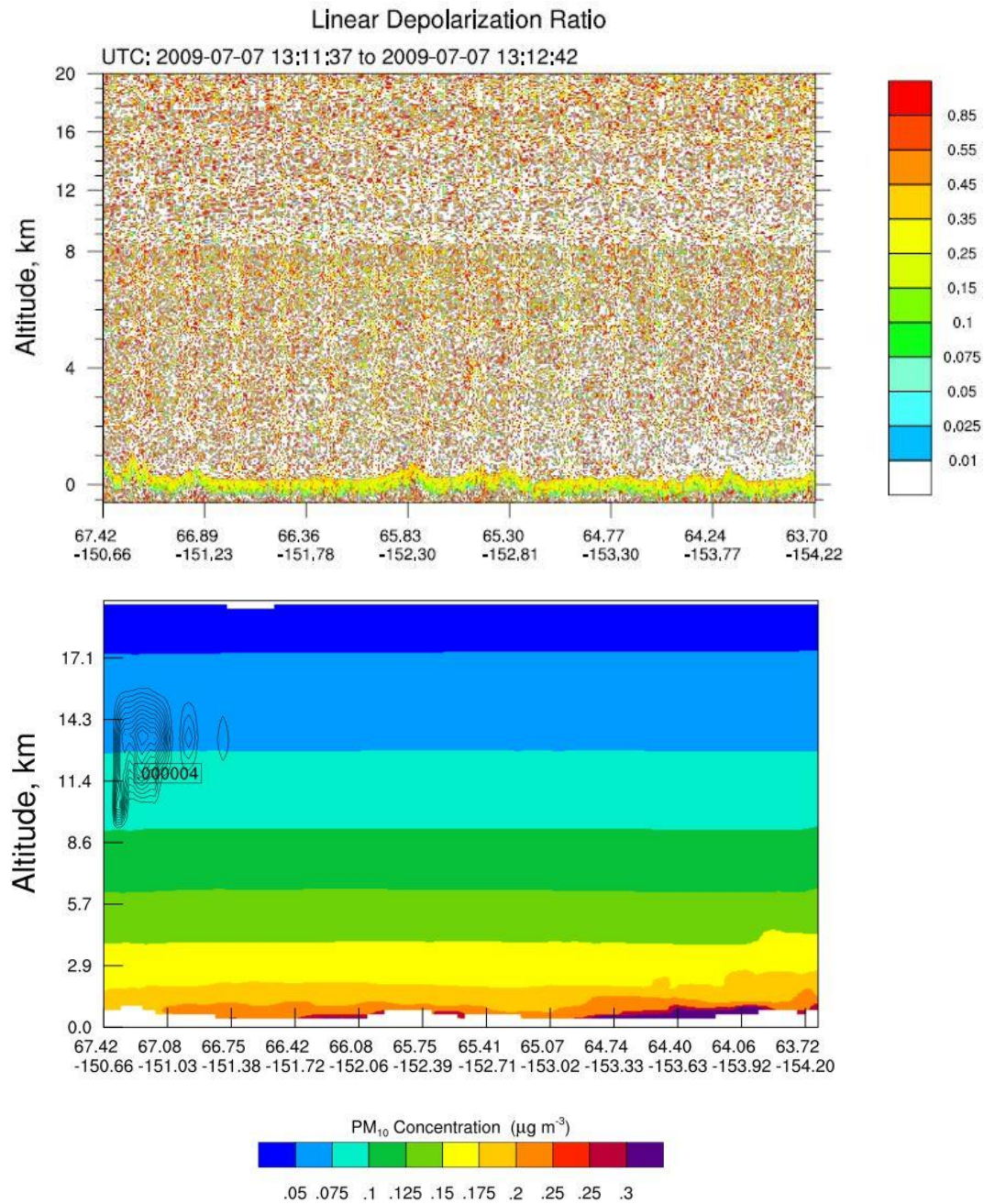


Fig. 3.14 The linear depolarization ratio derived from nighttime CALIOP backscatter data for 7 July, 1311 to 1312 UTC (top), and the WRF/Chem model cross-section of PM₁₀ concentration (in $\mu\text{g}/\text{m}^3$) at 7 July 1300 UTC (bottom). Dark contour lines within the model cross-section indicate the cloud particle mixing ratio (cloud-water + rain-water + snow + graupel + ice mixing ratios), as defined by a threshold value suggested by Beres et al. (2009).

The WRF/Chem simulation performs well in predicting the steady, zonal decrease of particulate matter with height (Fig. 3.14). Moreover, WRF/Chem predicts an increase of PM_{10} slightly north of the region where both light backscattering and very low depolarization occur. Temporal and spatial offsets within the model possibly caused slight discrepancies.

3.2.2 July 11 Case

The MODIS imagery and CALIPSO scan track for the 11 July case are featured in Figures 3.15 and 3.16. While smoke can be seen in the MODIS imagery, both METAR reports and National Weather Service discussions do not feature smoke because the smoke did not occur at Fairbanks. The total backscattering plot features light backscattering in an area uninhibited by cloud contamination, from 64.55 to 63.90 N latitude (Fig. 3.17). In the same locations, the perpendicular backscattering plot features extremely low perpendicular scattering (Fig. 3.17), and the linear depolarization ratio plot features very low to zero depolarization (Fig. 3.18).

WRF/Chem simulates high PM_{10} in the same regions (Fig. 3.18). WRF/Chem also simulates a tall plume, slightly north of where light backscattering and low depolarization values occur. Like the 7 July case, WRF/Chem simulates a zonal decrease of PM_{10} with height. Temporal and spatial offsets again seem to cause discrepancies between the WRF/Chem cross-section and the lidar curtain.

3.2.3 July 27 Case

The MODIS imagery and CALIPSO scan track for the 27 July case are featured in Figures 3.19 and 3.20. METAR reports and National Weather Service discussions indicate smoke presence at Fairbanks. The total backscattering plot indicates light backscattering below 2 km from 66.70 to 65.55 N latitude (Fig. 3.21). In the same region, little perpendicular backscattering occurs. Additionally, there are very low to zero depolarization values in the same region (Fig. 3.22).

The WRF/Chem model data at 1300 UTC indicates notable amounts of particulate matter below an altitude of roughly 3.3 km (Fig. 3.22). The model also seems to simulate suspended particulate matter north of the high terrain (around 65.96 N latitude), which would be consistent with what the backscattering and depolarization plots indicate. Model discrepancies can be explained through those that were mentioned in previous cases, as well as through the impact of model terrain on the propagation of aerosols.

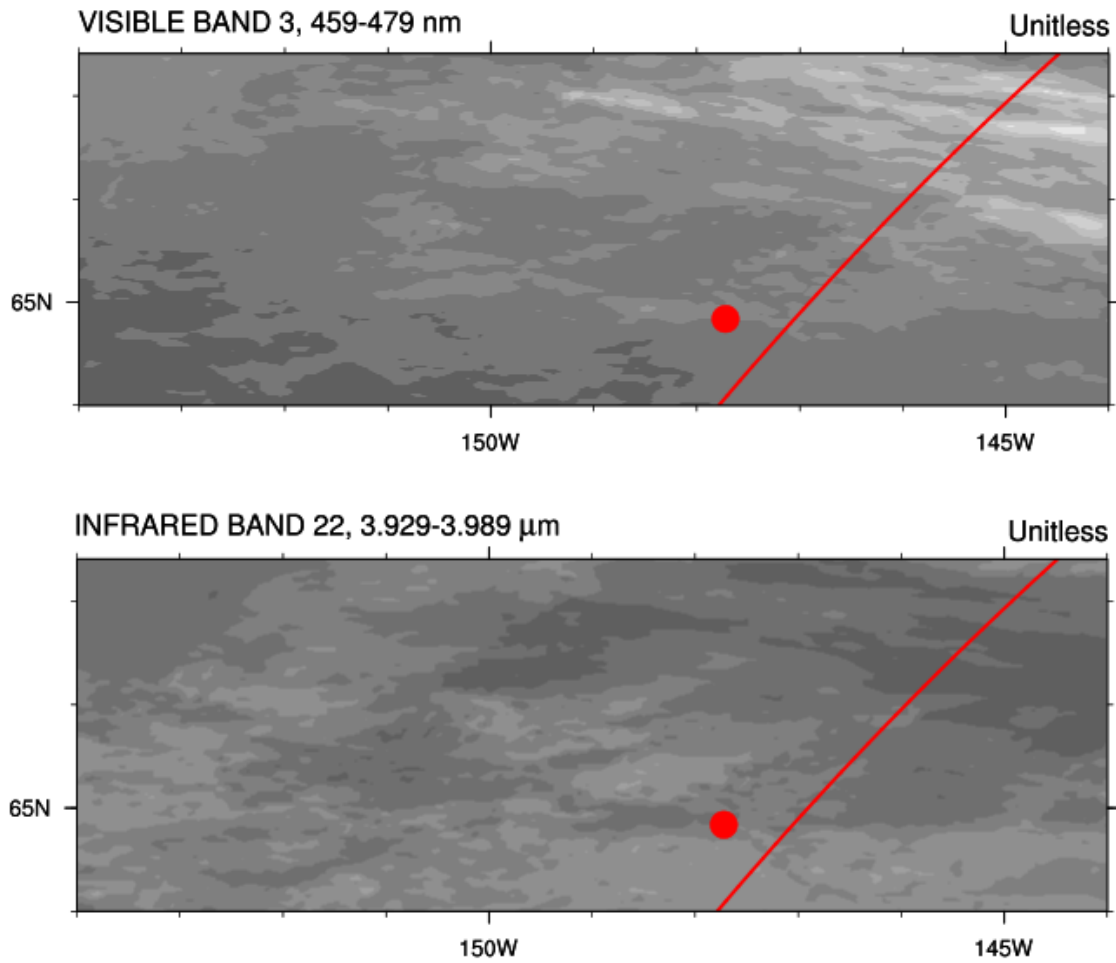


Fig. 3.15 MODIS Aqua visible and infrared images of wildfire smoke and clouds propagating through the approximate model domain, taken on 11 July, 1245 UTC. The red dot indicates the city of Fairbanks, Alaska. The red line indicates the CALIPSO scan. While the visible imagery shows cloud presence to the north and northeast, the infrared imagery captures small amounts of smoke throughout the southern portion of the domain. Note the small temporal offset between the imagery and model results shown in Figure 3.16.

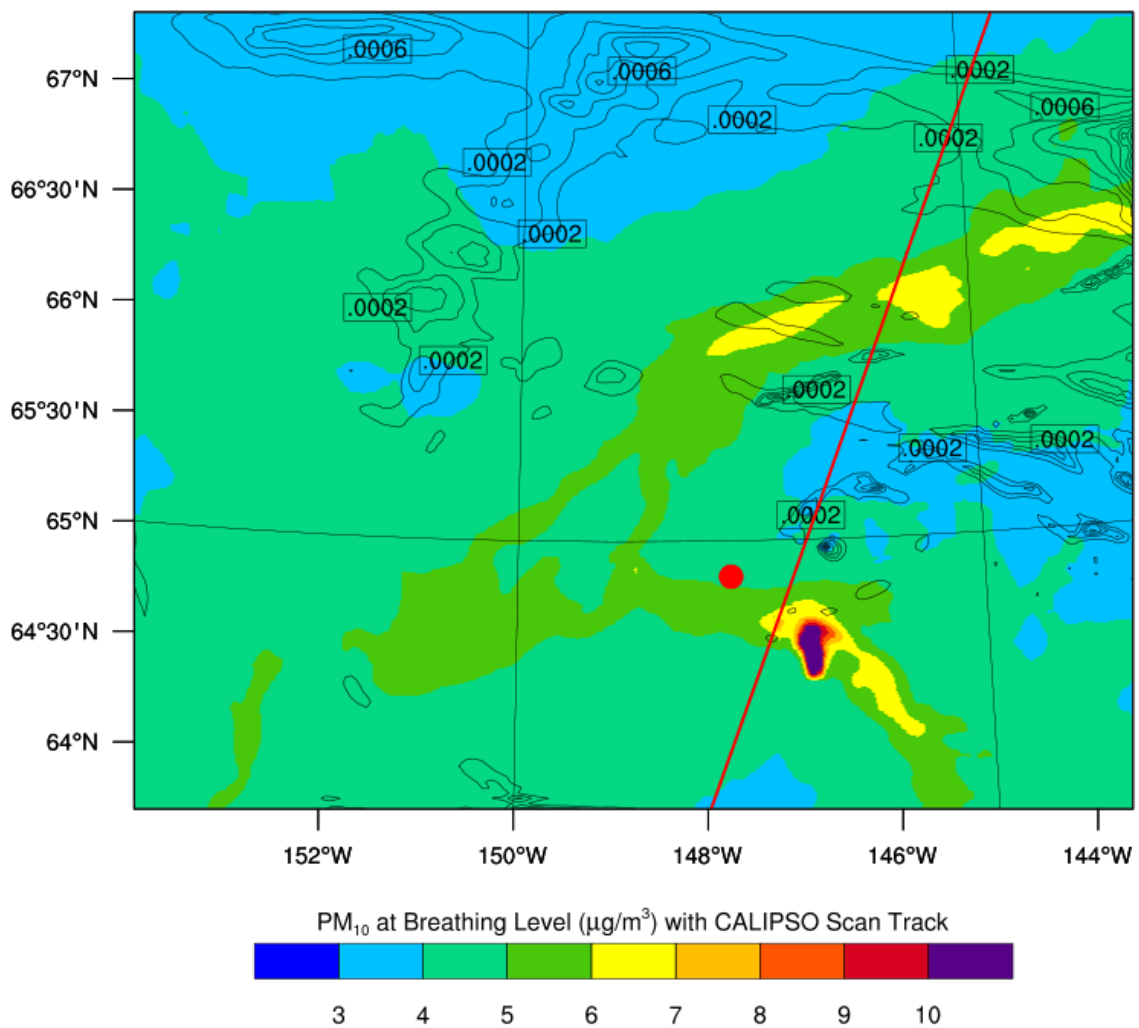


Fig. 3.16 WRF/Chem breathing level PM₁₀ concentrations at 11 July, 1300 UTC with the CALIPSO scan track in red. The red dot signifies the position of Fairbanks, Alaska. Dark contour lines within the model domain indicate the cloud particle mixing ratio (cloud-water + rain-water + snow + graupel + ice mixing ratios), as defined by a threshold value suggested by Beres et al. (2009).

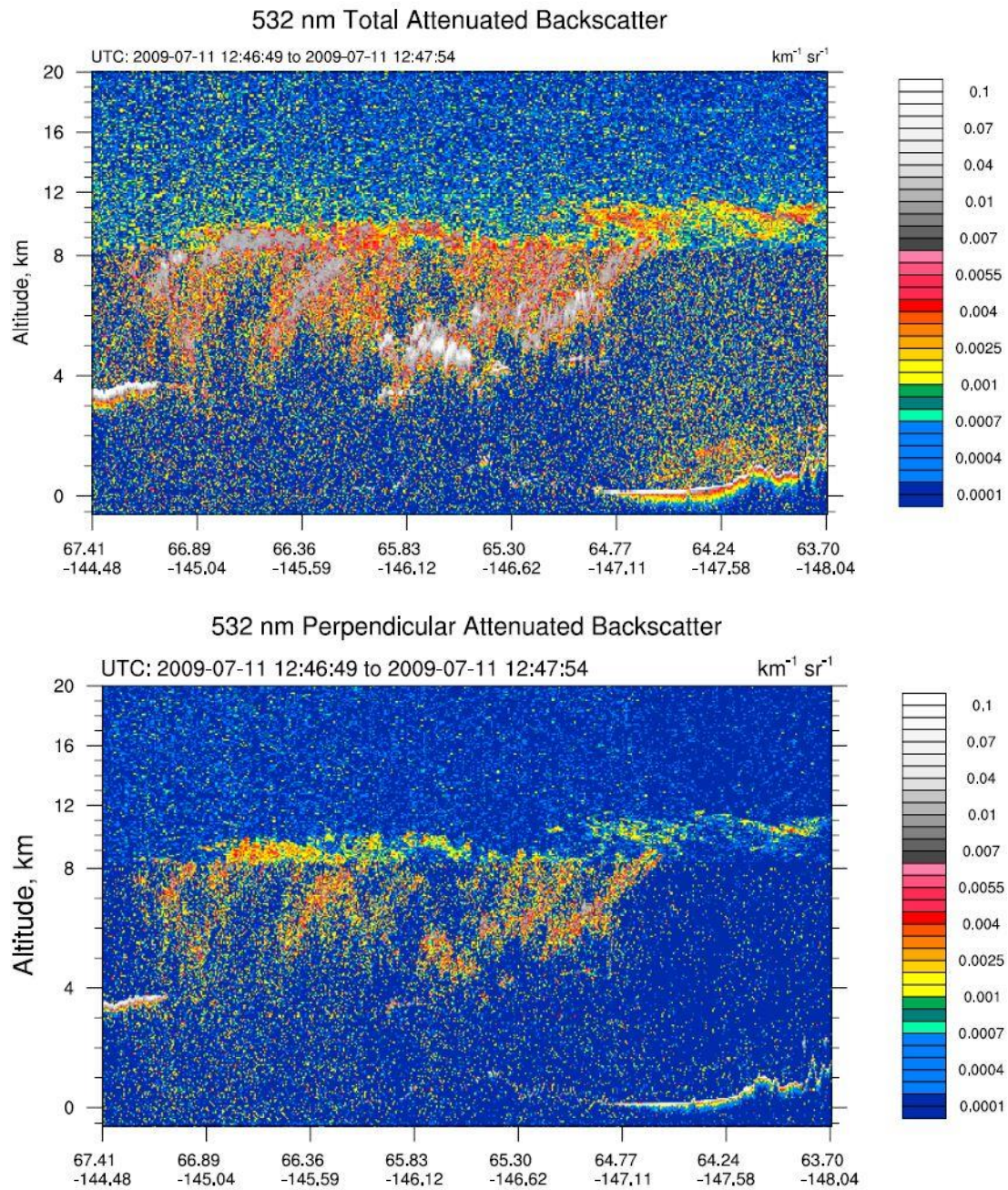


Fig. 3.17 The nighttime total attenuated backscatter (top) and perpendicular backscatter (bottom) at 532 nm from CALIPSO's CALIOP lidar for 11 July, 1246 to 1247 UTC.

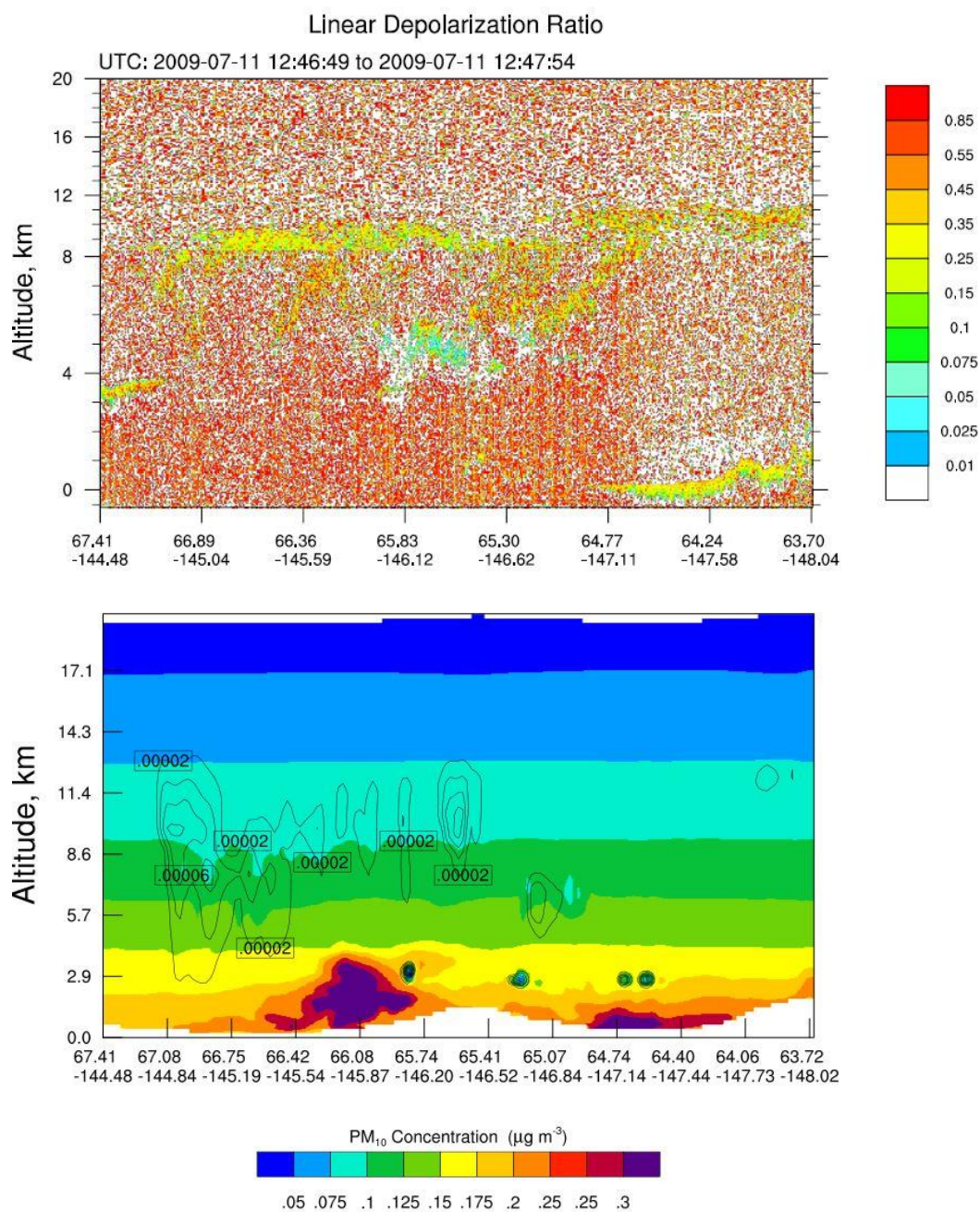


Fig. 3.18 The linear depolarization ratio derived from nighttime CALIOP backscatter data for 11 July, 1246 to 1247 UTC (top), and the WRF/Chem model cross-section of PM₁₀ concentration (in $\mu\text{g}/\text{m}^3$) at 11 July 1300 UTC (bottom). Dark contour lines within the model cross-section indicate the cloud particle mixing ratio (cloud-water + rain-water + snow + graupel + ice mixing ratios), as defined by a threshold value suggested by Beres et al. (2009).

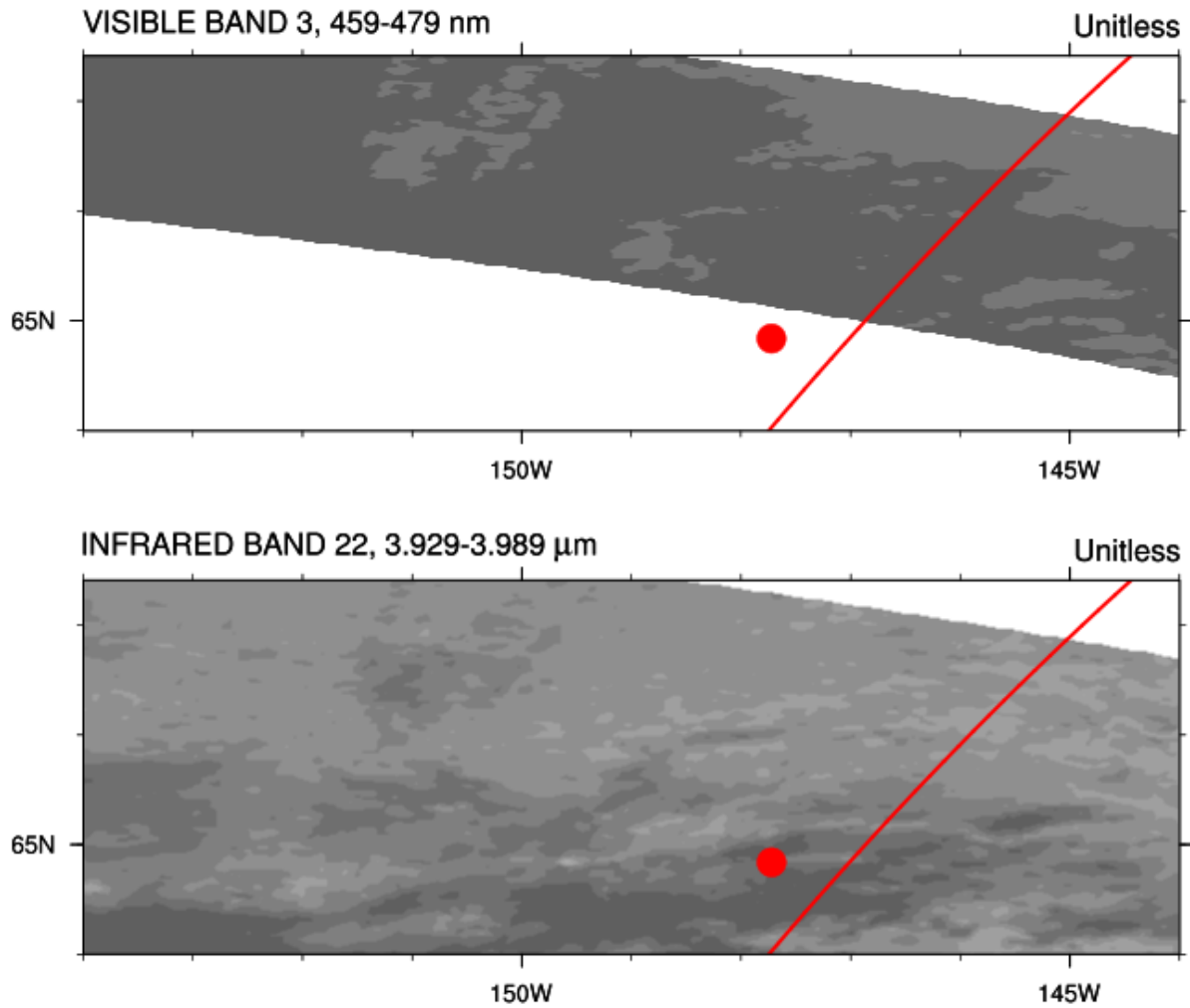


Fig. 3.19 MODIS Aqua visible and infrared images of wildfire smoke and clouds propagating through the approximate model domain, taken on 27 July, 1245 UTC. The red dot indicates the city of Fairbanks, Alaska. The red line indicates the CALIPSO scan. The infrared image captures smoke propagation and low clouds throughout the central and northern portions of the domain. Note the small temporal offset between the imagery and the model results shown in Figure 3.20.

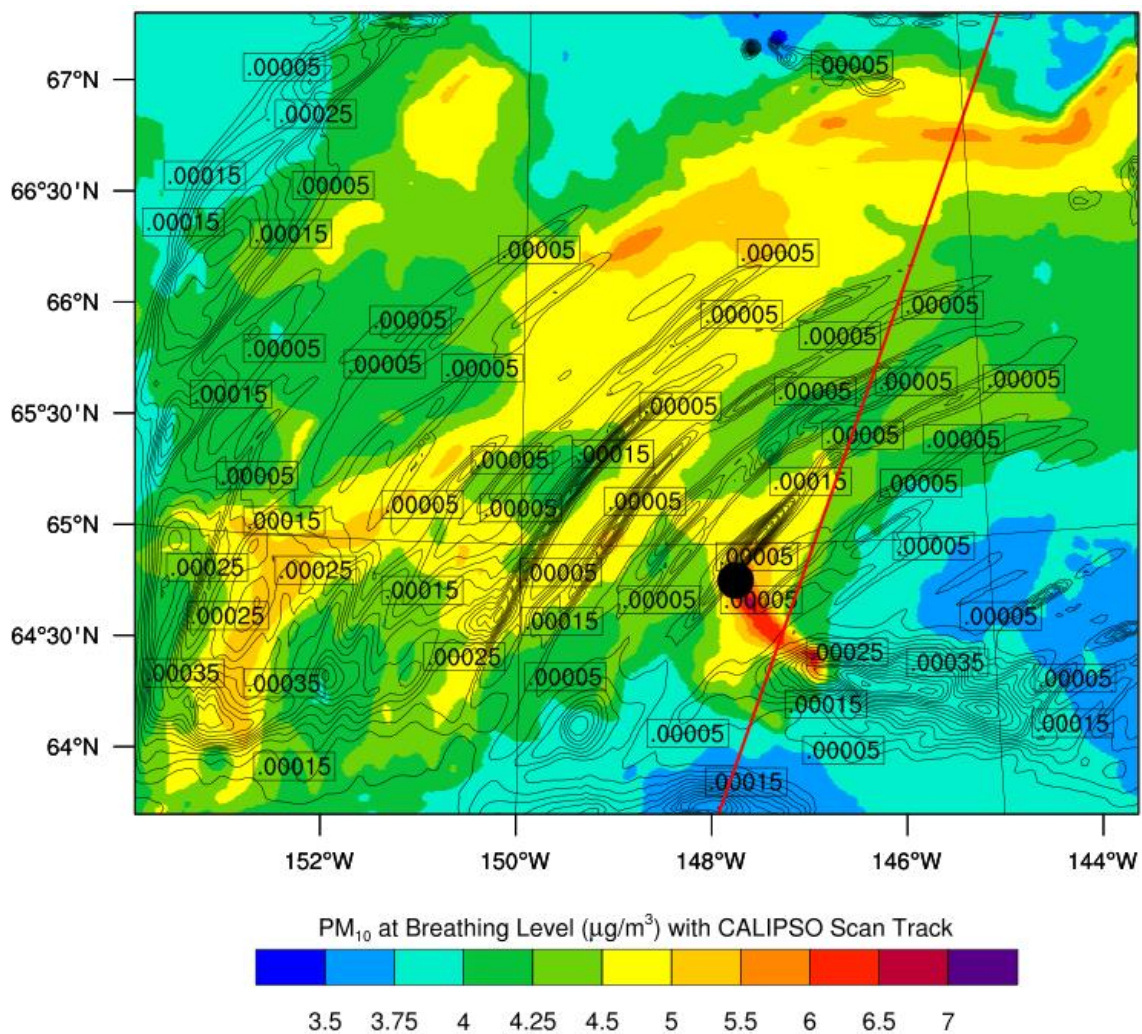


Fig. 3.20 WRF/Chem breathing level PM_{10} concentrations at 27 July, 1300 UTC with the CALIPSO scan track in red (bottom). The black dot signifies the position of Fairbanks, Alaska. Dark contour lines within the model domain indicate the cloud particle mixing ratio (cloud-water + rain-water + snow + graupel + ice mixing ratios), as defined by a threshold value suggested by Beres et al. (2009).

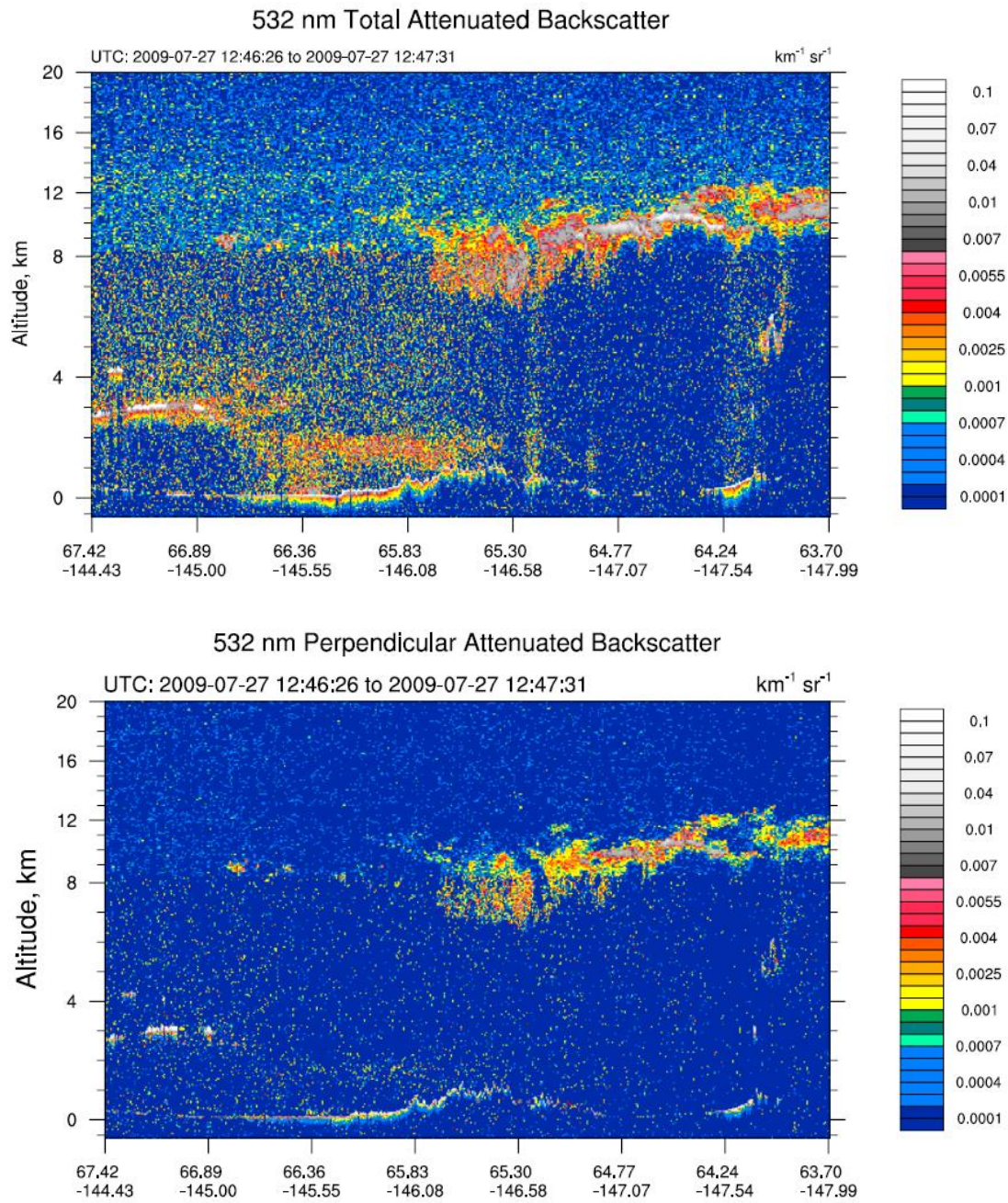


Fig. 3.21 The nighttime total attenuated backscatter (top) and perpendicular backscatter (bottom) at 532 nm from the CALIPSO's CALIOP lidar for 27 July, 1246 to 1247 UTC.

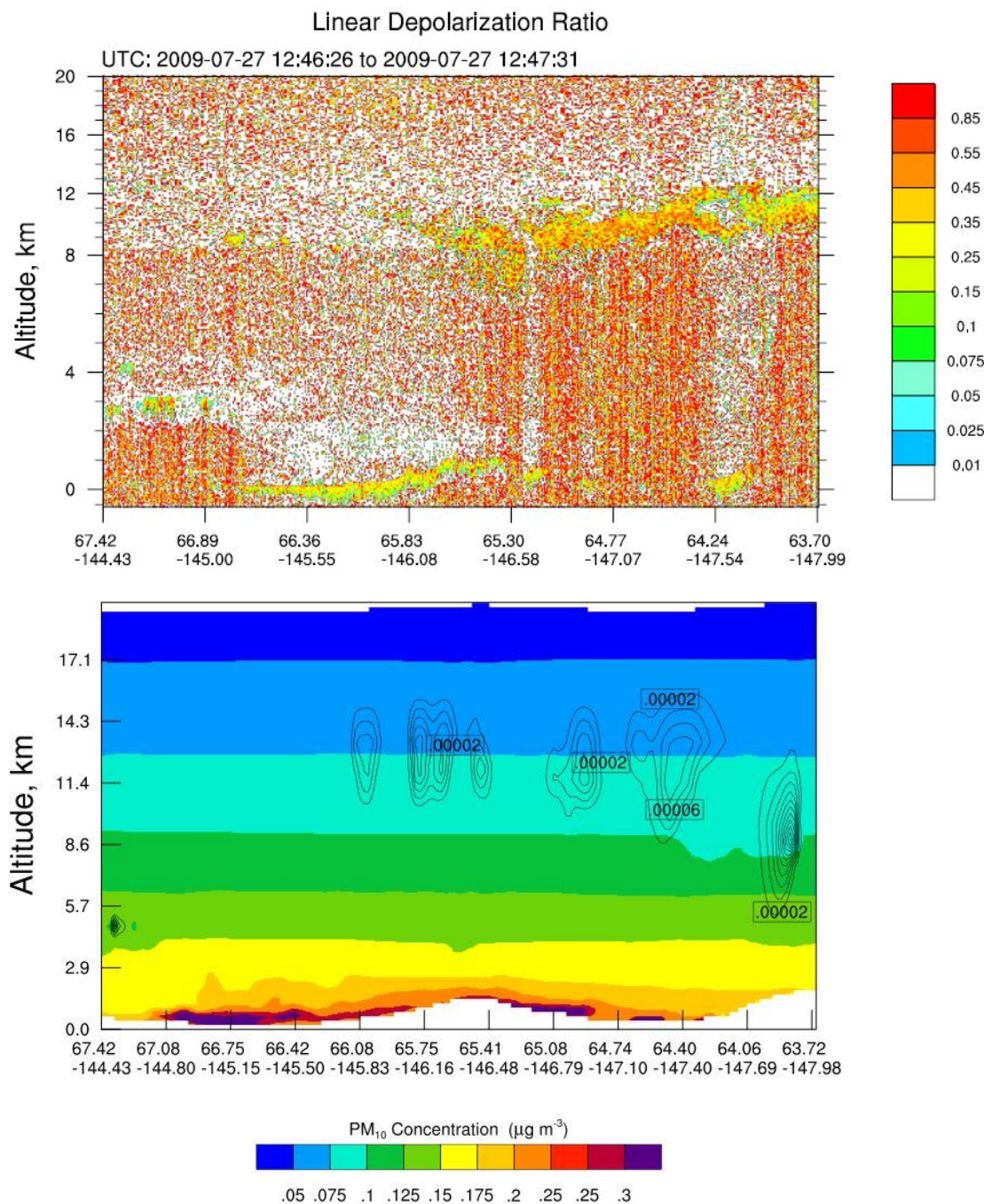


Fig. 3.22 The linear depolarization ratio derived from nighttime CALIOP backscatter data for 27 July, 1246 to 1247 UTC (top), and the WRF/Chem model cross-section of PM₁₀ concentration (in $\mu\text{g}/\text{m}^3$) at 27 July 1300 UTC (bottom). Dark contour lines within the model cross-section indicate the cloud particle mixing ratio (cloud-water + rain-water + snow + graupel + ice mixing ratios), as defined by a threshold value suggested by Beres et al. (2009).

3.2.4 Conclusions on the Vertical Aerosol Performance

Overall, CALIPSO backscatter and depolarization has provided an acceptable, qualitative means of evaluating vertical WRF/Chem simulations of PM_{10} . The model's performance in predicting aerosol vertical distribution along the lidar curtain is very similar to CALIPSO backscatter and depolarization remote sensing data, albeit small spatial and temporal differences.

However, simulated aerosol concentrations seem to be relatively small. There are multiple reasons for error. First, model parameterizations of sub-grid scale emission processes are not perfect and will induce error. Equation 2.2 (see section 2.1.3) showed that the amount of emitted wildfire tracers is dependent upon above-ground biomass availability, flammable vegetation, and the area of the land (Grell et al. 2011). In regard to the area of the land, wildfire location data is not perfect; the location data may miss an area with fires, thus reducing the amount of area available for simulated burning. Moreover, grid-cell averaging establishes a singular land-use type across a 4 km^2 grid-cell; thus, land-use type generalizations and miscategorizations will induce vegetation errors (and hence combustion errors) within Equation 2.2. Lastly, surface roughness within the model is not as refined as what is seen in reality, and will miss the complexity of the surface vegetation heights. Above-ground biomass is important in calculating emitted wildfire tracers, and simplistic estimations of the amount of above-ground biomass will create errors.

Chapter 4 Synthetic Pixels

After the statistical and qualitative evaluations of WRF/Chem performance, the WRF/Chem output will be used as input for the synthetic pixel program. The program will demonstrate how pixels of 1 km nadir aerosol-sensitive radiometers (onboard geostationary satellites) would resemble in an environment affected by wildfires.

Before analyzing test cases of clean and polluted pixels, an example case will be demonstrated to see how raw WRF/Chem data can be used to generate a grid of synthetic pixels. Following, a test case will demonstrate what clean synthetic pixels look like. Then, polluted pixels, which will indicate the presence of a simulated smoke plume, will be showcased. Both test cases will feature their respective raw WRF/Chem data plots.

To determine the vertical extent of the plume, the domains of both test cases will be examined through model cross-sections. Also, the cross-sections will help determine qualitatively the accuracy of the pixels' vertical integration and spatial positioning. Lastly, the pixels and their content would be examined for possible errors, and suggestions for future projects will be mentioned.

4.1 Synthetic Pixel Construction

A sample WRF/Chem plot will illustrate how the synthetic pixels are developed. WRF/Chem data is plotted normally (Fig. 4.1), and a looping structure is used within the program to create a grid of synthetic pixels over the same plot (Fig. 4.2). Each 'oval' constitutes a synthetic pixel, and is appropriately sized to represent the distortion of pixel geometry that occurs in the high latitudes (see Chapter 2).

Statements within the looping structure serve various functions. For example, missing values are assigned to data that are outside of the pixels; this is done to distinguish one pixel from another and to remove the effects from overlapping. Reiterating, there is a clause in the looping structure that vertically integrates the WRF/Chem PM_{10} data over multiple WRF/Chem layers.

In order to represent a signature that a pixel would ideally provide, the vertically-integrated WRF/Chem simulated PM_{10} values within each pixel are averaged (Fig. 4.3). A color scheme is applied to visually assess the vertically integrated PM_{10} values. To illustrate areas of high PM_{10} presence, the $1,800 \mu\text{g}/\text{m}^2$ threshold (see Section 2.3) is applied as the highest boundary in the color scheme.

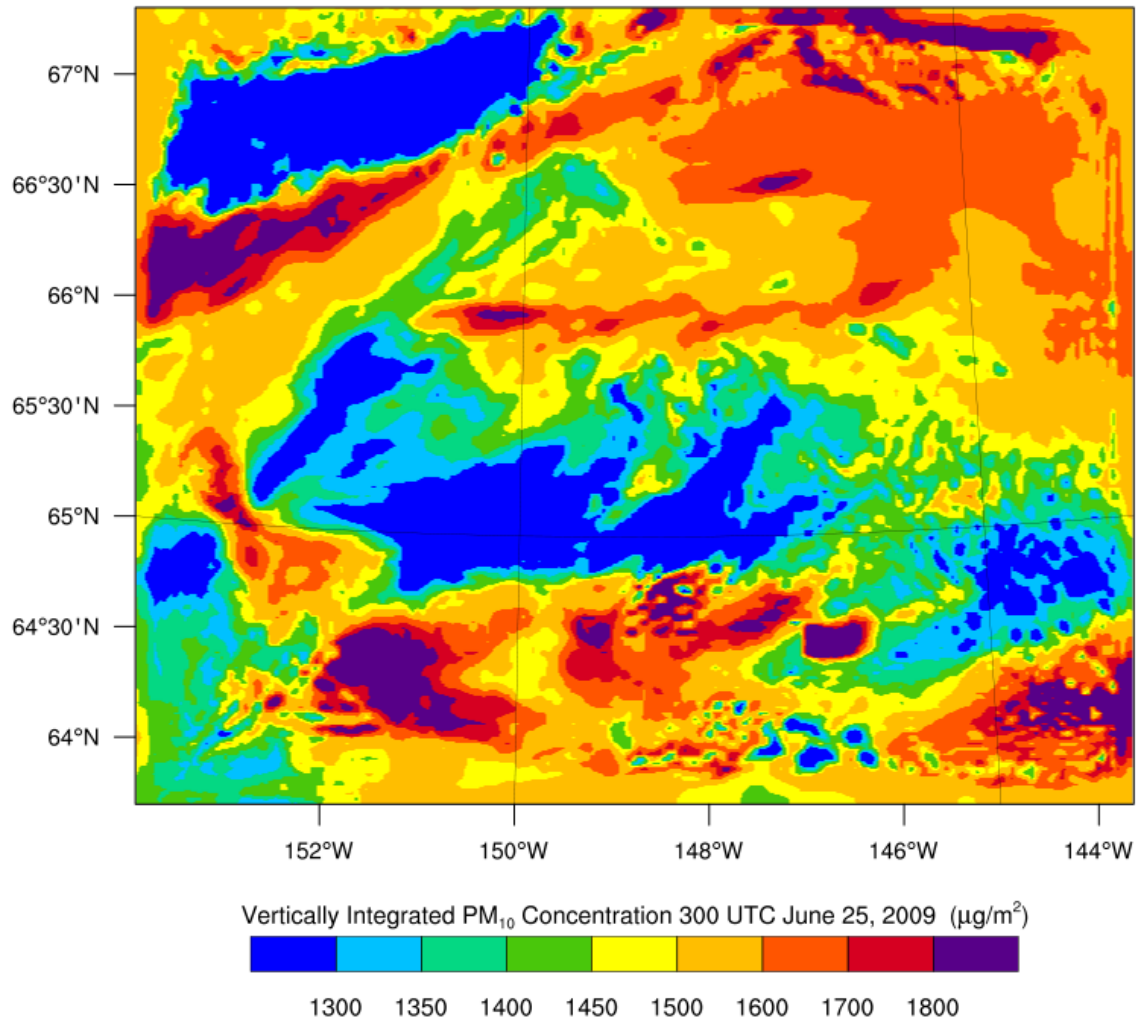


Fig. 4.1 A normal plot of vertically-integrated WRF/Chem PM₁₀ data over the domain for June 25, 2009, 300 UTC.

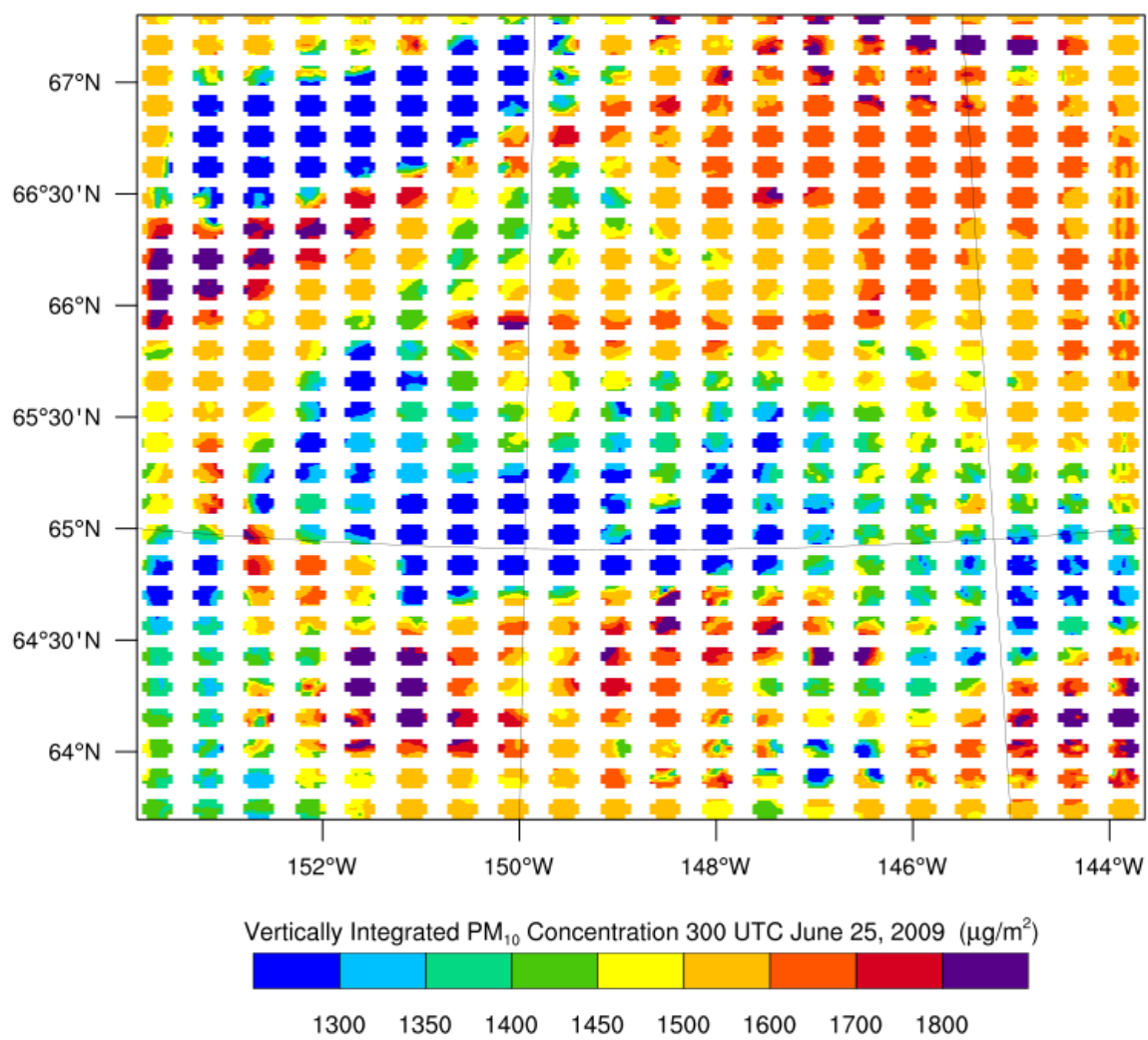


Fig. 4.2 A grid of synthetic pixels overlay the WRF/Chem data over the same domain (see Fig. 4.1).

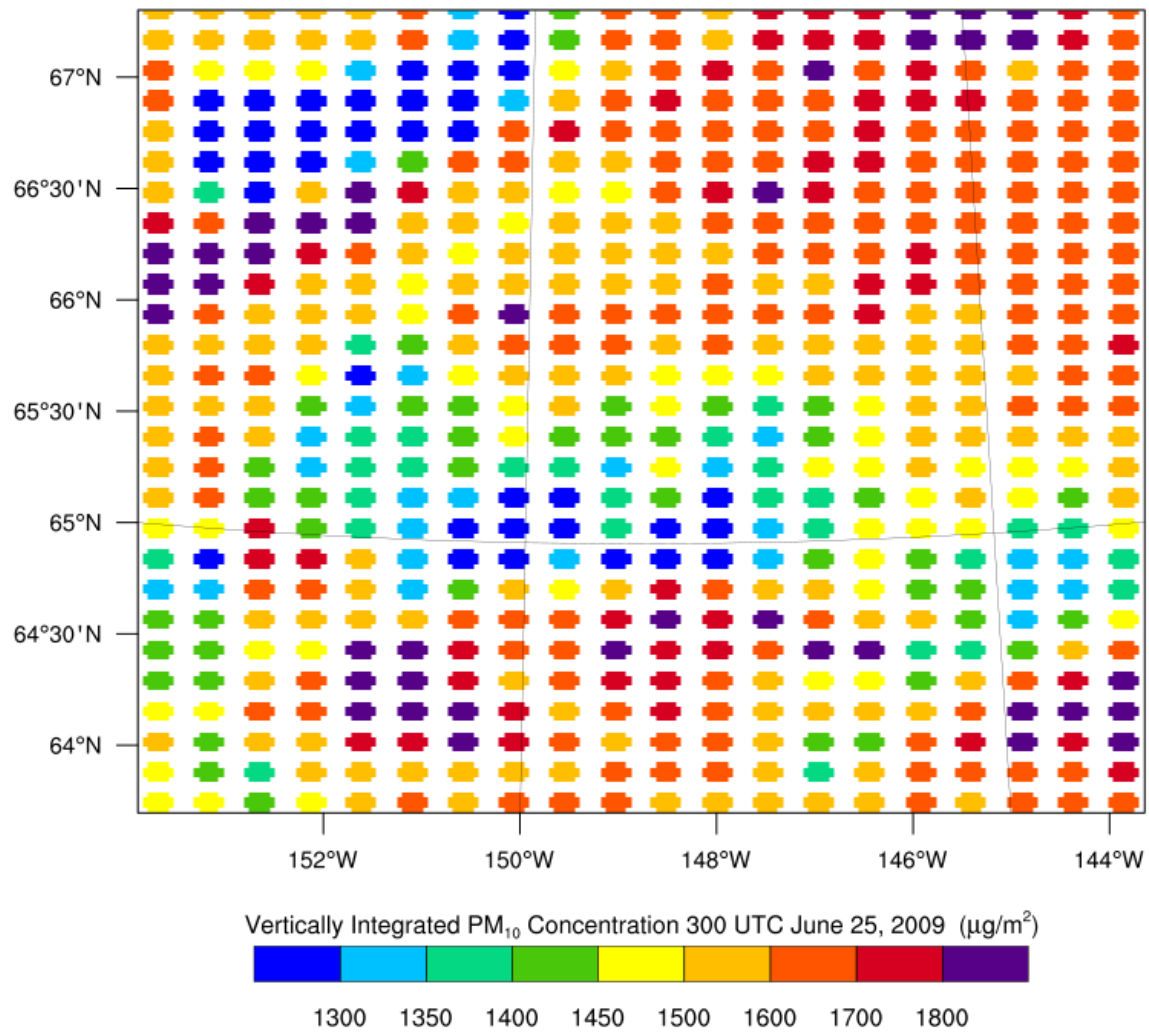


Fig. 4.3 Synthetic pixels from the previous figure are averaged.

4.2 Clean Synthetic Pixels

A test case is undertaken to visually assess a clean environment. A raw WRF/Chem plot shows an optically-thin environment in the south-central and southeastern portion of the domain with low amounts of simulated accumulated smoke, where values are below the $1,800 \mu\text{g}/\text{m}^2$ threshold (Fig. 4.4).

The NCL program then uses the raw WRF/Chem data to produce a grid of synthetic pixels (Fig. 4.5). The WRF/Chem values within these pixels are then averaged to produce signatures in the final plot (Fig. 4.6). Light green, primary blue, and light blue synthetic pixels represent areas of low PM_{10} concentrations ($< 1400 \mu\text{g}/\text{m}^2$). Lower amounts of PM_{10} ($1400 - 1800 \mu\text{g}/\text{m}^2$), situated over the southwest and northeast parts of the domain, reflect lighter amounts of smoke from small fires.

Figure 4.7 illustrates the model cross-section through a relatively clean portion of the domain of interest. The cross-section indicates low simulated PM_{10} concentrations. As was demonstrated by the clean synthetic pixels, an area without wildfires should be visible at the edge of a geostationary satellite's field of view.

4.3 Polluted Synthetic Pixels

Next, a test case is undertaken to visually assess an environment with high smoke presence. A raw WRF/Chem plot shows an optically-thick environment with high amounts of simulated accumulated smoke in the domain, where some values are above the $1,800 \mu\text{g}/\text{m}^2$ threshold (Fig. 4.8).

The NCL program then uses the raw WRF/Chem data to produce a grid of synthetic pixels (Fig. 4.9). The WRF/Chem values within these pixels are then averaged to produce a final graphic (Fig. 4.10). In the southwest and northwest parts of the domain, WRF/Chem simulated a high smoke presence ($> 1,800 \mu\text{g}/\text{m}^2$). As illustrated by the multiple purple pixels, the $1,800 \mu\text{g}/\text{m}^2$ threshold was exceeded.

Note that there is a distance between the natural and anthropogenic sources of PM_{10} , between the wildfires at the southwestern part of the domain, and the Fairbanks metropolitan region to the east, respectively (Fig. 4.10). The lone orange synthetic pixel at $64^{\circ}30'N$, $147^{\circ}W$ reflects the combination of simulated anthropogenic PM_{10} contributions from the Fairbanks metropolitan region and the PM_{10} contributions from the propagating smoke to the west. Regardless, wildfire particulate matter values to the west exceed anthropogenic values.

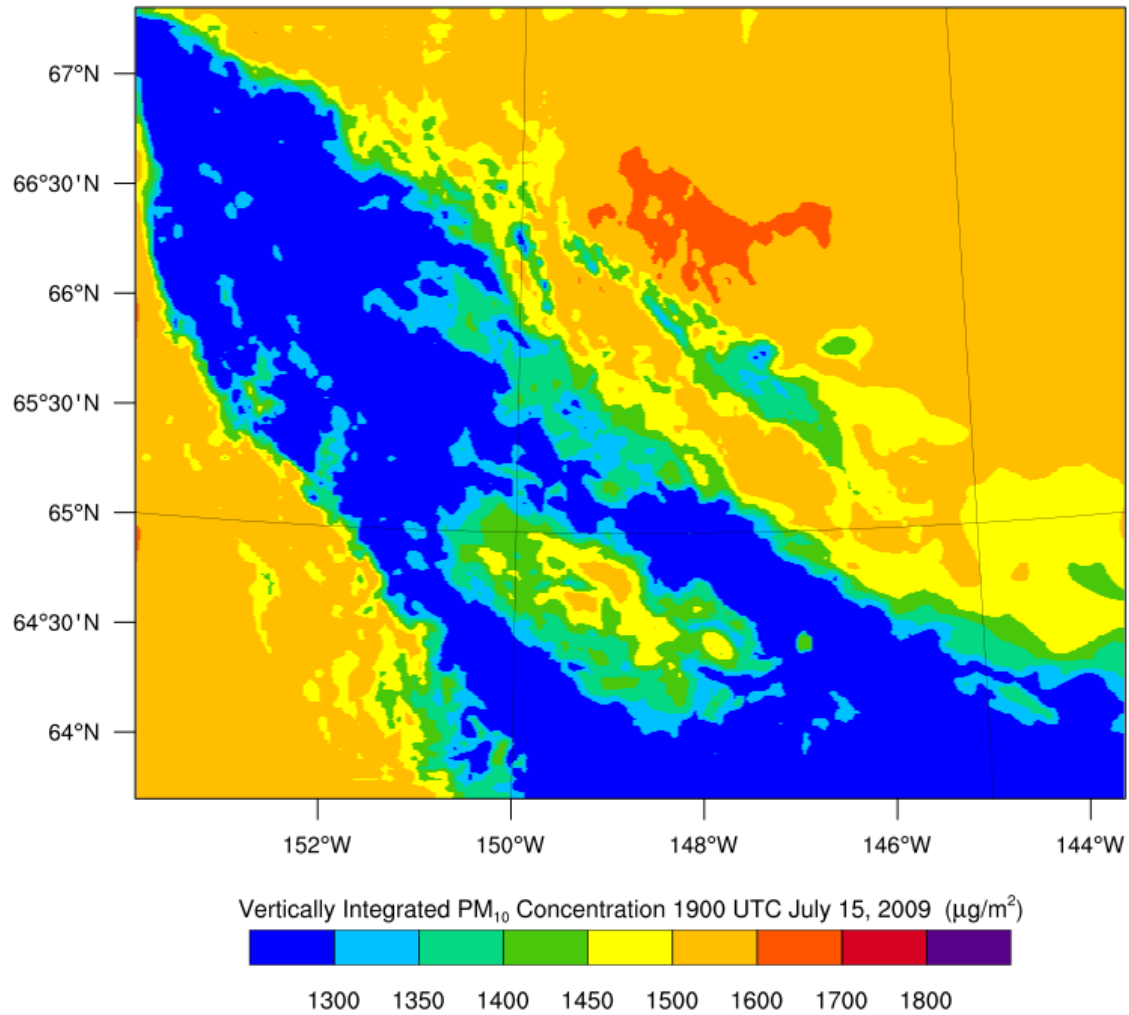


Fig. 4.4 A raw WRF/Chem plot for 1900 UTC, July 15, 2009, illustrating an optically-thin environment with low amounts of simulated accumulated smoke.

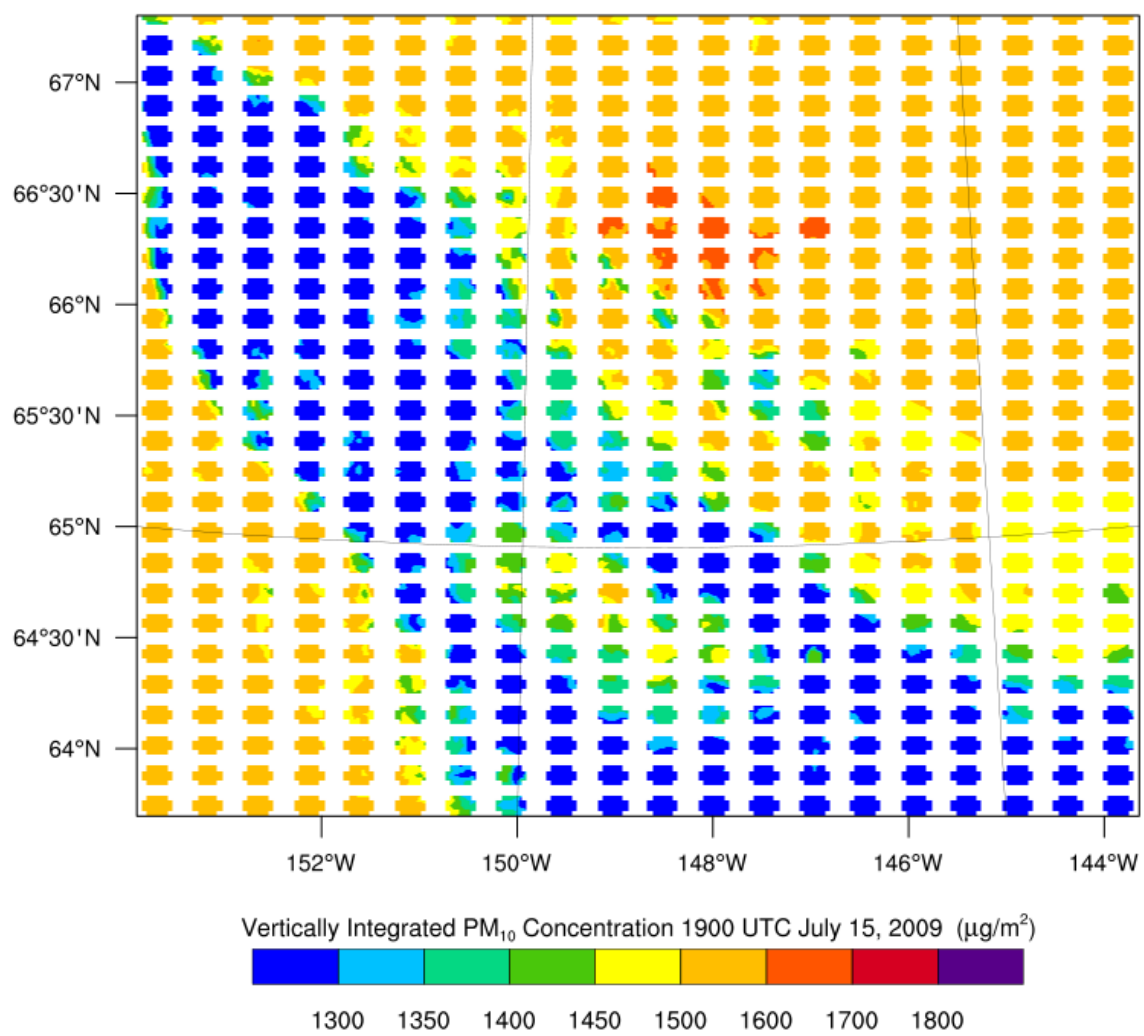


Fig. 4.5 A grid of synthetic pixels overlay the previous plot.

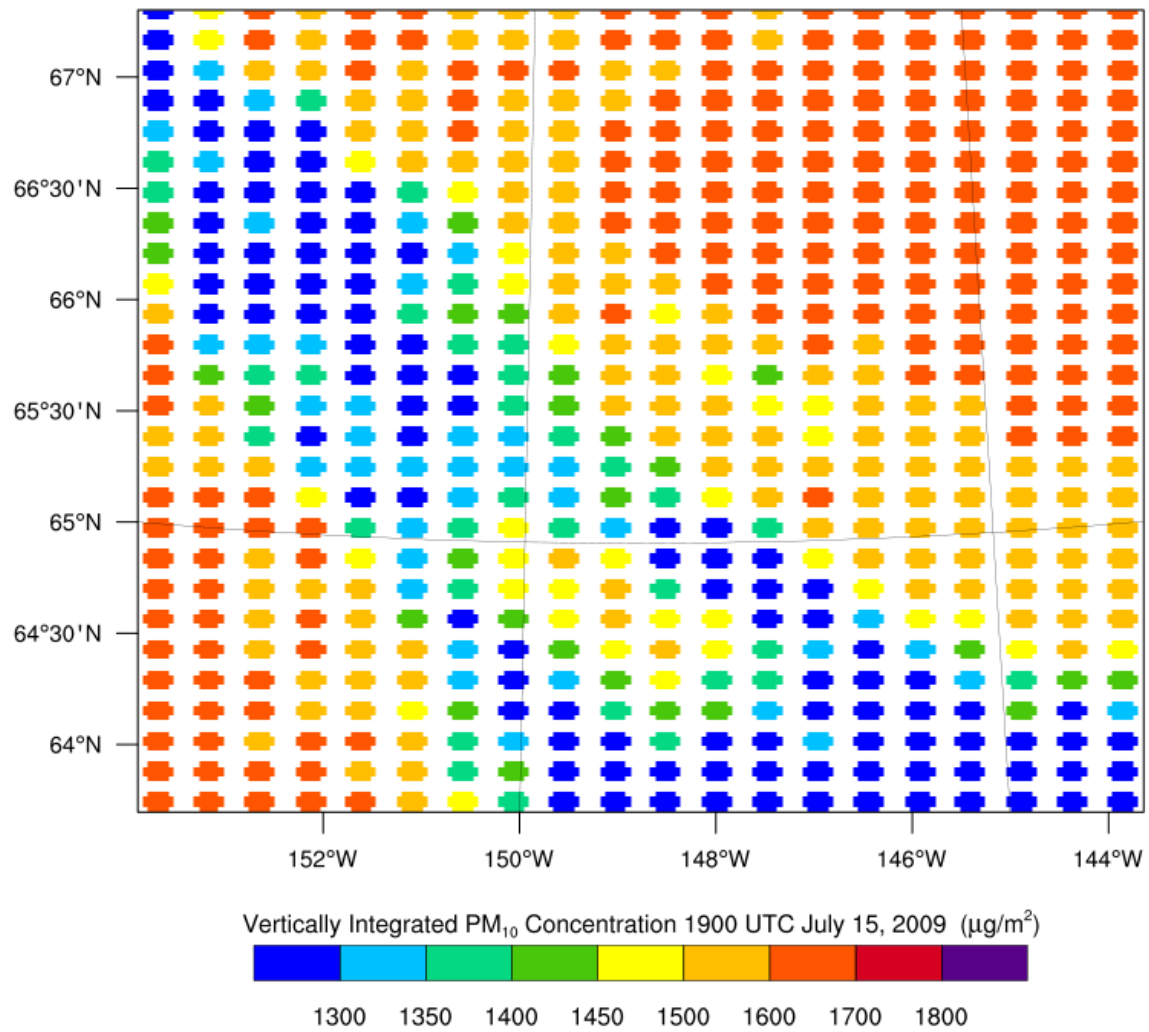


Fig. 4.6 Synthetic pixels from the previous figure are averaged to produce a clean-environment test case.

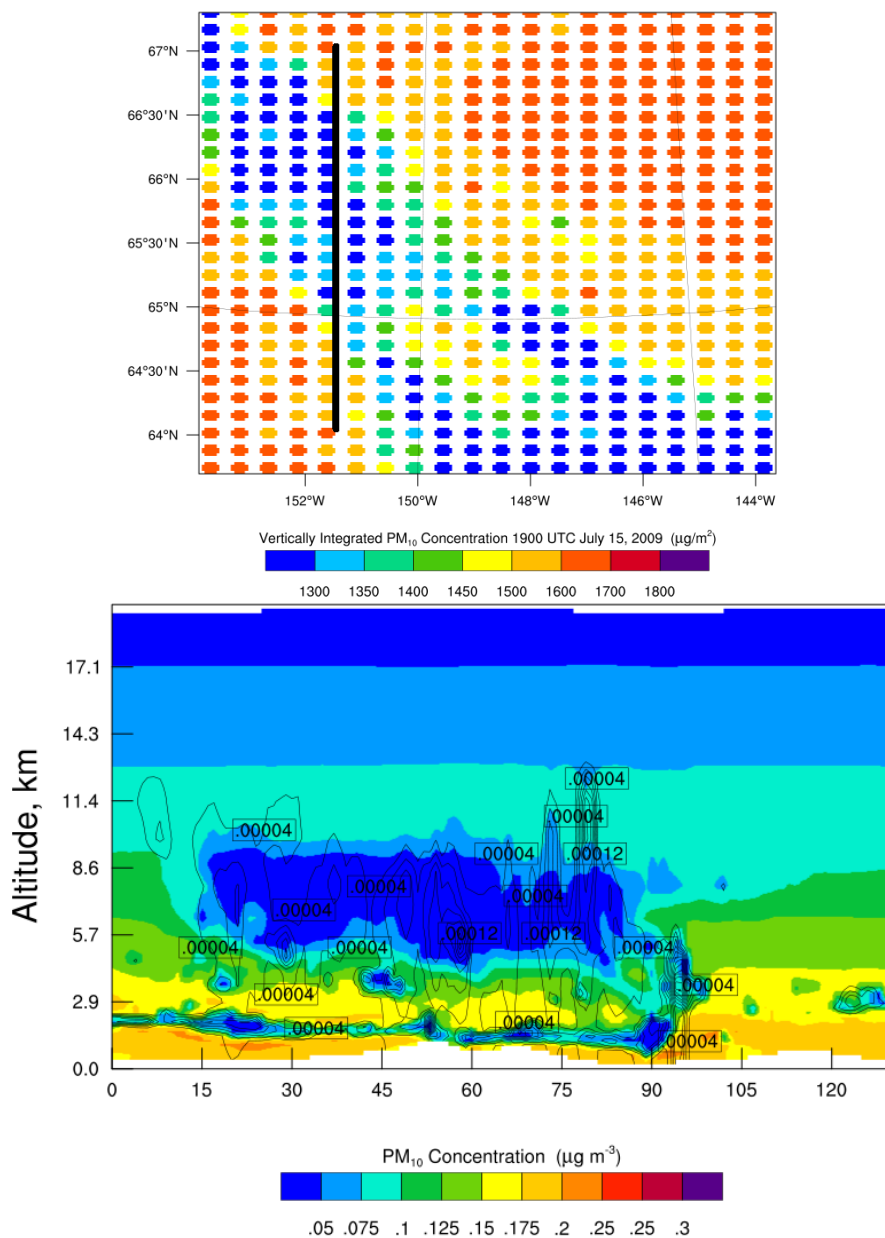


Fig. 4.7 A cross-section through part of the clean-environment case, 15 July, 2009, 1900 UTC. The red line in the model domain (top) illustrates the position of the model cross-section. In the model cross-section (bottom), the north is to the left of the plot, and the south is to the right of the plot. A relatively clean environment is depicted by the synthetic pixels and the model cross-section. Black contours indicate the cloud particle mixing ratio (cloud-water + rain-water + snow + graupel + ice mixing ratios), as defined by a threshold value suggested by Beres et al. (2009).

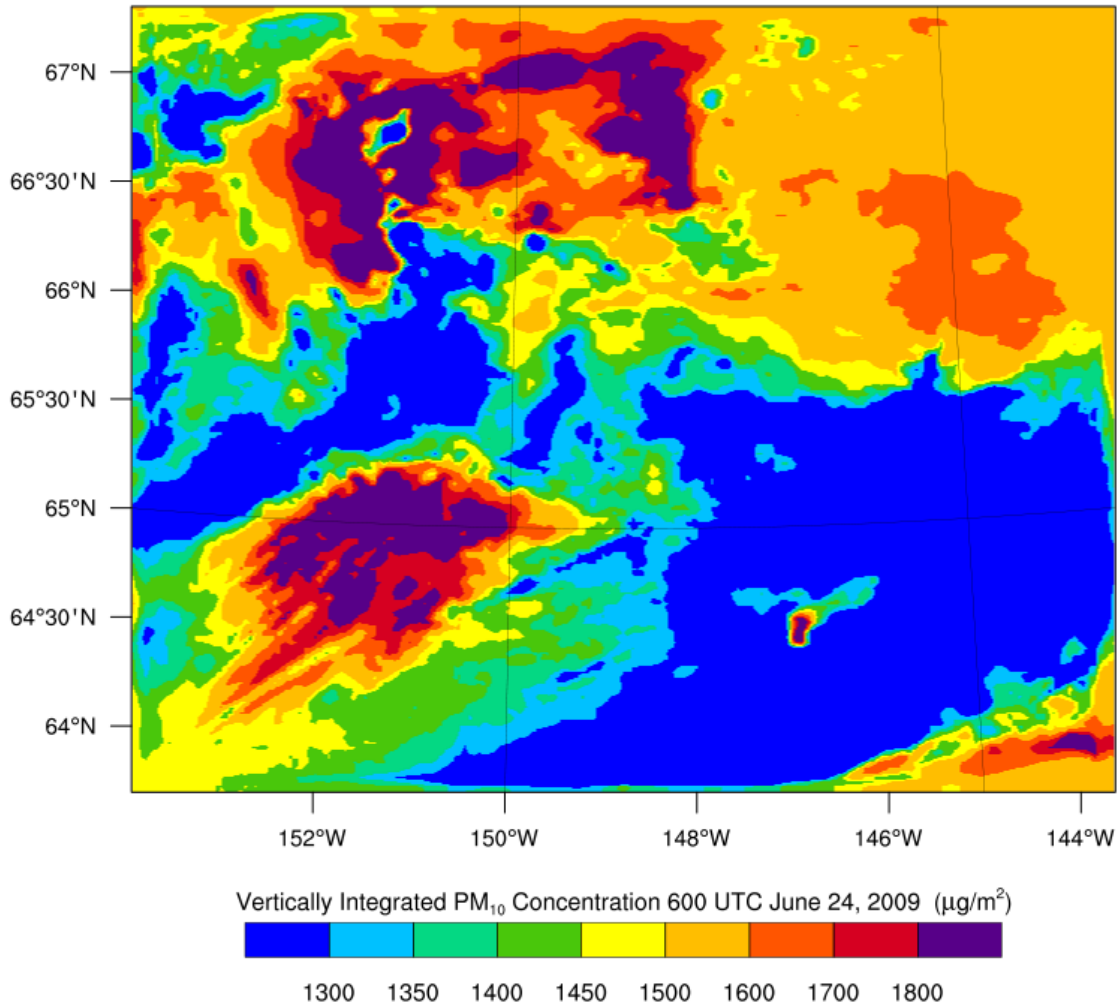


Fig. 4.8 A raw WRF/Chem plot for 600 UTC, June 24, 2009, illustrating an optically-thick environment with high amounts of simulated accumulated smoke. Note the large separation between the smoke plumes to the west and the Fairbanks metropolitan region that is located at 64°30'N latitude, 147° longitude.

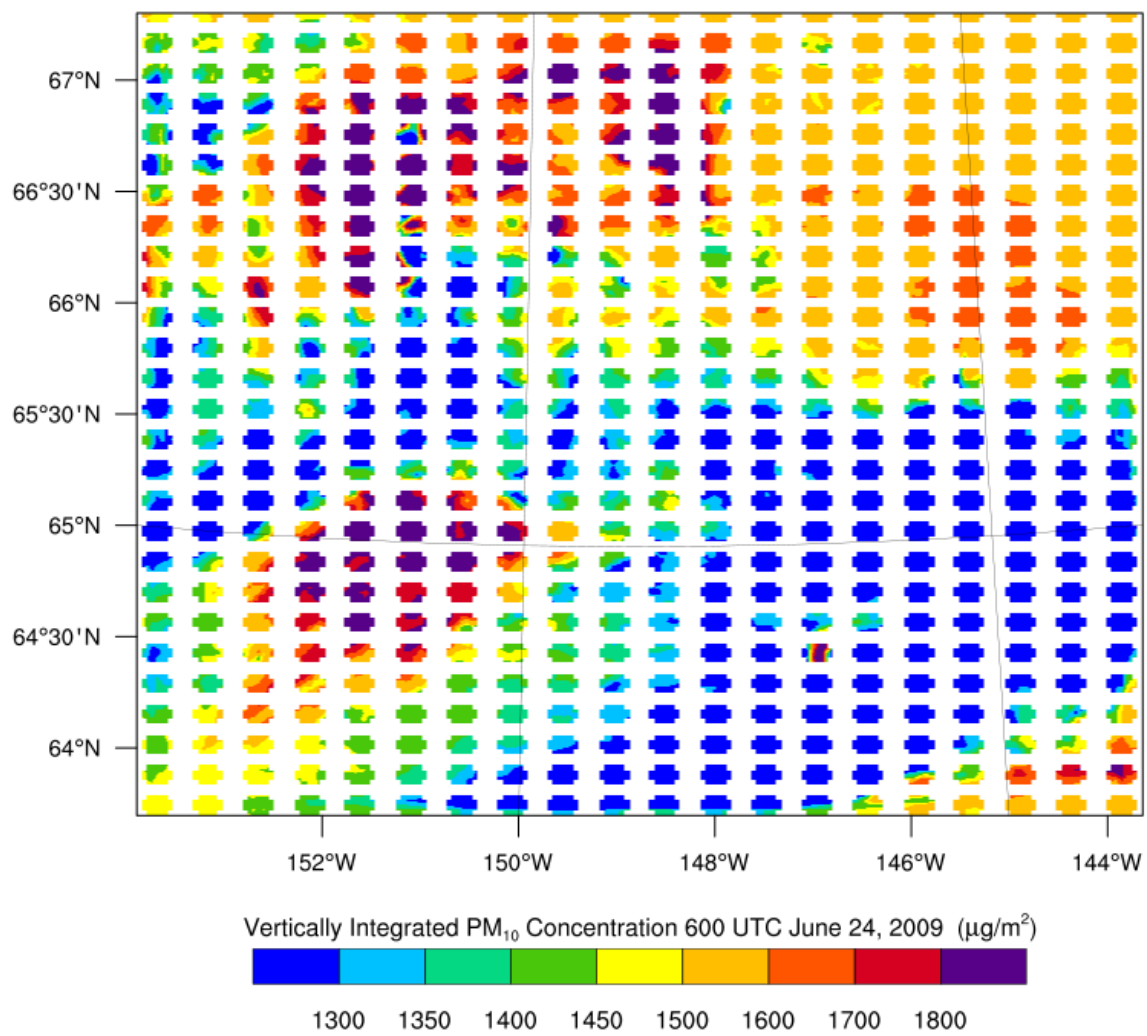


Fig. 4.9 A grid of synthetic pixels overlay the previous plot.

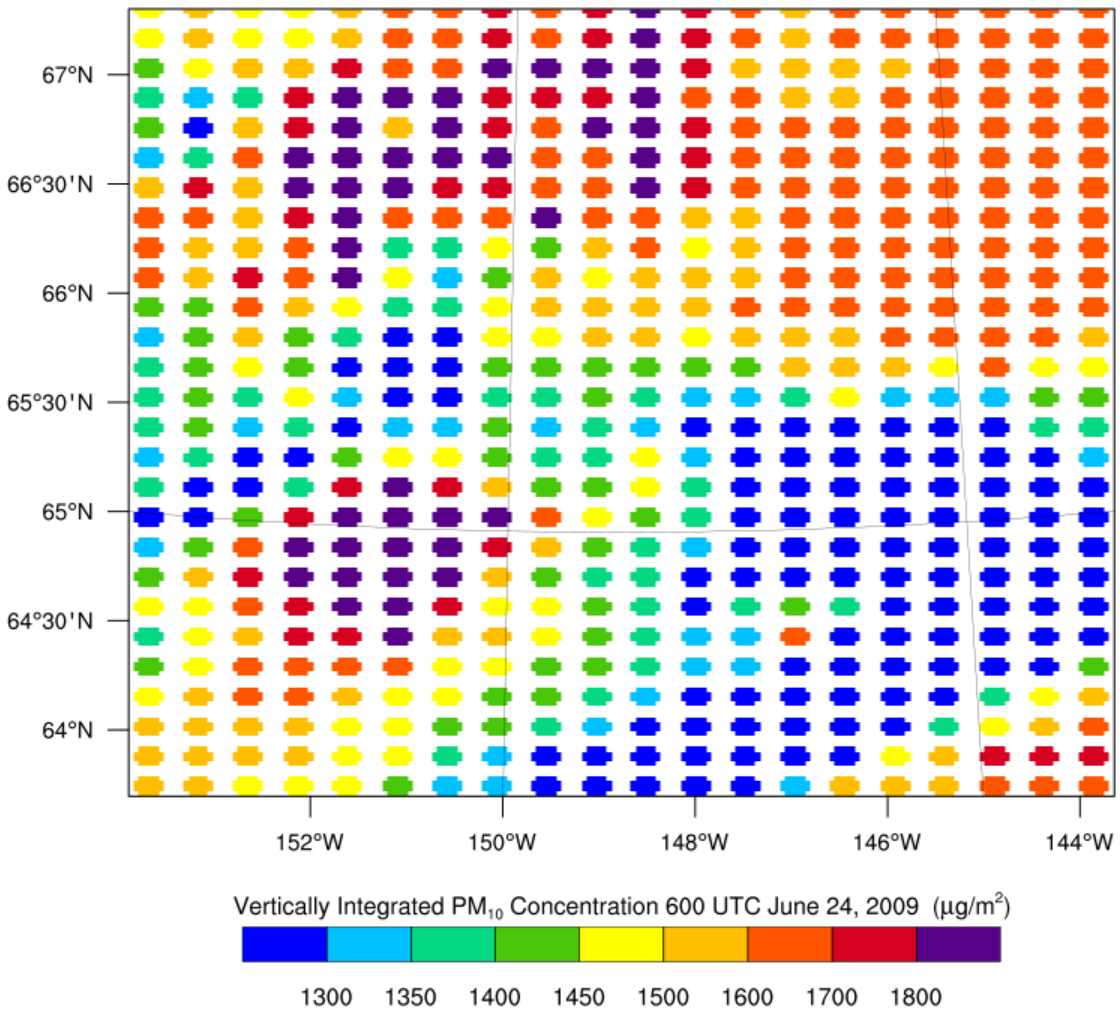


Fig. 4.10 Synthetic pixels from the previous figure are averaged to produce a smoke-polluted environment test case.

Figure 4.11 illustrates the model cross-section through the area of the smoke plume. The cross-section indicates a high presence of simulated PM_{10} concentration, from the surface to the 2.5 km vertical layer. The high concentration of simulated PM_{10} is situated in the same spatial regime as the plume. As was demonstrated by the synthetic pixels created from evaluated WRF/Chem data, an area with strong wildfire smoke signatures should be visible at the edge of a geostationary satellite's field of view. However, smaller smoke plumes to the northern and western portions of the domain remain undetected. This means further research is needed to optimize the threshold. Establishing a threshold was beyond the scope of this thesis; however, the feasibility of a threshold was to be accessed.

4.4 Synthetic Pixel Discussion

Overall, the synthetic pixels can easily distinguish between non-smoke and smoke regions. Moreover, the synthetic pixels can detect a spread between different sources of PM_{10} . In summary, a synthetic pixel program can be used as a tool to detect smoke plumes at the edge of a geostationary satellite's field of view.

However, there are issues to discuss in regard to synthetic pixel performance, and how these synthetic pixels can be developed for future projects. For example, the synthetic pixel program does not consider the geostationary satellite's view angle during vertical integration. While correcting for this aspect would theoretically yield more accurate results, a majority of smoke plumes in the domain propagate within the boundary layer, not throughout the entire atmosphere (see Figures 4.7 and 4.11). Thus, a correction in regard to the view angle, while warranted, should yield modest results.

Additionally, synthetic pixel program products can depend upon the positioning of the pixel grid within the domain. For example, if all synthetic pixels are shifted upward in latitude by only one 1 grid-cell (2 km), a couple of averaged results are changed (Fig. 4.12). Figure 4.12 highlights the discrepancies that could occur with the large spatial variabilities of smoke. Note that a radiometer, however, scans at a discrete distance, and the same scan-line is scanned every 15 minutes. Thus, the shift shown in Figure 4.12 does not actually occur, but only serves to demonstrate challenges in determining the threshold.

Finally, the synthetic pixels, while appropriately sized for the area in question, do not consider the changes in pixel distortion with even smaller changes in latitude and the effects from pixel overlapping. For simplicity, synthetic pixel sizes in the program are assumed to be fixed

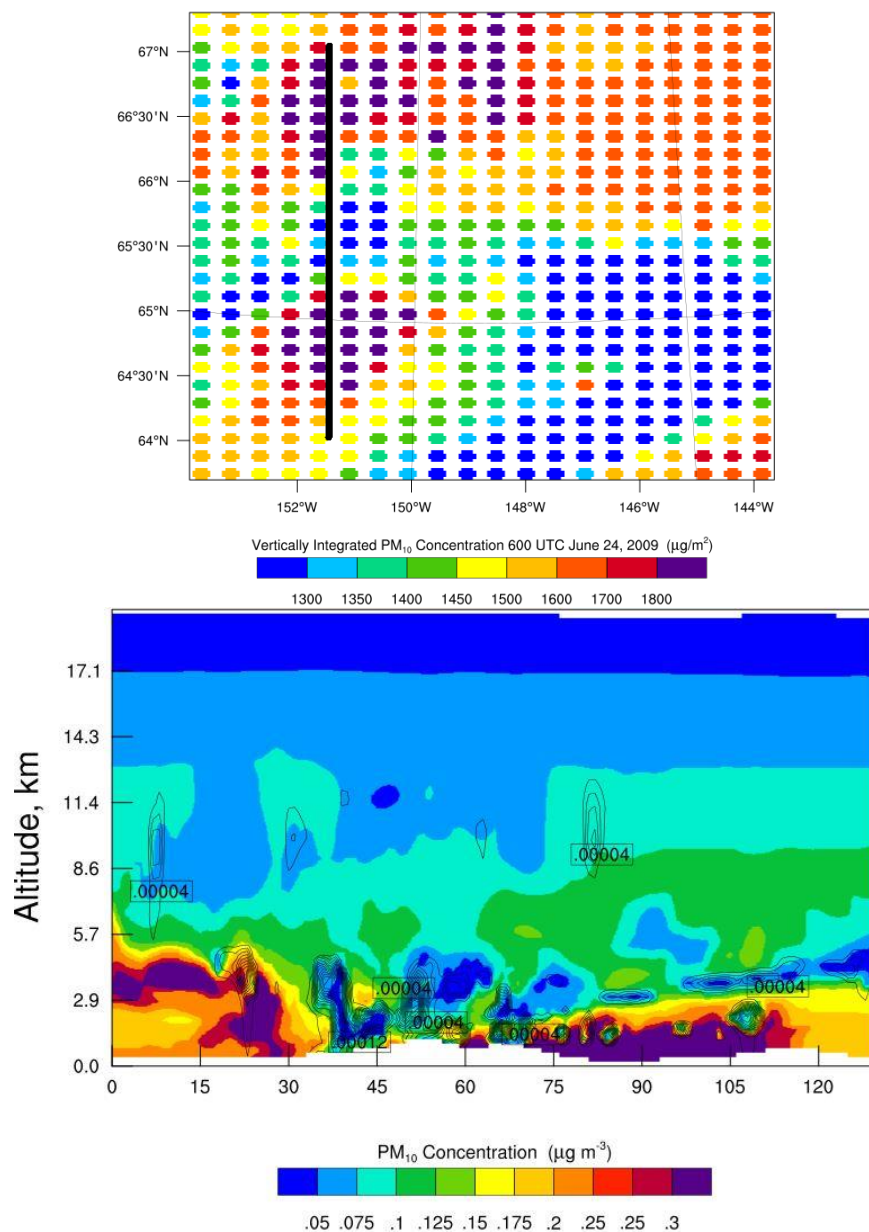


Fig. 4.11 A cross-section through part of the polluted-environment case, 24 June, 2009, 600 UTC. The red line in the model domain (top) illustrates the position of the model cross-section. In the model cross-section (bottom), the north is to the left of the plot, and the south is to the right of the plot. The model cross-section shows a high PM₁₀ concentration near the signature of the plume. Black contours indicate the cloud particle mixing ratio (cloud-water + rain-water + snow + graupel + ice mixing ratios), as defined by a threshold value suggested by Beres et al. (2009).

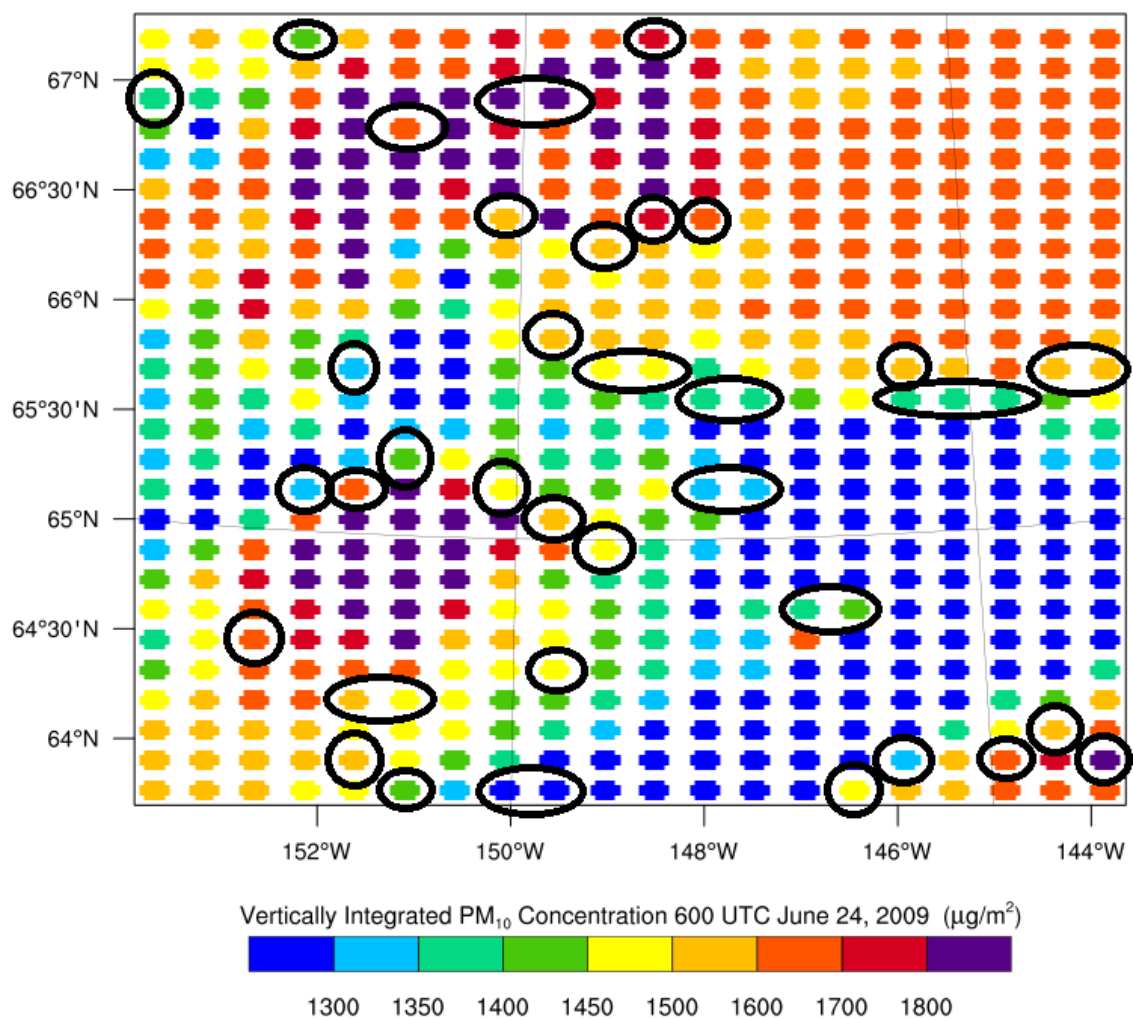


Fig. 4.12 An illustration of discrepancies that occur (in comparison to Figure 4.10) with regard to wide spatial distributions of smoke. Black circles and ovals indicate several of the changes occur with a shift in synthetic pixel grid positioning.

throughout the entire domain. As seen with Figure 4.12, small changes in positioning, and furthermore size, can alter averaged results. Moreover, the threshold used for this thesis depended upon only one air-quality monitoring station; the threshold can change when more air-quality information becomes available.

Chapter 5 Discussion and Conclusions

The thesis tested the hypothesis that a four-dimensional dataset can be created with WRF/Chem to demonstrate that smoke-contaminated synthetic pixels can be distinguished from clean synthetic pixels at the edge of a geostationary satellite's field of view. The next generation of radiometers, with a 1 km nadir resolution over the equator, was considered for the thesis. In order to test the hypothesis, the following work was performed.

To create a wildfire smoke dataset, the region's wildfire climatology must be known to gain historical context for the test case data. The climatology of Interior Alaska and the generation of wildfires in Interior Alaska were considered as context. Through a large margin, Interior Alaska has the most wildfires in the State. Interior Alaska is wildfire-prone as the area features low surface winds, light precipitation, easily flammable vegetation, and continental influences. Moreover, climatological patterns have an influence on wildfire activity in Interior Alaska, and there are concerns that high-latitude wildfires might increase in the future. These concerns are troublesome as wildfires in Interior Alaska lead to the destruction of personal and governmental property, and the concern for health. The human costs of wildfires and the related smoke created the motivation for early detection.

However, wildfire detection in the high latitudes is difficult, due to low observational coverage. While polar-orbiting satellites, like CALIPSO and Aqua, provide great data of smoke activity at the surface, they lack the spatial and the temporal coverage that is ideal for wildfire detection. Geostationary satellites have greater spatial and temporal coverage, and would be a great resource for high-latitude wildfire detection. Thus, the goal of this study was to create a suitable wildfire smoke dataset and a set of synthetic pixels to demonstrate that smoke plumes could be detectable from a geostationary satellite at the edge of its field of view.

The creation of the model data required Alaska-specific initial and boundary conditions, and the appropriate physical and chemical packages. The simulated meteorology was statistically tested and the vertical extent of simulated wildfire aerosols was qualitatively examined. To the best knowledge of the author, the latter was the first WRF/Chem-CALIPSO data comparison at the high-latitudes. The vertical extent of wildfire aerosol plumes had to be tested qualitatively as there were no tools to directly measure the vertical distribution of aerosol concentrations in Interior Alaska during the period of interest.

Skill scores were used to statistically evaluate the simulated meteorology. Specifically, the bias, RMSE, SDE, and the correlation were used. WRF/Chem simulated temperature,

dewpoint temperature, relative humidity, precipitation, wind speed, wind direction, downward shortwave radiation, and sea-level pressure were compared to the surface observations of these quantities. Despite systematic and random errors, WRF/Chem's meteorological performance was very good and similar in quality to many past WRF (and other model) studies in Alaska and elsewhere. I conclude the meteorological simulations were acceptable.

Backscatter and backscatter-derived linear depolarization ratio products from CALIPSO were used to qualitatively examine WRF/Chem simulated aerosols above the surface. Specifically, cross-sections of total backscatter, perpendicular backscatter and linear depolarization ratios were compared to WRF/Chem cross-sections of simulated PM_{10} . When available, the comparisons were supplemented with MODIS imagery, and positive smoke indices from METAR reports and National Weather Service discussions. Despite small spatial and temporal differences, the model simulations were very similar to CALIPSO backscatter and depolarization data. In conclusion, the simulated results are acceptable, and the WRF/Chem output can be used a realistic dataset to demonstrate that signatures of smoke could be detected at the edge of a satellite's field of view.

The WRF/Chem dataset was then used as input to a synthetic pixel program. The program was used to demonstrate the possibility of smoke detection in pixels at the edge of a geostationary satellite's field of view. To demonstrate this possibility, synthetic pixels were constructed by the program. The synthetic pixels were appropriately sized to represent the distortion of pixel geometry and area that occurs from the equator to the poles. Additionally, the synthetic pixels featured the entire atmospheric column content and were color-coded to visually distinguish clean pixels from smoke-polluted pixels. To numerically distinguish between clean and polluted pixels, a $1,800 \mu\text{g}/\text{m}^2$ threshold was used. Due to the lack of other suitable data, the $1,800 \mu\text{g}/\text{m}^2$ threshold was derived from vertically integrating an equivalent concentration equation through the use of the mean Denali IMPROVE PM_{10} non-fire season data and the WRF/Chem layer thicknesses up to 2 km.

Two synthetic pixel test cases were generated: a clean, optically-thin episode with low PM_{10} ; and, a polluted, optically-thick episode with a high presence of PM_{10} . Both clean and polluted synthetic pixels were examined through model cross-sections, and the polluted synthetic pixels were further analyzed to determine the horizontal extent of the plume.

The synthetic pixels demonstrated their purposes in both cases; the light, optically-thin test case displayed pixels that were low in PM_{10} and below the $1,800 \mu\text{g}/\text{m}^2$ threshold, and the

polluted, optically-thick test case clearly displayed pixels that were indicative of a smoke plume. The synthetic pixels were also able to distinguish between different sources of PM_{10} . The cross-section of simulated PM_{10} , which was taken through the group of polluted synthetic pixels, illustrated a smoke plume to the south of the domain. Through the analysis of these test cases, clean and polluted synthetic pixels can be distinguished, and polluted synthetic pixels can indicate the presence of a smoke plume. However, additional research must be undertaken to optimize a threshold to detect smaller fires. In conclusion, smoke detection should be possible at the edge of the field of view for instruments with resolutions of 1 km at the sub-satellite point.

5.1 Future Work

There are a few ways to improve and add upon this research. First, parameterizations of wildfire heat transfer effects could be added. While there will be systematic errors, the inclusion of wildfire heat transfer parameterizations may change the simulated meteorology and gas-phase chemistry temporally and spatially. If a statistical evaluation of the model shows that wildfire heat transfer parameterizations improve the previous skill scores, then the inclusion would produce a better realistic dataset.

The synthetic pixel program can also be expanded upon to include the satellite's view angle during integration. Correcting for this aspect would theoretically yield more accurate results. Moreover, using multiple grids at the same time period with slightly different spatial positions could yield more accurate results, as additional grid-cells would be considered. Also, the synthetic pixel program could be expanded upon to include the changes in pixel distortion and area with even smaller changes in latitude.

Finally, the thesis only concerned the year of 2009, as the goal was to simply show the feasibility of smoke plume detection. While 2009 was an active wildfire year, the most recent years include certain advantages. For example, several air-quality stations were installed near the Fairbanks metropolitan region. More air-quality stations would improve the qualitative analysis of model performance, and open possibilities for statistical comparisons. Recent years also include ground lidar data from the Arctic Facility for Atmospheric Remote Sensing (AFARS) site. Additional lidar readings, especially from a source other than CALIPSO, would improve qualitative analyses. In regard to CALIPSO and other lidar data, quantitative evaluation methods should be developed. In summary, there are opportunities to increase the qualitative and quantitative examinations of the spatial presence of aerosols. Acting upon these opportunities

will improve the validity of the WRF/Chem simulations and the artificial dataset created therefrom.

References

- Alaska Climate Research Center, cited 2013: Temperature changes in Alaska. [Available online at <http://climate.gi.alaska.edu/ClimTrends/Change/TempChange.html>.]
- Alaska Interagency Coordination Center (AICC), cited 2013: 2013 fire numbers. [Available online at <http://prezi.com/b-xnw1kn-idb/2013-fire-numbers/>.]
- Amiro, B. D., J. I. MacPherson, and R. L. Desjardins, 1999: BOREAS flight measurements of forest-fire effects on carbon dioxide and energy fluxes. *Agr. Forest Meteorol.*, **96**(4), 199-208.
- Anthes, R. A., 1984: Enhancement of convective precipitation by mesoscale variations in vegetative covering in semiarid regions. *J. Appl. Meteor. Climatol.*, **23**(4), 541-554.
- Anthes, R. A., Y.-H. Kuo, E.-Y. Hsie, S. Low-Nam, and T. W. Bettge, 1989: Estimation of skill and uncertainty in regional numerical models. *Quart. J. Roy. Meteor. Soc.*, **115**(488), 763-806.
- Arakawa, A., and V. R. Lamb, 1977: Computational design of the basic dynamical processes of the UCLA general circulation model. *Methods in Computational Physics*, J. Chang, Ed., Academic Press, New York, 173-265.
- Avissar, R., and R. A. Pielke, 1989: A parameterization of heterogeneous land surfaces for atmospheric numerical models and its impact on regional meteorology. *Mon. Wea. Rev.*, **117**(10), 2113-2136.
- Barney, R. J., 1971: Wildfires in Alaska - some historical and projected effects and aspects. *Proc. Fire in the Northern Environment - A Symposium*, Fairbanks, AK, USDA Forest Service – Pacific Northwest Forest and Range Experiment Station, 51-59.

- Beljaars, A. C. M., 1994: The parameterization of surface fluxes in large-scale models under free convection. *Quart. J. Roy. Meteor. Soc.*, **121**(522), 255-270.
- Beres, J., A. Prakash, and N. Mölders, 2009: Comparison of WRF model outputs and MODIS image products for cloud presence: A case study. ARSC-REU Report, 22 pp.
- Beychok, M.R., 2005: *Fundamentals of stack gas dispersion*. Milton R. Beychok, Irvine, CA, 201 pp.
- Bieniek, P. A., 2007: Climate and predictability of Alaska wildfires. Thesis, Department of Atmospheric Sciences, University of Alaska Fairbanks, 95 pp.
- Brotak, E. A., and W. E. Reifsnyder, 1977: An investigation of the synoptic situations associated with major wildland fires. *J. Appl. Meteor. Climatol.*, **16**(9), 867-870.
- Brown, M., 2008: Impact of local external forcing of the 2006 Augustine Volcano eruption on regional weather conditions. Thesis, Department of Atmospheric Sciences, University of Alaska Fairbanks, 134 pp.
- Bytnerowicz, A. S., M. J. Arbaugh, A. R. Riebau, and C. Anderson, 2009: Integrating research on wildland fires and air quality: needs and recommendations. *Wildland fires and air pollution*, A. Bytnerowicz, M. J. Arbaugh, A. R. Riebau and C. Anderson, Eds., Elsevier B. V., Oxford, UK, 585-602.
- Cayford, J. H., and D. J. McRae, 1983: The ecological role of fire in jack pines. *The Role of Fire in Northern Circumpolar Ecosystems*, R. W. Wein and D. A. MacLean, Eds., John Wiley & Sons, New York, NY, 183-200.
- Chang, J., R. A. Brost, I. S. A. Isaksen, S. Madronich, P. Middleton, W. R. Stockwell, and C. J. Walcek, 1987: A three-dimensional Eulerian acid deposition model: Physical concepts and formation. *J. Geophys. Res.*, **92**(D12), 14681-14700.

- Chang, J.-T., and P. J. Wetzel, 1991: Effects of spatial variations of soil moisture and vegetation on the evolution of a prestorm environment: a numerical case study. *Mon. Wea. Rev.*, **119**(6), 1368-1390.
- Cheng, W. Y. Y., and W. J. Steenburgh, 2005: Evaluation of surface sensible weather forecasts by the WRF and the Eta models over the western United States. *Wea. Forecasting*, **20**(5), 812-821.
- Collins, D. C., and R. Avissar, 1994: The impact of land-surface wetness heterogeneity on mesoscale heat fluxes. *J. Appl. Meteorol.*, **33**(11), 1323-1340.
- Cosgrove, B. A., D. Lohmann, K. E. Mitchell, P. R. Houser, E. F. Wood, J. C. Schaake, A. Robock, J. Sheffield, Q. Duan, L. Luo, R. W. Higgins, R. T. Pinker, and J. D. Tarpley, 2003: Land surface model spin-up behavior in the North American Land Data Assimilation System (NLDAS). *J. Geophys. Res.*, **108**(D22), doi:10.1029/2002JD003316.
- Damoah, R., N. Spichtinger, R. Servranckx, M. Fromm, E. W. Eloranta, I. A. Razenkov, P. James, M. Shulski, C. Forster, and A. Stohl, 2006: A case study of pyro-convection using transport model and remote sensing data. *Atmos. Chem. Phys.*, **6**(1), 173-185.
- Delta News Web, cited 2014: Wildfire threatens Alaska Highway. [Available online at <http://news.deltanewsweb.com/news/2013/06/02/wildfire-threatens-alaska-highway/>.]
- Dingman, S. L., 2002: *Physical Hydrology*. Prentice Hall, Upper Saddle River, NJ, 646 pp.
- Dominici, F., R. D. Peng, M. L. Bell, L. Pham, A. McDermott, S. L. Zeger, and J. M. Samet, 2006: Fine particulate air pollution and hospital admission for cardiovascular and respiratory diseases. *JAMA - J. Am. Med. Assoc.*, **295**(10), 1127-1134.
- Duck, T. J., B. J. Firanski, D. B. Millet, A. H. Goldstein, J. Allan, R. Holzinger, D. R. Worsnop, A. B. White, A. Stohl, C. S. Dickinson, and A. van Donkelaar, 2007: Transport of forest

- fire emissions from Alaska and the Yukon Territory to Nova Scotia during summer 2004. *J. Geophys. Res.-Atmos.*, **112**(D10), doi: 10.1029/2006JD007716.
- Duffy, P. A., J. E. Walsh, J. M. Graham, D. H. Mann, and T. S. Rupp, 2005: Impacts of large-scale atmospheric-ocean variability on Alaskan fire season severity. *Ecol. Appl.*, **15**(4), 1317-1330.
- EC-JRC/PBL, cited 2014: EUROPA – EDGAR homepage. [Available online at <http://edgar.jrc.ec.europa.eu/>.]
- Ernst, A., and J. D. Zibrak, 1998: Carbon monoxide poisoning. *N. Engl. J. Med.*, **339**(22), 1603-1608.
- Fairbanks North Star Borough, cited 2013: Fairbanks North Star Borough – Welcome. [Available online at <http://www.co.fairbanks.ak.us/default.htm>.]
- Fauria, M. M., and E. A. Johnson, 2006: Large-scale climatic patterns control large lightning fire occurrence in Canada and Alaska forest regions. *J. Geophys. Res.-Biogeo.*, **111**(G4), doi: 10.1029/2006JG000181.
- Flannigan, M. D., and J. B. Harrington, 1988: A study of the relation of meteorological variables to monthly provincial area burned by wildfire in Canada (1953–80). *J. Appl. Meteor. Climatol.*, **27**(4), 441-452.
- Forster, C., U. Wandinger, G. Wotawa, P. James, I. Mattis, D. Althausen, P. Simmonds, S. O’Doherty, S. G. Jennings, C. Kleefeld, J. Schneider, T. Trickel, S. Kreipl, H. Jäger, and A. Stohl, 2001: Transport of boreal forest fire emissions from Canada to Europe. *J. Geophys. Res.*, **106**(D19), 22,887-22,906.
- Freitas, S. R., K. M. Longo, M. Silva Dias, P. Silva Dias, R. Chatfield, E. Prins, P. Artaxo, G. Grell, and F. Recuero, 2005: Monitoring the transport of biomass burning emissions in

South America. *Environ. Fluid Mech.*, **5**(1-2), 135-167, doi: 10.1007/s10652-005-0243-7.

Freitas, S. R., K. M. Longo, R. Chatfield, D. Latham, M. Silva Dias, M. O. Andreae, E. Prins, J. C. Santos, R. Gielow, and J. A. Carvalho Jr., 2007: Including the sub-grid scale plume rise of vegetation fires in low resolution atmospheric transport models. *Atmos. Chem. Phys.*, **7**, 3385-3398, doi: 10.5194/acp-7-3385-2007.

Geographic Information Network of Alaska, cited 2013: MODIS satellite data from Swathviewer. [Available online at <http://sv.gina.alaska.edu/#>.]

Goldammer, J. G., M. Statheropoulos, and M.O. Andreae, 2009: Impacts of vegetation fire emissions on the environment, human health, and security: a global perspective. *Developments in environmental science*, A. Bytnerowicz, M. Arbaugh, A. Riebau, and C. Anderson, Eds., Elsevier B.V., Oxford, UK, 3-36.

Grell, G. A., S. E. Peckham, R. Schmitz, S. A. McKeen, G. Frost, W. C. Skamarock, and B. Eder, 2005: Fully coupled "online" chemistry within the WRF model. *Atmos. Env.*, **39**(37), 6957-6975.

Grell, G., S. R. Freitas, M. Stuefer, and J. Fast, 2011: Inclusion of biomass burning in WRF-Chem: impact of wildfires on weather forecasts. *Atmos. Chem. Phys.*, **11**(11), 5289-5303.

Guenther, A., P. Zimmerman, P. C. Harley, R. K. Monson, and R. Fall, 1993: Isoprene and monoterpene emission rate variability: Model evaluations and sensitivity analyses. *J. Geophys. Res.-Atmos.*, **98**(D7), 12,609-12,617.

Guenther, A., P. Zimmerman, and M. Wildermuth, 1994: Natural volatile organic compound emission rate estimates for U.S. woodland landscapes. *Atmos. Environ.*, **28**(6), 1197-1210.

- Henry, D. M., 1978: Forecasting fire occurrence using 500 mb map correlation. NOAA Technical Memorandum NWS AR-21, 31 pp.
- Hess, J. C., C. A. Scott, G. L. Hufford, and M. D. Fleming, 2001: El Niño and its impact on fire weather conditions in Alaska. *Int. J. Wildland Fire*, **10**(1), 1-13.
- Hillger, D. W., and T. J. Schmit, 2011: The GOES-15 science test: Imager and sounder radiance and product validations. NOAA Technical Report NESDIS 141, 114 pp.
- Hines, K. M., and D. H. Bromwich, 2008: Development and testing of Polar WRF. Part 1. Greenland ice sheet meteorology. *Mon. Wea. Rev.*, **136**(6), 1971-1989.
- Hines, K. M., D. H. Bromwich, L.-S. Bai, M. Barlage, and A. G. Slater, 2011: Development and testing of Polar WRF. Part III. Arctic Land. *J. Climate*, **24**(1), 26-48.
- Hogan, W. H., and W. Hurlburt, 2010: Association between air quality and hospital visits - Fairbanks, 2003-2008, *State of AK Epidemiology Bulletin*, No. 26, 1 pp.
- Houze, R. A., 1993: *Cloud Dynamics*. Academic Press, San Diego, CA, 573 pp.
- Hu, Y., 2007: Depolarization ratio-effective lidar ratio relation: Theoretical basis for space lidar cloud phase determination. *Geophys. Res. Lett.*, **34**(11), doi: 10.1029/2007GL029584.
- Hunt, W. H., D. M. Winker, M. A. Vaughan, K. A. Powell, P. L. Lucke, and C. Weimer, 2009: CALIPSO lidar description and performance assessment. *J. Atmos. Oceanic Technol.*, **26**(7), 1214-1228.
- Janjić, Z. I., 2002: Nonsingular implementation of the Mellor-Yamada level 2.5 scheme in the NCEP meso model, *NCEP Office Note*, No. 437, 61 pp.
- Jiménez, P.A., and J. Dudhia, 2013: On the ability of the WRF model to reproduce the surface wind direction over complex terrain. *J. Appl. Meteor. Climatol.*, **52**(7), 1610-1617.

- Johnson, E. A., and D. R. Wowchuk, 1993: Wildfires in the southern Canadian Rocky Mountains and their relationship to mid-tropospheric anomalies. *Can. J. Forest Res.*, **23**(6), 1213-1222.
- Justice, C. O., L. Giglio, S. Korontzi, J. Owens, J. T. Morisette, D. Roy, J. Descloitres, S. Alleaume, F. Petitcolin, and Y. Kaufman, 2002: The MODIS fire products. *Remote Sens. Environ.*, **83**(1-2), 244-262.
- Kappos, A. D., P. Bruckmann, T. Eikmann, N. Englert, U. Heinrich, P. Höppe, E. Koch, G. H. M. Krause, W. G. Kreyling, K. Rauchfuss, P. Rombout, V. Schulz-Klemp, W. R. Thiel, and H.-E. Wichmann, 2004: Health effects of particles in ambient air. *Int. J. Hyg. Envir. Heal.*, **207**(4), 399-407.
- Kasischke, E. S., K. Bergen, R. Fennimore, F. Sotelo, G. Stephens, A. Janetos, and H. H. Shugart, 1999: Satellite imagery gives clear picture of Russia's boreal forest fires. *Eos Trans. AGU*, **80**(13), 141-147.
- Kasischke, E. S., 2000: Boreal ecosystems in the global carbon cycle. *Fire, climate change, and carbon cycling in the boreal forest*, E. S. Kasischke and B. J. Stocks, Eds., Springer-Verlag, New York, NY, 19-30.
- Kasischke, E. S., D. Williams, and D. Barry, 2002. Analysis of the patterns of large fires in the boreal forest region of Alaska. *Int. J. Wildland Fire*, **11**(2), 131-144.
- Knox, J. L., and R. G. Lawford, 1990: The relationship between Canadian prairie dry and wet months and circulation anomalies in the mid-troposphere. *Atmos.-Ocean*, **28**(2), 189-215.
- Kurz, W. A., M. J. Apps, B. J. Stocks, and W. J. A. Volney, 1995: Global climatic change: disturbance regimes and biospheric feedbacks of temperate and boreal forests. *Biospheric feedbacks in the global climate system: Will the warming feed the*

- warming?, G. F. Woodwell and F. McKenzie, Eds., Oxford University Press, New York, NY, 119-133.
- Labonne, M., F.-M. Bréon, and F. Chevallier, 2007: Injection height of biomass burning as seen from a spaceborne lidar. *Geophys. Res. Lett.*, **34**(L11806), doi: 10.1029/2007GL029311.
- Laprise, R., 1992: The Euler equations of motion with hydrostatic pressure as an independent variable. *Mon. Wea. Rev.*, **120**(1), 197-207.
- Lee, C. H., J. H. Kim, C. B. Park, A. Shimizu, I. Matsui, and N. Sugimoto, 2004: Continuous measurements of smoke of Russian forest fire by 532/1064 nm Mie scattering lidar at Suwon, Korea. *Proc. 22nd International Laser Radar Conference*, G. Pappalardo and A. Amodeo, Eds., Paris, France, European Space Agency, 535-538.
- Leelasakultum, K., N. Mölders, H. N. Q. Tran, and G. Grell, 2012: Potential impacts of the Introduction of low-sulfur fuel on PM_{2.5} concentrations at breathing level in a sub-Arctic city. *Adv. Meteor.*, **2012**, 16 pp, doi: 10.1155/2012/427078.
- Levine, J. S., and W. R. Cofer III, 2000: Boreal forest fire emissions and the chemistry of the atmosphere. *Fire, climate change, and carbon cycling in the boreal forest*, E. S. Kasischke and B. J. Stocks, Eds., Springer-Verlag, New York, NY, 31-48.
- Lin, Y., R. D. Farley, and H. D. Orville, 1983: Bulk parameterization of the snow field in a cloud model. *J. Appl. Meteor. Climatol.*, **22**(6), 1065-1092.
- Liu, Y., J. R. Key, and X. Wang, 2008: On the use of geostationary satellites for remote sensing in the high latitudes. Poster, *AMS 88th Annual Meeting / 5th GOES Users' Conference*, New Orleans, LA, American Meteorological Society.
- Longo, K. M., S. R. Freitas, M. O. Andreae, A. Setzer, E. Prins, and P. Artaxo, 2010: The coupled aerosol and tracer transport model to the Brazilian developments on the regional atmospheric modeling system (CATT-BRAMS) – Part 2: Model sensitivity to the

- biomass burning inventories. *Atmos. Chem. Phys.*, **10**, 5785-5795, doi: 10.5194/acp-10-5785-2010.
- Loose, T., and R.D. Bornstein, 1977: Observations of mesoscale effects on frontal movement through an urban area. *Mon. Wea. Rev.*, **105**(5), 563-571.
- Madronich, S., 1987: Photodissociation in the atmosphere 1. actinic flux and the effects of ground reflection and clouds. *J. Geophys. Res.*, **92**(D8), 9740-9752.
- Manning, K. W., and C. A. Davis, 1997: Verification and sensitivity experiments for the WISP94 MM5 forecasts. *Wea. Forecasting*, **12**(4), 719-735.
- McCormick, M. P., 2005: Airborne and spaceborne lidar. *Lidar, range-resolved optical remote sensing of the atmosphere*, C. Weitcamp, Ed., Springer Science+Business Media Inc., New York, NY, 355-397.
- McGuiney, E., M. Shulski, and G. Wendler, 2005: Alaska lightning climatology and application to wildfire science. *Extended abstract, Conference on Meteorological Applications of Lightning Data*, San Diego, CA, American Meteorological Society, 2.14.
- Mellor, G. L., and T. Yamada, 1982: Development of a turbulence closure model for geophysical fluid problems. *Rev. Geophys. Space Phys.*, **20**, 851-875.
- Middleton, P., W. R. Stockwell, and W. P. L. Carter, 1990: Aggregation and analysis of volatile organic compound emissions for regional modeling. *Atmos. Environ.*, **24**(5), 1107-1133.
- Miller, K. A., D. S. Siscovick, L. Sheppard, K. Shepherd, J. H. Sullivan, G. L. Anderson, and J. D. Kaufman, 2007: Long-term exposure to air pollution and incidence of cardiovascular events in women. *New Engl. J. Med.*, **356**(5), 447-458.

- Mitsuta, Y., Y. Mori, T. Fujitani, and T. Hanafusa, 1973: On the definitions of mean wind speed and direction. *Disaster Prev. Res. Inst. Kyoto Univ. Bull.*, **16B**, 319-326. [In Japanese with English abstract.]
- Mlawer, E. J., S. J. Taubman, P. D. Brown, M. J. Iacono, and S. A. Clough, 1997: Radiative transfer for inhomogeneous atmosphere: RRTM, a validated correlated-k model for the longwave. *J. Geophys. Res.*, **102**(D14), 16663-16682.
- Mölders, N., and A. Raabe, 1996: Numerical investigations on the influence of subgrid-scale surface heterogeneity on evapotranspiration and cloud processes. *J. Appl. Meteor. Climatol.*, **35**(6), 782-795.
- Mölders, N., A. Raabe, and G. Tetzlaff, 1996: A comparison of two strategies on land surface heterogeneity used in a mesoscale β meteorological model. *Tellus A*, **48**(5), 733-749.
- Mölders, N., 2000: Application of the principle of superposition to detect nonlinearity in the short-term atmospheric response to concurrent land-use changes associated with future landscapes. *Meteorol. Atmos. Phys.*, **72**(1), 47-68.
- Mölders, N., and G. Kramm, 2007: Influence of wildfire induced land-cover changes on clouds and precipitation in Interior Alaska — A case study. *Atmos. Res.*, **84**(2), 142-168.
- Mölders, N., 2008: Suitability of the Weather Research and Forecasting (WRF) model to predict the June 2005 fire weather for Interior Alaska. *Wea. Forecasting*, **23**(5), 953-973.
- Mölders, N., 2010: Comparison of Canadian forest fire danger rating system and national fire danger rating system fire indices derived from Weather Research and Forecasting (WRF) model data for the June 2005 Interior Alaska wildfires. *Atmos. Res.*, **95**(2-3), 290-306.
- Mölders, N., and G. Kramm, 2010: A case study on wintertime inversions in Interior Alaska with WRF. *Atmos. Res.*, **95**(2-3), 314-332.

- Mölders, N., H. N. Q. Tran, P. Quinn, K. Sassen, G. E. Shaw, and G. Kramm, 2011: Assessment of WRF/Chem to simulate sub-Arctic boundary layer characteristics during low solar irradiation using radiosonde, SODAR, and surface data. *Atmos. Poll. Res.*, **2**(3), 283-299.
- Mölders, N., 2012: *Land-use and land-cover changes impact on climate and air quality*. Springer Verlag, New York, NY, 189 pp.
- Mölders, N., H. N. Q. Tran, C. F. Cahill, K. Leelasakultum, and T. T. Tran, 2012: Assessment of WRF/Chem PM_{2.5} forecasts using mobile and fixed location data from the Fairbanks, Alaska winter 2008/09 field campaign. *Atmos. Poll. Res.*, **3**(2), 180-191.
- Mölders, N., 2013: Investigations on the impact of single direct and indirect, and multiple emission–control measures on cold–season near–surface PM_{2.5} concentrations in Fairbanks, Alaska. *Atmos. Poll. Res.*, **4**(1), 87-100.
- Monin, A. S., and A. M. Obukhov, 1954: Basic laws of turbulent mixing in the surface layer of the atmosphere. *Contrib. Geophys. Inst. Acad. Sci.*, **24**(151), 163-187.
- Mori, Y., 1986: Evaluation of several “single-pass” estimators of the mean and the standard deviation of wind direction. *J. Appl. Meteor. Climatol.*, **25**(10), 1387-1397.
- Murayama, T., D. Müller, K. Wada, A. Shimizu, M. Sekiguchi, and T. Tsukamoto, 2004: Characterization of Asian dust and Siberian smoke with multi-wavelength Raman lidar over Tokyo, Japan in spring 2003. *Geophys. Res. Lett.*, **31**(23), doi: 10.1029/2004GL021105.
- NASA, cited 2013: Introducing the A-Train. [Available online at http://www.nasa.gov/mission_pages/a-train/a-train.html.]
- O'Neal, M., 1996: Interactions between land cover and convective cloud cover over Midwestern North America detected from GOES satellite data. *Int. J. Remote Sens.*, **17**(6), 1149-1181.

- Ottmar, R. D., A. I. Miranda, and D. V. Sandberg, 2009: Characterizing sources of emissions from wildland fires. *Wildland fires and air pollution*, A. Bytnerowicz, M. Arbaugh, A. Riebau and C. Anderson, Eds., Elsevier B. V., Oxford, UK, 61-78.
- PaiMazumder, D., and N. Mölders, 2009: Theoretical assessment of uncertainty in regional averages due to network density and design. *J. Appl. Meteor. Climatol.*, **48**(8), 1643-1666.
- PaiMazumder, D., D. Henderson, and N. Mölders, 2012: Evaluation of WRF-forecasts over Siberia: Air mass formation, clouds and precipitation. *Open Atmo. Sci. J.*, **6**, 93-110.
- Peckham, S. E., G. A. Grell, S. A. McKeen, M. Barth, G. Pfister, C. Wiedinmyer, J. D. Fast, W. I. Gustafson, S. J. Ghan, R. Zaveri, R. C. Easter, J. Barnard, E. Chapman, M. Hewson, R. Schmitz, M. Salzmann, and S. R. Freitas, 2011: WRF/Chem version 3.3 user's guide. 96 pp.
- Pfister, G. G., C. Wiedinmyer, and L. K. Emmons, 2008: Impacts of the fall 2007 California wildfires on surface ozone: Integrating local observations with global model simulations. *Geophys. Res. Lett.*, **35**(19), doi: 10.1029/2008GL034747.
- Pielke, R. A., 2001: *Mesoscale meteorological modeling*. Academic Press, San Diego, CA, 693 pp.
- Pinty, J.-P., P. Mascart, E. Richard, and R. Rosset, 1989: An investigation of mesoscale flows induced by vegetation inhomogeneities using an evapotranspiration model calibrated against HAPEX-MOBILHY data. *J. Appl. Meteor. Climatol.*, **28**(9), 976-992.
- Platt, C. M. R., 1978: Lidar backscatter from horizontal ice crystal plates. *J. Appl. Meteor.*, **17**(4), 482-488.
- Podur, J., D. L. Martell, and K. Knight, 2002: Statistical quality control analysis of forest fire activity in Canada. *Can. J. Forest Res.*, **32**(2), 195-205.

- Porter, S. E., 2009: Investigation of the impact of ship emissions on atmospheric composition and deposition in remote, coastal landscapes of southwest Alaska. Thesis, Department of Atmospheric Sciences, University of Alaska Fairbanks, 122 pp.
- Rabin, R. M., D. J. Stensrud, S. Stadler, P. J. Wetzel, and M. Gregory, 1990: Observed effects of landscape variability on convective clouds. *Bull. Amer. Meteor. Soc.*, **71**(3), 272-280.
- Reap, R. M., 1991: Climatological characteristics and objective prediction of thunderstorms over Alaska. *Wea. Forecasting*, **6**(3), 309-319.
- Reinhardt, T. E., and R. D. Ottmar, 2000: Smoke exposure at western wildfires. Pacific Northwest Research Station PNW-RP-525, 72 pp.
- Rutledge, S. A., and P. V. Hobbs, 1984: The mesoscale and microscale structure and organization of clouds and precipitation in midlatitude cyclones. XII: A diagnostic modeling study of precipitation development in narrow cloud-frontal rainbands. *J. Atmos. Sci.*, **41**(20), 2949-2972.
- Sassen, K., 2002: Indirect climate forcing over the western US from Asian dust storms. *Geophys. Res. Lett.*, **29**(10), 103-1-103-4, doi: 10.1029/2001GL014051.
- Sassen, K., 2005: Dusty ice clouds over Alaska. *Nature*, **434**(456), doi: 10.1038/434456a.
- Sassen, K., and V. I. Khvorostyanov, 2008: Cloud effects from boreal forest fire smoke: evidence for ice nucleation from polarization lidar data and cloud model simulations. *Environ. Res. Lett.*, **3**(2), doi: 10.1088/1748-9326/3/2/025006.
- Sauter, B., and T. Henmi, 2004: Average forecast errors using MM5 and WRF over complex terrain: Utah, July/August 2003 and January/February 2004. U.S. Army Research Laboratory ARL-MR-597, 24 pp.

- Schaefer, V. J., 1957: The relationship of jet streams to forest wildfires. *J. Forestry*, **55**(6), 419-425.
- Schindler, D. W., 1988: Effects of acid rain on freshwater ecosystems. *Science*, **239**(4836), 149-157.
- Seiler, W., and P. J. Crutzen, 1980: Estimates of gross and net fluxes of carbon between the biosphere and the atmosphere from biomass burning. *Climatic Change*, **2**(3), 207-247.
- Shugart, H. H., T. M. Smith, and W. M. Post, 1992: The potential for application of individual-based simulation models for assessing the effects of global change. *Annu. Rev. Ecol. Syst.*, **23**(1), 15-38.
- Shulski, M., and G. Wendler, 2007: *The Climate of Alaska*. University of Alaska Press, Fairbanks, AK, 208 pp.
- Shvidenko, A., and S. Nilsson, 1994: What do we really know about the Siberian forests? *Ambio*, **23**(7), 396-404.
- Shvidenko, A., and S. Nilsson, 1997: Are the Russian forests disappearing? *Unasylva*, **188**(48), 57-64.
- Simpson, D., A. Guenther, C. N. Hewitt, and R. Steinbrecher, 1995: Biogenic emissions in Europe 1. Estimates and uncertainties. *J. Geophys. Res.*, **100**(D11), 22,875-22,890.
- Skamarock, W. C., J. B. Klemp, J. Dudhia, D. O. Gill, D. M. Barker, M. G. Duda, X. Huang, W. Wang, and J. G. Powers, 2008: A description of the advanced research WRF version 3. NCAR Tech. Note NCAR/TN-475+STR, 125 pp.
- Skamarock, W.C., W. Wang, C. Bruyère, M. Duda, J. Dudhia, D. Gill, H.-C. Lin, J. Michalakes, S. Rizvi, X. Zhang, J. D. Beezley, J. L. Coen, and J. Mandel, 2011: Weather research

and forecasting ARW version 3 modeling system user's guide – April 2011. National Center for Atmospheric Research, 362 pp.

Skinner, W. R., M. D. Flannigan, B. J. Stocks, D. L. Martell, B. M. Wotton, J. B. Todd, J. A. Mason, K. A. Logan, and E. M. Bosch, 2002: A 500 hPa synoptic wildland fire climatology for large Canadian forest fires, 1959–1996. *Theor. Appl. Climatol.*, **71**(3-4), 157-169.

Smirnova, T. G., J. M. Brown, and S. G. Benjamin, 1997: Performance of different soil model configurations in simulating ground surface temperature and surface fluxes. *Mon. Wea. Rev.*, **125**(8), 1870-1884.

Smirnova, T. G., J. M. Brown, S. G. Benjamin, and D. Kim, 2000: Parameterization of cold-season processes in the MAPS land-surface scheme. *J. Geophys. Res.*, **105**(D3), 4077-4086.

Soja, A. J., N. M. Tchepakova, N. H. F. French, M. D. Flannigan, H. H. Shugart, B. J. Stocks, A. I. Sukhinin, E. I. Parfenova, F. S. Chapin III, and P. W. Stackhouse Jr., 2007: Climate-induced boreal forest change: Predictions versus current observations. *Global Planet. Change*, **56**(3–4), 274-296.

Statistics Canada, cited 2014: Population and dwelling counts, for Canada, provinces and territories, 2011 and 2006 censuses. [Available online at <http://www12.statcan.ca/census-recensement/2011/dp-pd/hltfst/pd-pl/Table-Tableau.cfm?LANG=Eng&T=101&S=50&O=A>.]

Stocks, B. J., M. A. Fosberg, M. B. Wotton, T. J. Lynham, and K. C. Ryan, 2000: Climate change and forest fire activity in North American boreal forests. *Fire, climate change, and carbon cycling in the boreal forest*, E. S. Kasischke and B. J. Stocks, Eds., Springer-Verlag, New York, NY, 368-376.

- Stockwell, W. R., P. Middleton, J. S. Chang, and X. Tang, 1990: The second generation regional acid deposition model chemical mechanism for regional air quality modeling. *J. Geophys. Res.*, **95**(D10), 16343-16367.
- Sullivan, W. G., 1963: Low-level convergence and thunderstorms in Alaska. *Mon. Wea. Rev.*, **91**(2), 89-92.
- Trier, S. B., F. Chen, and K. W. Manning, 2004: A study of convection initiation in a mesoscale model using high-resolution land surface initial conditions. *Mon. Wea. Rev.*, **132**(12), 2954-2976.
- Tuccella, P., G. Curci, G. Visconti, B. Bessagnet, L. Menut, and R. J. Park, 2012: Modeling of gas and aerosol with WRF/Chem over Europe: Evaluation and sensitivity study. *J. Geophys. Res.*, **117**(D3), doi: 10.1029/2011JD016302.
- Urbanski, S. P., W. M. Hao, and S. Baker, 2009: Chemical composition of wildland fire emissions. *Developments in environmental science*, A. Bytnerowicz, M. Arbaugh, A. Riebau, and C. Anderson, Eds., Elsevier B.V., Oxford, UK, 79-107.
- U.S. Census Bureau, cited 2013: State & County QuickFacts - Alaska. [Available online at <http://quickfacts.census.gov/qfd/states/02000.html>.]
- U.S. EPA, cited 2014a: An introduction to indoor air quality (IAQ) – carbon monoxide (CO). [Available online at <http://www.epa.gov/iaq/co.html>.]
- U.S. EPA, cited 2014b: Ozone. [Available online at <http://www.epa.gov/ozone/>.]
- U.S. EPA, cited 2014c: What is acid rain? [Available online at <http://www.epa.gov/acidrain/what/index.html>.]

- Viereck, L. A., 1983: The effects of fire in black spruce ecosystems of Alaska and northern Canada. *The role of fire in northern circumpolar ecosystems*, R. W. Wein and D. A. MacLean, Eds., John Wiley & Sons, Chichester, UK, 201-220.
- Wandinger, U., 2005: Introduction to lidar. *Lidar, range-resolved optical remote sensing of the atmosphere*, C. Weitcamp, Ed., Springer Science+Business Media Inc., New York, NY, 1-18.
- Whiteman, C. D., 2000: *Mountain meteorology: Fundamentals and applications*. Oxford University Press, 355 pp.
- Winker, D. M., W. H. Hunt, and M. J. McGill, 2007: Initial performance assessment of CALIOP. *Geophys. Res. Lett.*, **34**(19), doi: 10.1029/2007GL030135.
- Wotawa, G., and M. Trainer, 2000: The influence of Canadian forest fires on pollutant concentrations in the United States. *Science*, **288**(324), doi: 10.1126/science.288.5464.324.
- Zhang, Y., 2008: Online-coupled meteorology and chemistry models: History, current status, and outlook. *Atmos. Chem. Phys.*, **8**(11), 2895-2932.
- Zhang, Y., X.-Y. Wen, and C. J. Jang, 2010: Simulating chemistry-aerosol-cloud-radiation-climate feedbacks over the continental U.S. using the online-coupled Weather Research Forecasting Model with chemistry (WRF/Chem). *Atmos. Environ.*, **44**(29), 3568-3582.
- Zhong, S., H.-J. In, X. Bian, J. Charney, W. Heilman, and B. Potter, 2005: Evaluation of real-time high-resolution MM5 predictions over the Great Lakes region. *Wea. Forecasting*, **20**(1), 63-81.
- Zhu, J., 2011: Investigation on cirrus clouds by the Cloud-Aerosol Lidar and Infrared Pathfinder Satellite Observation data. Thesis, Department of Atmospheric Sciences, University of Alaska Fairbanks, 219 pp.

- Zhuang, Q., A. D. McGuire, K. P. O'Neill, J. W. Harden, V. E. Romanovsky, and J. Yarie, 2002: Modeling soil thermal and carbon dynamics of a fire chronosequence in Interior Alaska. *J. Geophys. Res.-Atmos.*, **107**(D1), doi: 10.1029/2001JD001244.
- Zilitinkevich, S. S., 1995: Non-local turbulent transport: pollution dispersion aspects of coherent structure of convective flows. *Air pollution III: volume I. Air pollution theory and simulation*, H. Power, N. Moussiopoulos and C. A. Brebbia, Eds., Computational Mechanics Publications, Southampton, UK, 53-60.